Design and Background Simulations for the KATRIN Main Spectrometer and Air Coil System

Nancy Wandkowsky

Institut für Experimentelle Kernphysik
Karlsruhe Institute of Technology (KIT)

Design and Background Simulations for the KATRIN Main Spectrometer and Air Coil System

Diplomarbeit

vorgelegt
von

Nancy Wandkowsky
Institut für Experimentelle Kernphysik
Karlsruhe Institute of Technology (KIT)

Referent: Prof. Dr. G. Drexlin
Institut für Experimentelle Kernphysik

Korreferent: Prof. Dr. W. de Boer
Institut für Experimentelle Kernphysik

30. Oktober 2009

Erklärung

Hiermit erkläre ich, dass ich die vorliegende Arbeit selbst verfasst und keine anderen als die angegebenen Quellen und Hilfsmittel verwendet und diese im Text kenntlich gemacht habe.

Nancy Wandkowsky, Oktober 2009

Zusammenfassung

Das **KA**rslruhe **TRI**tium **N**eutrino Experiment (KATRIN) untersucht das β-Spektrum des Zerfalls von molekularem Tritium nahe des Endpunkts von $18,6$ keV um daraus die Ruhemasse des Elektron-Antineutrinos $m_{\bar{\nu}_e}$ zu bestimmen. Die essentiellen Bestandteile des Experiments sind dabei die fensterlose gasförmige Tritiumquelle (WGTS) mit ihrer extrem hohen Luminosität und das elektrostatische Spektrometer mit seiner besonders hohen Energieauflösung von $\Delta E = 0,93$ eV.

KATRIN strebt dabei eine bisher unerreichbare Sensitivität von $m_{\bar{\nu}_e} < 0,2$ eV/c^2 an. Dieses Ziel kann jedoch nur erreicht werden, wenn die gesamten statistischen und systematischen Unsicherheiten unter einem Schwellwert von $\sigma^2 < 0,017$ eV$^2/c^4$ liegen. Um die systematischen Unsicherheiten zu minimieren, muss jede einzelne Komponente des KATRIN Experiments stabil auf dem Promille Level sein. Daher müssen relevante, experimentelle Parameter stabilisiert und überwacht werden. Für diese Arbeit wichtige Beispiele sind die Säulendichte ρd der Quelle WGTS und das magnetische Führungsfeld der Elektronen im gesamten experimentellen Aufbau und im Spektrometer im Speziellen.

Im Rahmen dieser Arbeit wurden die elektromagnetischen Eigenschaften des Spektrometers mit Hilfe sehr präziser elektrischer und magnetischer Feldberechnungen untersucht und optimiert. Desweiteren bilden diese Feldberechnungsroutinen die Grundlage der Bahnverfolgungssimulationen, welche benutzt wurden um ein besseres Verständnis von Untergrundquellen und ihrer möglichen Folgen für das KATRIN Experiment zu erlangen.

Im Folgenden soll ein kurzer Überblick über die einzelnen Kapitel dieser Arbeit gegeben werden. Für eine ausführliche Darstellung und die dazugehörigen Quellenangaben sei auf den anschließenden (englischen) Haupttext verwiesen.

1. Einführung Seit der Erfindung des Neutrinos durch W. Pauli in den 30er Jahren des letzten Jahrhunderts wurden seine Eigenschaften intensiv erforscht. Die Tatsache, dass es allein fast 30 Jahre dauerte, bis es das erste Mal tatsächlich nachgewiesen werden konnte, zeigt bereits die Schwierigkeit auf bei der Untersuchung des Winzlings. Eine bisher immernoch ungeklärte Frage ist die nach seiner Masse. Die Beobachtung der Neutrinooszillationen durch Super-Kamiokande bestätigte, dass es sich bei den Neutrinos um massebehaftete Teilchen handelt. Diese Art von Experimenten erlaubt es jedoch nicht, quantitative Aussagen bezüglich dieser Masse zu machen. Dafür gibt es zwei vielversprechende Ansätze. Indirekte Methoden stützen sich auf kosmologische Beobachtungen der Strukturbildung im Universum und haben daher den Nachteil, dass sie stark modellabhängig sind. Direkte Nachweismethoden basieren auf der Beobachtung der Kinematik von β-Zerfällen und beinhalten als einzige Annahmen die Drehimpuls- und Energieerhaltung. Einen solchen modellunabhängigen Ansatz der Vermessung des Tritium-β-Spektrums nahe des kinematischen Endpunkts verfolgt das KATRIN Experiment.

2. Das KATRIN Experiment Bisherige Tritiumzerfallsexperimente in Mainz und Troitsk konnten lediglich eine Obergrenze von $2,0$ eV/c^2 für die Neutrinomasse bestimmen. Als Nachfolgeexperiment will KATRIN eine Verbesserung um eine Größenordnung auf 0,2 eV/c^2 erreichen. Da die beobachtete experimentelle Größe jedoch $m^2_{\overline{\nu}_e}$ ist, erfordert dies eine Verbesserung der experimentellen Schlüsselparameter um zwei Größenordnungen. Die Vermessung der Energie der β-Elektronen geschieht, wie bei den Vorgängerexperimenten, unter Verwendung eines sogenannten MAC-E Filters[1]. Er besteht aus einem elektrostatischen Spektrometer, welches als Energiefilter dient und damit das Spektrum in integrierender Form aufnimmt. Die elektrostatische Barriere erreicht ihren Maximalwert in der Mitte des Hauptspektrometers, der sogenannten 'Analysierebene'. Sie kann jedoch nur die longitudinale Energie der Elektronen analysieren. Daher muss ein geeignetes magnetisches Führungsfeld eine Transformation von transversaler in longitudinale Energie durchführen. Dies ist das Prinzip der magnetischen adiabatischen Kollimation. Diesen MAC-E Filter gilt es hinsichtlich seiner Transmissions- und Untergrundeigenschaften zu optimieren. Dies war das Ziel der vorliegenden Arbeit. Als zentralen Parameter der Simulationen wurde das externe Luftspulensystem LFCS[2] verwendet, um speziell das Magnetfeld den Anforderungen anzupassen.

3. Simulationsprogramme Die Funktionsweise des Spektrometers basiert lediglich auf der Verwendung statischer elektrischer und magnetischer Felder. Daher kann die Berechnung derselben vollständig voneinander entkoppelt werden. Dies ermöglicht es, die Simulationsprogramme hinsichtlich verschiedener Aspekte des elektromagnetischen Designs anzupassen.
In beiden Feldberechnungsroutinen sind zwei unterschiedliche Methoden implementiert, um das magnetische Feld bzw. das elektrostatische Potential in einem Raumpunkt zu berechnen. Dies ist einerseits die Berechnung mit Hilfe elliptischer Integrale und andererseits die Berechnung unter Verwendung der Entwicklung nach Legendre-Polynomen. Mit Hilfe dieser Routinen, und unter Einbeziehung weiterer physikalischer Aspekte wie der Magnetrondrift und der Streuung an Restgasatomen, können Bahnverfolgungssimulationen im gesamten Spektrometer durchgeführt werden.

4. Optimierung der magnetischen Eigenschaften Die hohe Sensitivität des KATRIN Experiments macht ein Spektrometer erforderlich, welches optimale Transmissions- und Untergrundeigenschaften aufweist. Dabei spielt das Magnetfeld eine entscheidende Rolle. Es transportiert die β-Elektronen von der Quelle über eine Distanz von nahezu 70 m bis zum Detektor. Im Spektrometer muss es dafür sorgen, dass die magnetische adiabatische Kollimation ideal vonstatten geht, damit alle Elektronen, welche die Transmissionsbedingung erfüllen, auch tatsächlich transmittiert werden. Desweiteren sollte es in der Analysierebene in radialer Richtung möglichst homogen sein, da die Analysierebene direkt auf den segmentierten Detektor abgebildet wird und zu große Inhomogenitäten zu einer unkontrollierbaren Verbreiterung der Transmissionsfunktion T einzelner Detektorpixel führen kann. Eine wichtige Aufgabe des magnetischen Führungsfeldes ist zugleich die Abschirmung von Elektronen, die sonst von außen in den Flussschlauch eindringen könnten. Im Falle eines perfekt axialsymmetrischen Magnetfeldes ist dies nicht möglich. Im Rahmen dieser Arbeit wurde die

---

[1] **M**agnetic **A**diabatic **C**ollimation and **E**lectrostatic Filter

[2] **L**ow **F**ield **C**orrection **S**ystem

Magnetfeldkonfiguration für das Standarddesign mit einem globalen Magnetfeldminimum in der Analysierebene durch eine Variation der Parameter des Luftspulensystems LFCS optimiert. Es zeigte sich, dass gerade die Transmissionsbedingung schwierig zu erfüllen ist. Daher wurde eine alternative Konfiguration untersucht, bei der in der Analysierebene ein lokales Maximum vorherrscht. Durch die lokalen Minima vor und hinter der Analysierebene gelingt es, die Transmissionsbedingung wesentlich zuverlässiger zu erfüllen. Abbildung 1 zeigt die Magnetfeldstärken entlang verschiedener Feldlinien innerhalb des Flussschlauchs und demonstriert die wesentlichen Unterschiede der beiden Konfigurationen.

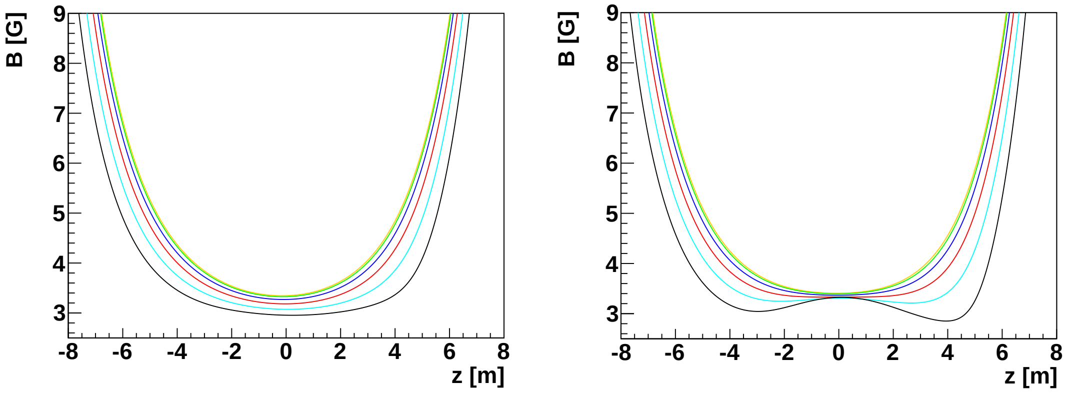

Figure 1: Magnetfeldstärke entlang verschiedener Magnetfeldlinien innerhalb des Flussschlauchs. ***Links***: Konfiguration mit einem globalen Minimum in der Analysierebene ($z = 0$ m). ***Rechts***: Konfiguration mit zwei lokalen Minima vor und hinter der Analysierebene.

Lokale Magnetfeldminima stellen aufgrund des magnetischen Spiegeleffekts potentielle Teilchenfallen dar. Dies wurde mit Hilfe einer Monte Carlo Simulation des Verhaltens von niederenergetischen Elektronen untersucht, welche im Spektrometer isotrop emittiert wurden. Es konnte keine signifikant erhöhte Speicherung, bedingt durch die zwei lokalen Magnetfeldminima, reproduziert werden. Mehr als 90% der Elektronen, die durch die lokalen Minima gespeichert sind, sind auch im Falle eines globalen Minimums aufgrund des gleichen Effekts gespeichert. Diese spezielle Magnetfeldkonfiguration stellt daher eine mögliche Alternative für das KATRIN Experiment dar.

5. Ein System zur Überwachung des magnetischen Führungsfeldes Für eine korrekte Bestimmung der Transmissionsfunktion T ist die bis auf 1% genaue Kenntnis der Magnetfeldstärke, speziell in der Analysierebene, von essentieller Bedeutung. Außerdem muss gewährleistet werden, dass das Magnetfeld ständig allen experimentellen Anforderungen genügt, welche im vorhergehenden Abschnitt kurz erläutert wurden. Daher ist die Implementation eines Systems zur Messung und Überwachung der Magnetfelder der verschiedenen Quellen unerlässlich.
Diese Quellen sind zum einen die Vielzahl supraleitender Magnete im gesamten Experimentaufbau und zum anderen die externen Luftspulensysteme LFCS und EMCS[3].

---

[3] **E**arth **M**agnetic field **C**ompensation **S**ystem

Die am schlechtesten zu beschreibenden, aber nicht vernachlässigbaren Quellen sind die magnetischen Materialien in der unmittelbaren Umgebung des Spektrometers. Ihre Beiträge müssen unter Verwendung realer Messwerte gesondert simuliert werden. Die resultierenden Magnetfeldstärken können mit Hilfe der obigen Simulationsprogramme gezielt für bestimmte Raumpunkte berechnet und mit dort tatsächlich gemessenen Werten verglichen werden. Diese realen Daten werden durch sehr präzise Sensoren ermittelt, welche an Schlüsselpositionen im Experimentaufbau angebracht sind. Sie müssen hohe Anforderungen bezüglich ihrer Positionierung ($\Delta\vec{r} < 0,5$ cm) und Ausrichtung ($\Delta\theta < 0,1^\circ$) erfüllen.

6. Elektronenspeicherung aufgrund einer Kontrollmessung der Quell-Säulendichte Die Transmissionsfunktion T des Spektrometers berücksichtigt keine Wechselwirkungseffekte von β-Elektronen innerhalb der Quelle WGTS. Falls ein Elektron beispielsweise inelastisch an einem Tritiummolekül streut, könnte der resultierende Energieverlust dazu führen, dass es die elektrostatische Barriere im Spektrometer nicht mehr überwinden kann. Die Zählrate am Detektor wird also reduziert. Die resultierende modifizierte Funktion ist die 'Antwortfunktion' des KATRIN Experiments. Sie ist auf der linken Seite von Abbildung 2 zu sehen und zeigt die drei leicht identifizierbaren Bereiche der 0-fachen, 1-fachen und 2-fachen Streuung in der Quelle. Die Streuwahrscheinlichkeit hängt von der Säulendichte ρd in der Quelle ab. Umgekehrt kann somit ρd aus dem Verhältnis der am Detektor gemessenen Raten bei verschiedenen Überschussenergien (schwarze Punkte in Abbildung 2) bestimmt werden.

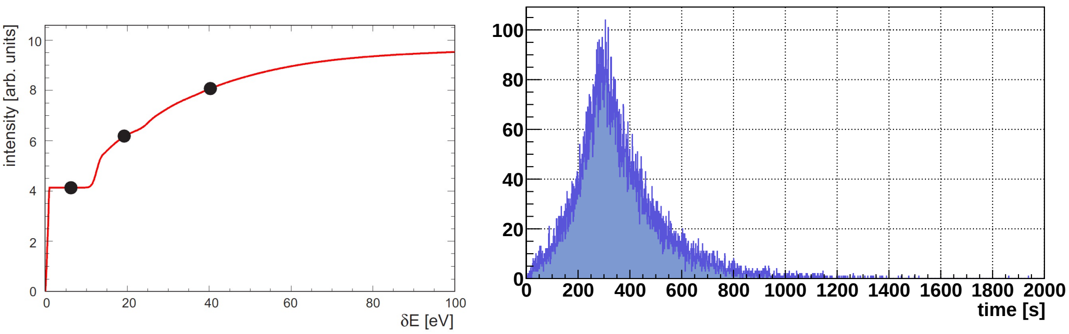

Figure 2: ***Links***: Antwortfunktion des KATRIN Experiments. ***Rechts***: Resultierendes Untergrundspektrum aufgrund einer Messung der Säulendichte der Quelle.

Eine solche, periodisch zu wiederholende Messung, bei der Elektronen von einer Elektronenkanone aus mit den drei Überschussenergien $E = 5$, 20, 40 eV insgesamt 5 Minuten lang durch die Quelle geschickt werden, wurde in dieser Arbeit simuliert. Dafür wurden insgesamt drei Millionen Elektronenbahnen berechnet. Diese Elektronen können an Restgasatomen streuen, was mit einer Veränderung ihres Polarwinkels verbunden ist. Dies kann dazu führen, dass sie innerhalb des Spektrometers durch den magnetischen Spiegeleffekt gespeichert sind. Verlassen diese Elektronen das Spektrometer erst nach Beenden der Vermessung der Säulendichte, so tragen sie zum Untergrund der eigentlichen Tritium-β-Spektrums-Messung bei. Das resultierende Zeit-Spektrum der gespeicherten Primärelektronen ist im rechten Teil der Abbildung 2 zu sehen. Durch den exponentiellen Abfall nimmt die Rate zu großen Zeiten hin schnell ab. Ein ähnliches Spektrum ergibt sich bei der Betrachtung der Sekundärelektronen, welche durch Ionisation der Restgasatome entstehen. Jedoch ist die hieraus resultierende Rate am Detektor geringer. Innerhalb einer Zeitspanne von wenigen Minuten nach der Messung ist somit insgesamt eine intollerable Erhöhung der Rate im mHz-Bereich zu erwarten. Konsequenterweise dürfen die von dieser erhöhten Rate betroffenen Detektorpixel bei der Analyse der β-Spektrums-Messdaten für eine Zeitdauer von etwa 10 Minuten im Anschluss an die ρd-Vermessung nicht berücksichtigt werden. Dies soll innerhalb der Testphase des Hauptspektrometers verifiziert werden.

7. Zusammenfassung und Ausblick Zusammenfassend kann man festhalten, dass es mit Hilfe der sehr vielfältigen und präzisen Simulationssoftware möglich war, die magnetische Konfiguration für das Hauptspektrometer zu optimieren. Desweiteren wurde demonstriert, dass Monte Carlo Simulationen eine geeignete Methode zur Untersuchung der elektromagnetischen Eigenschaften des Spektrometers darstellen. Wichtige Speichereffekte konnten untersucht und mögliche Alternativen bereitgestellt werden.

Da jedoch nicht alle Effekte durch die Simulationsprogramme berücksichtigt werden können, müssen diese im Rahmen ausführlicher Testmessungen verifiziert werden. Zudem wird die Software durch neue Erkenntnisse ständig erweitert und verbessert werden. Nur dadurch ist zu gewährleisten, dass das elektromagnetische Design des Hauptspektrometers den hohen Anforderungen des KATRIN Experiments gerecht wird und somit eine Bestimmung der Neutrinomasse mit einer bisher unerreichbaren Sensitivität ermöglicht.

Contents

List of Figures

List of Tables

1. Introduction

Since its invention by W. Pauli in 1930 [1], the properties of the neutrino have been studied intensively. But even 80 years later, open questions remain. It is not known if the neutrino is its own antiparticle or which specific mass scale and mass pattern is realised in nature. Together with photons the neutrinos are the most numerous particles in the universe. They are of importance for cosmology which is focused on the evolution of the universe, especially the formation of large scale structures. An upper limit on the sum of all neutrino masses $\sum_i m_{\nu_i}$, $i = 1, 2, 3$ can be derived from cosmological observations. But due to the huge parameter space available for their analysis, it would be of great importance to have the neutrino mass as an input parameter. Therefore, direct and model-independent methods are needed. So far, the investigation of the tritium-beta-decay revealed the best upper limit on the mass of the electron-antineutrino [2][1]:

$$m_{\bar{\nu}_e} < 2.2 \ \frac{\mathrm{eV}}{\mathrm{c}^2}. \tag{1.1}$$

As a successor experiment, the KATRIN experiment [3] will improve the present accuracy by one order of magnitude down to a sensitivity of $m_\nu < 0.2$ eV. This does not only ask for a larger experiment but also for a very detailed understanding of background processes and other systematical effects on the beta-spectrum. Statistical and systematical uncertaintites have to be confined to $\sigma^2 < 0.017$ eV^2. To keep the systematical uncertaintites at a minimum, each subsystem has to be stable on a 0.1% level. Therefore, relevant experimental parameters such as the column density of the source or the magnetic field within the whole KATRIN setup have to be monitored.

The main emphasis of the present work is on very detailed simulations of the electromagnetic properties of the KATRIN spectrometers, especially regarding trapping effects. Therefore, after an introduction to neutrino physics in this chapter and to the KATRIN experiment in chapter 2, the simulation tools will be presented in chapter 3. In particular, the configuration of the magnetic field has to be adjusted to reach the best transmission properties possible while keeping the background at a minimum. This will be discussed in detail in chapter 4. Due to the high stability required for all parameters of the electromagnetic setup, the magnetic field has to be monitored permanently. The challenges of this task will be outlined in chapter 5 and a possible solution will be presented. The last chapter 6 will be concerned with the simulation of a measurement using an electron gun with a high rate. Particle tracking simulations were used to determine the additional background resulting from this measurement. Such measurements are needed for calibration and monitoring purposes. The monitoring measurement of the source column density will thus be presented exemplary.

---

[1] Within this work, the unit [eV] will be used for masses. c^2 will not be stated explicitly.

1.1 The Beginning of Neutrino Physics

In 1930 physicists such as Niels Bohr [4] were ready to abandon energy conservation. They could not explain the continuous energy spectrum of β-decay

$$n \rightarrow p + e^- \tag{1.2}$$

of nuclei otherwise. Instead of a monoenergetic line at a fixed energy E_{max}, as expected for a two-body decay, electrons of all energies between 0 and E_{max} were found. W. Pauli was able to save energy conservation by suggesting a three-body decay

$$n \rightarrow p + e^- + \bar{\nu}_e \tag{1.3}$$

with a hypothetical, electrically neutral particle with a spin quantum number $s = 1/2$. This particle takes away the missing energy. He introduced it as 'neutron' in his famous letter *"Dear radioactive ladies and gentlemen..."* to his colleagues at a conference in Tübingen [5]. But when Chadwick used this name shortly thereafter for the neutral constituent of a nucleus [6], Enrico Fermi, who was the first to explain the β-decay theoretically, renamed it 'neutrino' [7].

Because neutrinos are subject to gravitation and weak interactions only, they are hard to detect and to study. Therefore, it took about 25 years until Fred Reines and Clyde Cowan finally managed to prove their existence within the series of "Poltergeist" experiments [8]. They made use of the inverse β-decay reaction

$$\bar{\nu}_e + p \rightarrow e^+ + n \tag{1.4}$$

in water (H_2O), where the electron-antineutrinos $\bar{\nu}_e$ were provided in great quantity by the nearby Savannah River reactor.
The emitted positron in (1.4) quickly annihilates with an electron into two monochromatic 511 keV photons which can then be detected with photomultiplier tubes (PMT). Furthermore, cadmium-chloride ($CdCl_2$) was added to the water. The neutron scatters off the water molecules, slowing down until it is captured by a cadmium nucleus. This excited Cd^* goes back to its ground state by emitting a high-energy delayed gamma signal. Both signals together serve as clear delayed coincidence signature.
They found an extremely small cross section of $\sigma = (1.1 \pm 0.3) \cdot 10^{-43}\ \mathrm{cm}^2$ [1], underlining the weak interaction rate of neutrinos.

In 1962 Ledermann, Steinberger and Schwartz found evidence for a second neutrino type, the myon neutrino ν_μ [9] and in 2000 the DONUT experiment at Fermilab finally completed the picture with their proof of the existence of the tau neutrino ν_τ [10].

The fact that there are no further active neutrino flavours (with $m_\nu < 45$ GeV) was established by experiments at the LEP accelerator at CERN [11]. They measured the decay width of the Z^0 boson which is a mediator of the weak interaction the neutrinos are subject to and thus fixed out current picture of the standard model families.

1.2 Neutrinos in the Standard Model

The Standard Model (SM) [12] contains all known matter particles and describes their strong, weak and electromagnetic interaction through exchange currents. The origin of gravitation and its hypothetical exchange boson of spin $s = 2$, the graviton, are not explained within the Standard Model.
According to the Standard Model, all matter is made of 12 fermions and their antiparticles which can be grouped as in figure 1.1.

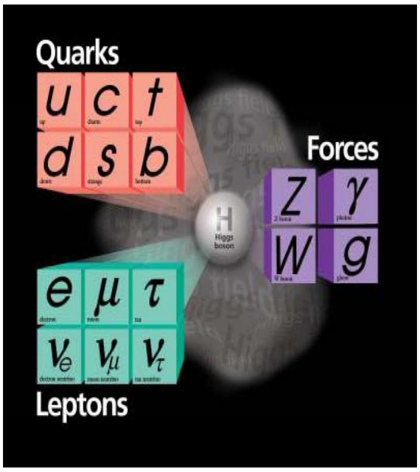

Figure 1.1: Particles of the Standard Model.

There are two types of fermions to distinguish, leptons and quarks. They can be further split up into three so-called 'generations'.

The quarks appear as six different 'flavour' states, each with three different 'colours'. Each generation can be ordered by their increasing mass.
The quark states are the only particles in the Standard Model to experience all four fundamental interactions, and whose electric charges are not integer multiples of the elementary charge, i.e. $+\frac{2}{3} \cdot e$ for up, charm and top quark and $-\frac{1}{3} \cdot e$ for down, strange and bottom quark. Their colour charge is mediated by gluons and causes them to participate in the strong interaction. Furthermore, quarks can not be found isolated, because of the so-called 'colour confinement'. When separating two quarks from each other, the increasing quark-quark potential at some point has enough energy to create a quark-antiquark pair.

For the leptons, each generation consists of a (weak) isospin doublet of electron, muon or tau and their corresponding neutrino ν_e, ν_μ, ν_τ. The charged leptons are subject to both, weak and electromagnetic interactions. The neutral neutrinos experience the weak interaction only, mediated by the Z^0 and $W^\pm$ bosons.

The Higgs boson is the only Standard Model particle which has not been observed yet. Its detection would confirm theoretical considerations on the mass-generation mechanism for the elementary particles in the universe. However, in the scheme of neutrinos being Majorana particles, it is possible for right-handed neutrinos to have a mass M of their own without relying on the Higgs boson. Therefore, this mass can be very large, which, in return, allows the existence of left-handed neutrinos with a very small mass m due to the so-called seesaw-mechanism.

In 1958 Goldhaber measured the helicity of the neutrino [13], i.e. the orientation of its spin with respect to its momentum. He found neutrinos to have negative helicity only. An interesting conclusion is the fact that neutrinos, having a definite helicity, travel with the speed of light and hence, have to be massless. Otherwise, there would be a reference frame for which the momentum changes direction and hence the helicity changes as well.

1.3 Beyond the Standard Model

During the last decade, the hints for a non-zero neutrino mass have proliferated. Particularly the observation of neutrino oscillations, i.e. the transformation of one neutrino flavour into another, has confirmed Pontecorvo's idea of neutral lepton oscillations. To allow for this phenomenon, the flavour-eigenstates $|\nu_\alpha\rangle$, where $\alpha = e, \mu, \tau$, d not coincide with the mass-eigenstates $|\nu_i\rangle$, where $i = 1, 2, 3$, but can be obtained by the following relation

$$|\nu_\alpha\rangle = \sum_i U_{\alpha i} \, |\nu_i\rangle \, . \tag{1.5}$$

$U_{\alpha i}$ represents the unitarity mixing matrix[2] which is the analogue of the CKM quark mixing matrix.
Therefore, neutrinos do not have a fixed mass but are in a state where different mass terms $|\nu_i\rangle$ can interfere with each other. This interference is an analogue to the interference of de Broglie waves. The probability for a transition from a specific flavour-eigenstate α to another state β is given in vacuum by

$$P_{\alpha\to\beta} = \left| \sum_i U^*_{\alpha i} U_{\beta i} e^{-i\Delta m^2_{ij} L/2E} \right|^2 , \quad \Delta m_{ij} = m_i - m_j , \tag{1.6}$$

where L is the pathlength and E the total energy of the neutrino.

The first confirmation of neutrino oscillations was provided by the Super-Kamiokande[3] experiment in 1998 [14]. A detector filled with 50 kt of pure water and equipped with thousands of PMTs was placed underground to detect atmospheric ν_e or ν_μ.
Inside the volume they can scatter off a proton and produce electrons or muons via a charged current reaction. These secondary particles travel with superluminal velocity and thereby produce a Cerenkov light cone. The event topology allows to distinguish electron neutrinos ν_e from muon neutrinos ν_μ and to determine the direction they came from.

---

[2] Leptonic mixing matrix, also PMNS matrix, named after **M**aki, **N**akagawa, **S**akata, who introduced it, and **P**ontecorvo, who created the theoretical foundation for neutrino oscillations.

[3] Super-Kamiokande: Successor experiment to Kamiokande (**Kamioka** **N**ucleon **D**ecay **E**xperiment), originally meant for the detection of proton decay, which is running since April 1996 in the Kamioka mine in Japan.

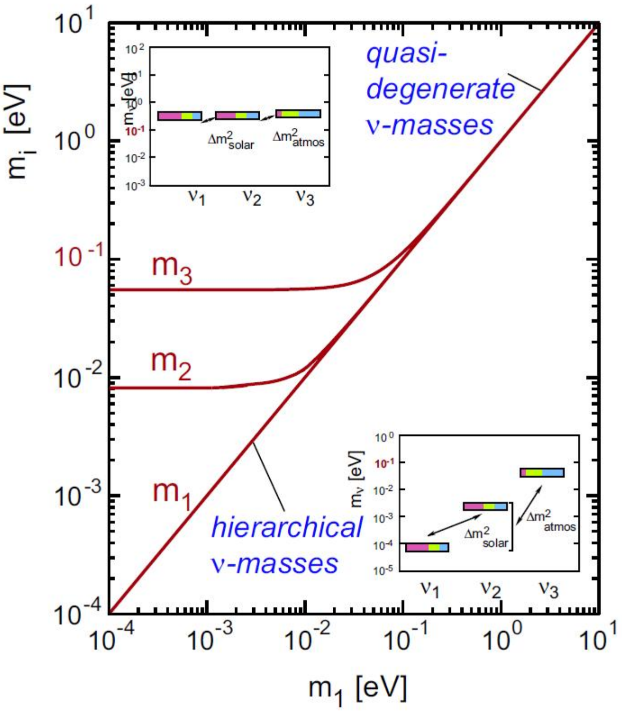

Figure 1.2: Neutrino mass eigenstates m_i, $i = 1, 2, 3$ as a function of the lightest eigenstate m_1. The graph shows a 'normal hierarchy' for $m_1 < m_2 < m_3$ and a 'quasi-degenerate model' for $m_1 \approx m_2 \approx m_3$. The small boxes visualize the impact of neutrino oscillation measurements. The mass differences can be determined by solar and atmospheric oscillation experiments. The colors correspond to the different flavour contributions resulting from the PMNS mixing matrix.

The experiment found a deficit of muon neutrinos crossing the Earth relative to those coming from the atmosphere directly above the detector. This can be explained by neutrino oscillations $\nu_\mu \to \nu_\tau$ during the flight through the Earth. As the detector has a very low efficiency in detecting ν_τ, this effect results in a ν_μ deficit while ν_e are unaffected.

Neutrino oscillations were also responsible to solve the so-called 'solar neutrino problem' [15]. Due to nuclear fusion reactions inside the sun

$$4p \to {}^4\mathrm{He} + 2e^+ + 2\nu_e \tag{1.7}$$

a constant flux of ν_e with an energy of less than 20 MeV is expected on the Earth. Different experiments, amongst others Homestake [16], Super-Kamiokande [17] and GALLEX [18]/GNO [19], measured a flux which was smaller by a factor of two to three than the theoretically expected one. This long-standing problem was finally solved by the **S**udbury **N**eutrino **O**bservatory SNO [20]. The SNO detector, equipped with 1,000 tons of heavy water (D_2O), was able to measure the total number of neutrinos of all types. The results showed that most of the neutrinos, which were produced as electron neutrinos inside the sun, are changed into muon and tau neutrinos by the time they reach the Earth. In the case of solar neutrinos, the flavour transformation relies on the so-called MSW effect [21], [22], where matter effects result in a resonant transformation of ν_e into $\nu_{\mu,\tau}$.

However, neutrino oscillation experiments can only determine the mass differences Δm_{ij}^2 of two neutrino mass eigenstates i, j. The knowledge of one mass eigenstate would thus be sufficient to determine the other mass eigenstates. Figure 1.2 shows the development of the different mass eigenstates as a function of the lightest mass eigenstate m_1. Therefore, other methods have to be looked for to fix the absolute neutrino mass scale.

1.4 Indirect Methods for Neutrino Mass Determination

There are several ideas on how to measure the mass of the neutrino indirectly. The most sensitive approaches, the search forneutrinoless double-β-decay and cosmological observations, will be summarised in the following.

Neutrinoless Double Beta Decay

In a double-β-decay process two β-decays happen simultaneously in the same nucleus (Z,A):

$$(Z, A) \ \rightarrow \ (Z + 2, A) + 2e^{-} + 2\bar{\nu}_e. \tag{1.8}$$

This process was observed for the first time in 1987 [23]. In a neutrinoless double-β-decay ($0\nu\beta\beta$) process the neutrinos are not being emitted but exchanged as virtual particles between the two neutrons undergoing β-decay. The observation of this hypothetical process would imply that the neutrino is its own antiparticle. This follows from the fact that the first neutron emits an antineutrino, while the second neutron can only interact weakly with a neutrino. Therefore, if a neutrinoless double-β-decay would be observed the neutrino would be a Majorana particle. Furthermore, parity is maximally violated in weak interactions [24], [25]. During the β-decay of a neutron an antineutrino with a right-handed chirality (positive helicity) is emitted. For the inverse β-decay of the second neutron, it has to be absorbed as a neutrino with left-handed chirality (negative helicity) [26]. For a massless neutrino, chirality is the same as helicity. But if the neutrino has a mass, they have to be distinguished. The weak interaction is related to chirality which, in turn, is related to the γ^5 matrix in Dirac spinor space. Helicity, however, is related to physical space and hence, it is frame dependent, i.e. the observer can find a reference frame for which the neutrino appears to move backwards resulting in a reversed helicity.

In $0\nu\beta\beta$ searches the half life $t_{1/2}$ of the decay is the observable. Only in the framework of a detailed calculation of the core matrix element for the nucleus under investigation the neutrino mass can be determined. More precisely, it is not the neutrino mass itself that is being measured ,but an effective majorana mass $m_{\beta\beta}$. This mass consists of the coherent sum of neutrino mass eigenstates m_i:

$$m_{\beta\beta} = \left| \sum_{i=1}^{3} U_{ei}^2 m_i \right|. \tag{1.9}$$

The Heidelberg-Moskow experiment has studied the decay of enriched germanium

$$^{76}\mathrm{Ge} \ \rightarrow \ ^{76}\mathrm{Se} + 2e^{-}(+2\bar{\nu}_e). \tag{1.10}$$

in a well-shielded underground setup. In 2002, a subgroup of the Heidelberg-Moskow collarobration claimed to have found evidence for a majorana neutrino mass $m_{\beta\beta} \approx 0.4$ eV [27]. This result is heavily disputed among the community [28]. Therefore, several experiments, for example GERDA [29], CUORE [30] and EXO [31], are being planned and partly already assembled to confirm or disprove this result.

Cosmology and Astrophysics

An attractive method to determine the sum of the neutrino mass eigenstates $\sum_{i=1}^{3} m_i$ is given by looking at the evolution of large-scale structures in the universe. This section will give a short overview of the different analysis methods which have been used to set an upper limit on this sum.

The study of the cosmic microwave background (CMB) allows astro-physicists to make a precise statement on the composition of the universe. Figure 1.3 shows the different contributions to the overall energy density of the universe. CMB satellite experiments like COBE [32] and WMAP [33] have measured a nearly perfect black body spectrum corresponding to a temperature $T = (2.735 \pm 0.025)$ K. This spectrum results from the photons which decoupled from matter 380,000 years after the Big Bang when the universe cooled down to a temperature where atomic hydrogen could form. Much earlier in time (after 0.1 s) the neutrinos were able to decouple in the same manner. Therefore, in analogy to the photon background, a relic neutrino background is expected. These neutrinos have not been detected so far because of their very low energies and cross sections. They interact extremely weakly and hence should reflect the properties of the early universe when they were free-streaming relativistically as hot dark matter. An investigation of the results of free-streaming by neutrinos can, in turn, give information about the mass of relic neutrinos.

Additional observations of the structure formation in the recent universe at low redshifts z reveal that dark matter mainly consists of ‘cold dark matter’. These particles were non-relativistic at the time of their decoupling. In comparison, ‘hot dark matter’, in the form of light neutrinos which were relativistic at the time of decoupling, washed out small structures. But small structures are still being observed by a measurement of the redshift of galaxies, e.g. with the 2dFGRS[4] or the SDSS[5]. Therefore, these observations allow to put a constraint on the neutrino mass.

Another approach to the neutrino mass is the investigation of the so-called Lyman-α forest. Photons, which were emitted by quasars at a certain redshift z, can map out large-scale structures due to the significant quasar distance to the Earth. In doing so, they have to pass many hydrogen clouds and a photon might get absorbed by the molecules inside. All clouds finally reemit radiation, but depending on their distance to the Earth the absorption lines will be found at different wavelengths. The distribution of these absorption lines can be converted into a distribution of hydrogen clouds in a certain line of sight. This distribution, in turn, reveals information on the structure formation of the universe and thus the neutrinos mass.

According to reference [33] the WMAP-5 data reveal a neutrino mass limit

$$\sum_{\nu} m_{\nu} < 0.67 \text{ eV} \quad (95\% \; C.L.). \tag{1.11}$$

Because of the huge parameter space required to constrain neutrino masses together with many other cosmological parameters, the analysis results for the sum of the neutrino masses vary between 0.2 eV and 2 eV. These indirect methods are strongly

---

[4] **2 d**egree **F**ield **G**alaxy **R**edshift **S**urvey [34]

[5] **S**loan **D**igital **S**ky **S**urvey [35]

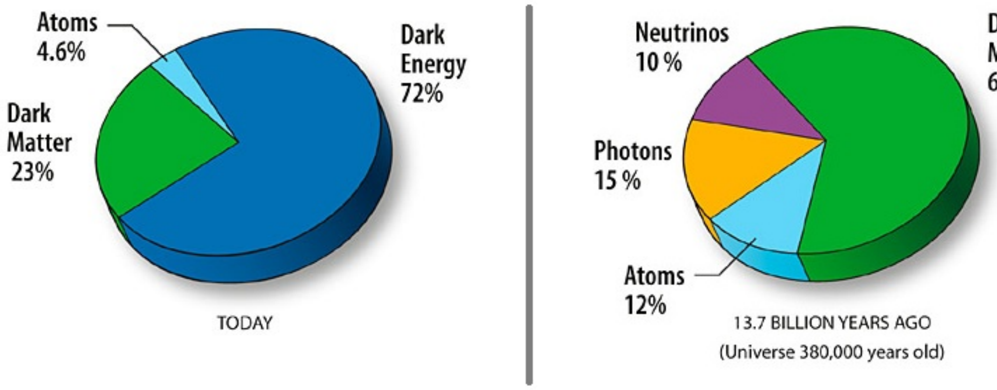

Figure 1.3: Energy composition of the universe today and at the time of recombination. The right graphic shows the beginning of the matter-dominated phase of the universe shortly after the decoupling of neutrinos and photons (recombination). Today the universe is dominated by Dark Energy, the driving force for its accelerated expansion.

model-dependent and an external input for the neutrino mass by direct methods such as the tritium β-decay would be of significant impact for cosmology.

1.5 Direct Methods for Neutrino Mass Determination

The most sensitive method to determine the neutrino mass is the investigation of the kinematics of weak decays. The experimental method relies on momentum and energy conservation only, so model-independent conclusions about the neutrino mass can be drawn. In comparison to searches for $0\nu\beta\beta$ or cosmological studies, this method is the only model-independent approach to determine the 'mass of the electron-antineutrino'.

1.5.1 Kinematics of β-decays

The 'mass of the electron-antineutrino' $m_{\bar{\nu}_e}$ can be determined by a measurement of the exact shape of the β-spectrum in the region close to the endpoint E_0.

In a β^--decay process, the weak interaction converts a neutron into a proton while emitting an electron and an electron-antineutrino as seen in equation (1.3) and figure 1.4. The energy released is distributed between the three decay products. The mass of the remaining nucleus is in a first order approximation treated as infinitely large in comparison to the mass of the electron and the neutrino. Therefore, the energy is split between the electron and the neutrino where the neutrino takes away the energy $E_\nu = \sqrt{m_\nu^2 c^4 + p_\nu^2 c^2}$. The maximum kinetic energy of the electron is thus reduced by the finite rest mass of the neutrino.

The energy distribution of the decay electrons can be calculated with the help of Fermi's Golden Rule [7]

$$T = \frac{\mathrm{d}^2 N}{\mathrm{d}t\,\mathrm{d}E} = \frac{2\pi}{\hbar}|\mathcal{M}|^2 \rho(E). \tag{1.12}$$

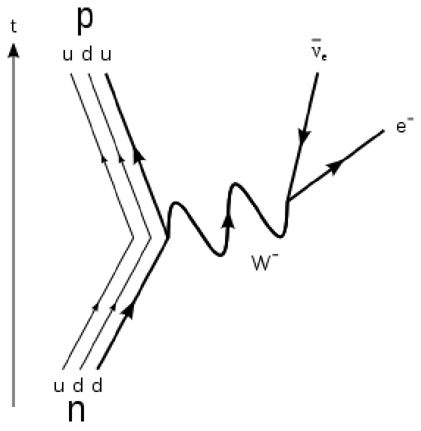

Figure 1.4: Feynman diagram for a β^--decay process.

The transition rate T depends on the strength of the coupling between the initial and final state of the system and on the number of ways this transition can happen, i.e. the density of the final states $\rho(E)$. A transition will proceed more rapidly if the coupling between the initial and final state is stronger. The coupling term is called the matrix element $\mathcal{M}$ for the transition. This leads to the following relation

$$\frac{\mathrm{d}N}{\mathrm{d}E} = R(Z,E) \cdot (E_0 - E) \cdot \sqrt{(E_0 - E)^2 - m_{\bar{\nu}_e}^2 c^4} \cdot \Theta(E_0 - E - m_{\bar{\nu}_e} c^2), \tag{1.13}$$

where

$$R(Z,E) = \frac{G_F^2}{2\pi^3 \hbar^7} \cdot \cos^2(\theta_C) \cdot |\mathcal{M}|^2 \cdot F(Z,E) \cdot p \cdot (E + m_e c^2) \tag{1.14}$$

contains several kinematic parameters and fundamental constants, namely

G_F : Fermi coupling constant
M : transition matrix element
p : electron momentum
E_0 : endpoint energy of β-spectrum
$m_{\bar{\nu}_e}$: neutrino rest mass.
Θ_C : Cabibbo angle
F : Fermi function
m_e : electron mass
E : electron kinetic energy

The step function $\Theta(E_0 - E - m_{\bar{\nu}_e} c^2)$ accomodates that a neutrino can only be produced if the available energy is larger than its rest mass.
Both $\mathcal{M}$ and $F(Z,E)$ are independent of $m_{\bar{\nu}_e}$, therefore the influence on the spectrum comes mainly from the phase space factor

$$(E_0 - E) \cdot \left[(E_0 - E)^2 - m_{\bar{\nu}_e}^2 c^4\right]^{1/2} .$$

In principle, the neutrino mass could be determined just by looking at the difference between the measured endpoint energy and the expected endpoint Q which can be seen in figure 1.5. However, both values can not be measured with a sufficiently high precision. Therefore, the influence of the neutrino mass on the shape of the spectrum up to a few eV below the endpoint has to be measured. In this region, neutrinos are non-relativistic and their momentum-energy relation can be probed.

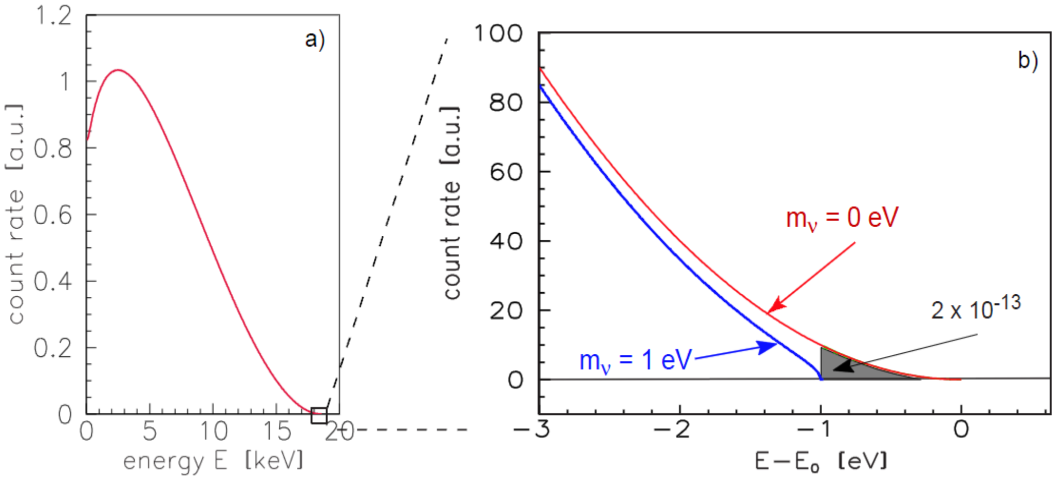

Figure 1.5: Electron energy spectrum of β^--decay. ***Left***: Complete spectrum. ***Right***: Narrow region around the endpoint.

1.5.2 Tritium β-decay experiments

Tritium as β-emitter

The choice to use tritium as a β-emitter is based on several important facts:

1. **Low endpoint energy**: $E_0 \approx 18600$ eV. The fraction of β-decay electrons in the endpoint region rises with $1/E_0^3$. Hence, for a small Q value of the source material the count rate close to the endpoint is relatively large.

2. **Short half life**: $t_{1/2} = 12.3$ a. The amount of tritium needed to reach a sufficiently high count rate is reduced substantially, in particular with regard to ^{187}Re (see next section).

3. **Super-allowed process**, transition between mirror nuclei:

$$^3_1\mathrm{H} \rightarrow \, ^3_2\mathrm{He}^+ + e^- + \bar{\nu}_e. \tag{1.15}$$

   No corrections from the matrix element $\mathcal{M}$ have to be taken into account. The matrix element is energy independent and has a rather large value.

4. **Electronic structure**: Due to the low Z value of tritium and its related nuclei ^{3}He$^+$, T$_2$, THe$^+$ their electronic structure is rather simple and can be computed with high precision. This is important for the neutrino-mass analysis, as the electronic structure has an impact on the β-spectrum.

5. **Inelastic scattering**: As tritium is a low Z nucleus, the fraction of decay electrons undergoing inelastic scattering on the molecules in the source is relatively small. A fraction of 41.3% of all β-electrons reach the spectrometer without energy loss. This will be of importance for the simulations discussed in chapter 6.

Previous results

Tritium β-decay experiments are realised for more than 50 years already. The best results come from the Mainz [36] and Troitsk [37] experiments:

$$\text{Mainz: } m(\bar{\nu}_e) \leq 2.3 \text{ eV} \;\; (95\%\,\text{CL.}); \;\; \text{Troitsk : } \; m(\bar{\nu}_e) \leq 2.5 \text{ eV} \;\; (95\%\,\text{CL.}). \tag{1.16}$$

Both experiments used the same principle of an electrostatic spectrometer the **KA**rlsruhe **TRI**tium **N**eutrino experiment [3] is going to use. A detailed insight into this part of the experiment will be given in the next chapter.
The KATRIN experiment will push the sensitivity of tritium β-decay experiments to the technological limits and will have an improved sensitivity of 0.2 eV.

1.5.3 Rhenium β-decay experiments

Another rather promising candidate for an investigation of the kinematics of β-decay is Rhenium. The great advantage of ^{187}Re over tritium is its low endpoint energy of $Q = 2.47$ keV. This ensures that a large fraction of the β-electrons carries useful information on the spectrum. On the other hand, due to its large half-life time of $T_{1/2} = 4.32 \cdot 10^{10}$ y, a large amount of Rhenium is required for a source with a sufficiently high activity.

The measurement principle is complementary to that of tritium β-decay. The Milano experiment [38] used an array of several thermal microcalorimeters which served as both, source and detector at the same time. A β-decay of ^{187}Re leads to an energy deposition inside the calorimeters. The resulting rise in temperature can be read out by thermistors. The Milano collaboration published an upper limit on the neutrino mass of

$$m_{\bar{\nu}_e} < 15 \text{ eV} \;\; (90\%\text{C.L.}). \tag{1.17}$$

The successor experiment MARE [39] aims to improve this sensitivity down to $m_\nu = 3$ eV. The great advantage is the modularity of the bolometers. New calorimeters can easily be added, however, this requires that the bolometer performance of each detector element is known precisely.

2. The KATRIN Experiment

The objective of the **KA**rlsruhe **TRI**tium **N**eutrino experiment [3] is a model-independent determination of the mass of the electron-antineutrino with a sensitivity of 0.2 eV (90% CL.) [3], which is an improvement of one order of magnitude compared to predecessor experiments. As the experimental observable is $m^2_{\bar{\nu}_e}$, this corresponds to an improvement by two orders of magnitude with regard to key experimental parameters.
This chapter gives an overview of the experiment. To gain information on the β-spectrum a special type of spectrometer is needed. To reach the design sensitivity, this spectrometer has to fulfil stringent requirements which will be discussed thoroughly.

2.1 Measurement Principle

To determine the 'mass of the electron-antineutrino' $m_{\bar{\nu}_e}$, the electron energy spectrum of tritium β-decay has to be measured very precisely close to its endpoint E_0. This general idea was already outlined in chapter 1.5.
As a geberal principle, the kinetic energy E of the β-electrons will be measured with a spectrometer which is put on a high electric potential U. Only those electrons with enough kinetic energy to pass this potential barrier will be detected. All others will be reflected. By varying the potential difference between the spectrometer and the electron source the β-spectrum will be scanned and an integrated spectrum will be obtained. The spectrometer acts as an integrated high-pass filter.

2.1.1 MAC-E Filter

The high sensitivity of KATRIN of 0.2 eV can only be reached with a spectrometer of high solid angle acceptance, low background and high energy resolution in combination with a stable, ultra-luminous tritium source. This spectrometer is based on the MAC-E filter[1] principle, which was proposed for the first time in [40]. The main features of the MAC-E filter are illustrated in figure 2.1.

Superconducting magnets at both ends of the spectrometer create a magnetic guiding field to transport the β-electrons. The β-electrons enter from the source side with an accepted solid angle of 2π. Due to the Lorentz force they perform a cyclotron motion around the magnetic field lines until they reach the detector. The electrons have to be guided adiabatically, i.e. the gradient of the magnetic field should not be too steep and the electrons should not be too fast, otherwise the magnetic guidance would be lost.

A novel design feature of MAC-E filters is the idea to put the spectrometer vessel on high voltage and to install a system of cylindrical and conical electrodes inside

---

[1] **M**agnetic **A**diabatic **C**ollimation combined with an **E**lectrostatic filter

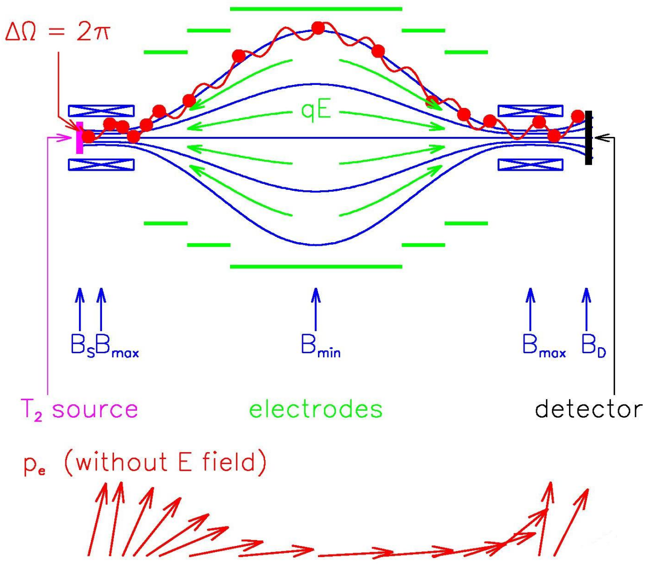

Figure 2.1: MAC-E filter principle. Upper part: blue - magnetic guiding field; green - electrostatic potential; red - cyclotron motion of electrons. Lower part: Transformation of electron momentum vector due to inhomogeneous magnetic field.

the spectrometer. Together they create an electrostatic retarding potential which has its maximum value U_0 in the middle of the spectrometer. This area is hence named 'analysing plane'. Accordingly, the potential is zero at the position of maximum magnetic field. This electrostatic field decelerates electrons moving towards the analysing plane and reaccelerates them up to their starting energy after they passed it. The most important aspect is that this potential only affects the longitudinal energy $E_{||}$ of the electrons, i.e. the fraction of the kinetic energy tangential to the magnetic field line it is guided on.

Therefore, an inhomogeneous magnetic guiding field is needed. During their motion towards the analysing plane of KATRIN, the magnetic field drops by more than four orders of magnitude. The resulting magnetic gradient force

$$\vec{F}_{\nabla} = \vec{\nabla}(\vec{\mu} \cdot \vec{B}) \tag{2.1}$$

transforms most of the transversal energy $E_{\perp}$, which causes the cyclotron motion, into longitudinal energy $E_{||}$ tangential to the magnetic field lines. This is visualized by the momentum vector in figure 2.1. If the electron has a longitudinal energy larger than zero in the analysing plane, i.e. $E_{||} > qU_0$, it will be guided to the detector, otherwise it will be reflected.

Because of their cyclotron motion, electrons have an orbital magnetic moment

$$\mu = \frac{e}{2m_e} \left| \vec{l} \right| = \frac{E_{\perp}}{B}. \tag{2.2}$$

During one cyclotron period the magnetic field changes slowly and the momentum gets transformed adiabatically. Therefore the magnetic moment keeps constant[2]. Furthermore, the retarding potential slows down the electrons by converting their kinetic energy into potential energy. This is important to guarantee an adiabatic motion of the electrons in low magnetic fields.

An important aspect of β-spectroscopy is the fact that the electrons are emitted isotropically in the source. If they start with a large polar angle θ they have to travel a long distance in the source due to their cyclotron motion. Therefore, the probability for inelastic scattering on the tritium molecules is very high. Due to their energy loss in this process they would distort the β-spectrum. Therefore, the source is put in a magnetic field $B_S = 3.6$ T, which is lower than the maximum magnetic field $B_{max} = 6$ T. If the polar starting angle of an electron is too large, the magnetic gradient force will transform all its longitudinal energy into transversal energy and the electron will get reflected. The maximum accepted starting angle θ_{max} can be calculated:

$$\sin\theta_{max} = \sqrt{\frac{B_S}{B_{max}}} \quad \rightarrow \quad \theta_{max} = 50.77^\circ. \tag{2.3}$$

This value is small enough to suppress most of the electrons which experienced an inelastic scattering event, but still large enough to allow for a sufficiently high count rate.

The MAC-E filter acts as an integrating high-pass filter. The region around the endpoint of the β-spectrum will be scanned by varying the electrostatic retarding potential.

The relative sharpness of this filter can be derived directly from equation (2.2) by looking at the points of maximum and minimum magnetic field, B_{max} and $B_{min} = B_A$[3]:

$$\frac{\Delta E}{E} = \frac{B_A}{B_{max}}. \tag{2.4}$$

ΔE in this case characterizes the energy interval for which the transmission of electrons increases from 0% to 100%. By putting the design values into equation (2.4) the width of this interval can be calculated

$$\Delta E = E_{\perp,min} = E_{\perp,max} \cdot \frac{B_A}{B_{max}} = 18600 \text{ eV} \cdot \frac{3 \cdot 10^{-4} \text{ T}}{6 \text{ T}} = 0.93 \text{ eV}. \tag{2.5}$$

This is the width of the transmission function displayed in figure 2.2. Following equations (2.2), (2.3) and (2.4) this normalised transmission function can be calculated analytically by

$$T(E, qU) = \begin{cases} 0 & E - qU < 0 \\ \frac{1-\sqrt{1-\frac{E-qU}{E}\cdot\frac{B_S}{B_A}}}{1-\sqrt{1-\frac{\Delta E}{E}\cdot\frac{B_S}{B_A}}} & 0 \le E - qU \le \Delta E \\ 1 & E - qU > \Delta E \end{cases}, \tag{2.6}$$

where U denotes the retarding potential, E the energy of the isotropic electron source and q the electron charge. Figure 2.2 shows the fraction of transmitted electrons as a

---

[2] non-relativistic approximation; for relativistic particles $(\gamma + 1) \cdot E_\perp / B$ is an adiabatic invariant of the motion, where γ denotes the relativistic factor

[3] B_A denotes the magnetic field in the analysing plane.

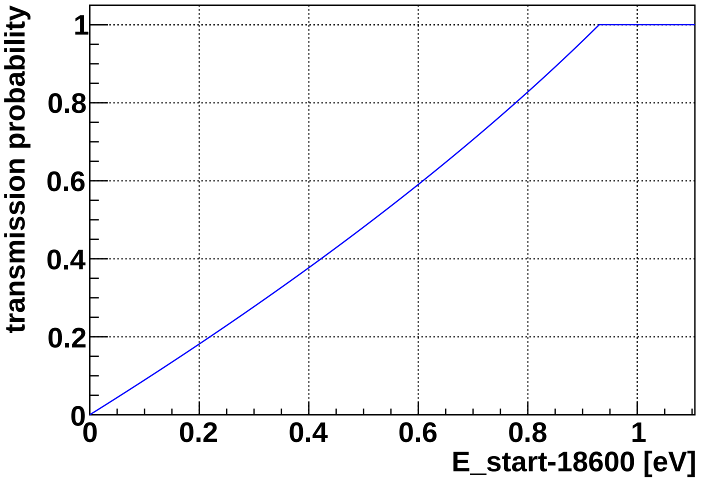

Figure 2.2: Transmission function for electrons isotropically emitted from the source, moving along the beam-axis, i.e. $x = 0$ and $y = 0$, and $B_{min} = 3$ G, $B_{max} = 6$ T, $U_{ret} = 18.6$ keV. Due to the suppression of all electrons with a starting angle larger than 51° a maximum of 42% of all emitted electrons can reach the detector. This effect was already taken into account for this normalised transmission function.

function of their starting energy. The probability for an electron to be transmitted is an interplay of its starting kinetic energy and its starting angle. If an electron has only a small excess energy its polar starting angle has to stay below a certain limit. Otherwise, the transformation from transversal into longitudinal energy will not be sufficient and it will get reflected. It is a great advantage that this function has no tails towards lower or higher energies and is only dependent on the ratios B_A/B_{max} and B_S/B_A of the magnetic field strengths.

The influence of the magnetic field configuration on the transmission properties will be discussed in more detail in section 4.2.

2.2 Setup

All tritium decay experiments use basically the same setup. There are four main components which are shown in figure 2.3 and which will be described in the following. These are *a)* the source where the β-electrons are being created, *b)* the transport section to filter out the tritium molecules, *c)* the spectrometer section to analyse the energies of the β-electrons and *d)* the detector to count the transmitted β-electrons.

2.2.1 Source

A high luminosity molecular tritium source (WGTS[4]) will provide 10^{11} β-electrons per second during the standard operation mode. Molecular tritium gas of high purity (>95%) and very low temperatures ($T = 27$ K) will be injected in the middle of the

---

[4] **W**indowless **G**aseous **T**ritium **S**ource

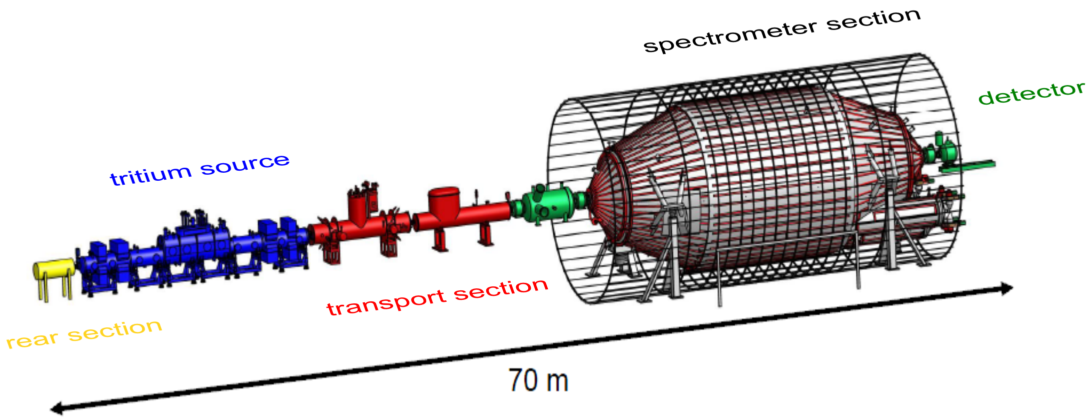

Figure 2.3: Schematical view of the KATRIN experimental setup with a total length of 70 m. The tritium decays in the tritium source releasing the β-electrons. The transport section guides the electrons to the spectrometer tandem setup. The pre-spectrometer filters out all those low energetic electrons that do not carry any usable information on the neutrino mass. The main spectrometer measures the region around the endpoint very precisely. The detector detects single electron events. The graphic does not show the monitor spectrometer which is needed for the observation of the high voltage stability of the main spectrometer.

10 m long WGTS tube and pumped off at both ends by turbomolecular pumps to be reinjected in a closed tritium cycle. The gas injection pressure p_{in} allows adjustment of the column density ρd. For a value of $p_{in} = 3.4 \cdot 10^{-3}$ mbar and a source tube temperature $T = 27$ K, the reference value for the column density can be calculated:

$$\rho d = 5 \cdot 10^{17} \frac{\text{molecules}}{\text{cm}^2}. \tag{2.7}$$

To keep the systematic uncertainties at a minimum this parameter has to be known to a precision of 0.1% and will be measured repeatedly. Chapter 6 will be discuss this subject in more detail.

The electrons, isotropically emitted from the tritium molecules, are guided adiabatically by the WGTS magnetic field of $B_S = 3.6$ T to both ends of the tube. On the rear side a **C**ontrol and **M**onitor **S**ection (CMS) will be installed [41]. It consists on the one hand of a rear detector to monitor the source activity and a rear WGTS plate to control plasma effects and the electrostatic potential within the source tube. On the other hand, a high intensity electron gun will be installed with the following purposes:

- Measurement of spectrometer transmission function.
- Measurement of inelastic scattering characteristics inside the gaseous source.
- Investigation of systematic effects from beam transport.

On the opposite front side of the WGTS the electrons enter the transport section.

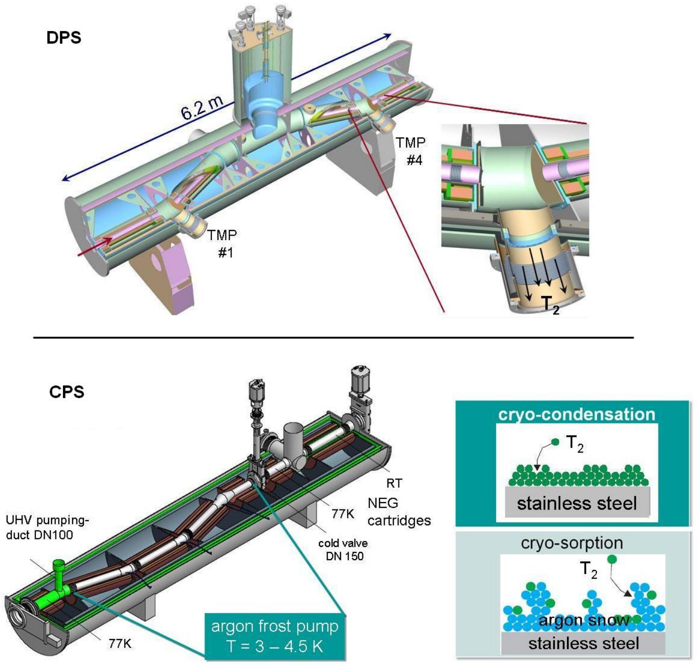

Figure 2.4: Schematical view of the transport section parts. Top: DPS tube and its 4 turbomolecular pumps to pump out the tritium actively. Bottom: CPS tube cooled down to $3-5$ K to allow for a passive absorption of tritium on the inner surface of the tube. Furthermore, a coverage with argon frost increases the surface and enhances the trapping probability. Both systems contain tubes that are tilted against each other to form a barrier for the outflowing tritium. The electrons are guided around by the magnetic field.

2.2.2 Transport System

The transport system has to guide the β-electrons to the spectrometer while suppressing tritium molecules flowing out from the source at the same time. It is divided into two parts, an active **D**ifferential **P**umping **S**ection (DPS) and a passive **C**ryogenic **P**umping **S**ection (CPS), shown in figure 2.4.

Inside the spectrometer a partial pressure of tritium of about 10^{-20} mbar is needed to keep the background generated by tritium decay below 10^{-3} counts/s. Therefore the tritium flow has to be suppressed by a factor of 10^{11} between the outlet of the WGTS tube and the entrance of the pre-spectrometer. This will be achieved by a combination of active pumping with turbomolecular pumps in the DPS and absorption of tritium on the ultra-cold inner surface of the beam tube in the CPS.

2.2.3 Spectrometers

There are three different spectrometers used in the KATRIN setup, the pre-spectrometer, the main spectrometer and the monitor spectrometer. They are all based on the MAC-E filter principle, described in section 2.1, but have different purposes which will be illustrated in this section.

Pre-spectrometer

The pre-spectrometer will be operated at a fixed retarding potential of 18.3 keV. All electrons with lower energies, which do not carry useful information on the neutrino mass, will be reflected by this potential. This will reduce the electron flux into the main spectrometer by a factor of 10^7, minimising the background from ionization of residual gas.

Main Spectrometer

In the main spectrometer the endpoint of the β-spectrum will be scanned with an energy resolution of 0.93 eV. An extremely low level of background is needed. Therefore, the vacuum requirements of $p < 10^{-11}$ mbar are very stringent to reduce the possibility for scattering, and most importantly, ionisation events inside the sensitive volume. Since this work focuses mainly on the investigation and improvement of the electromagnetic design of the main spectrometer, a more detailed overview will be presented in section 2.3.

The pre-spectrometer as well as the main spectrometer use the vacuum vessel itself to carry the retarding high voltage. To suppress background from the inner surface of the spectrometer walls a nearly massless inner wire electrode system will be installed. If put on a slightly more negative potential it will redirect low-energy muon-induced electrons back to the walls. This leads to an additional background suppression by a factor of 10^2, thus adding to the dominant magnetic shielding factor of 10^5. In addition, the inner wire electrodes will fine-tune the electrostatic field to avoid the occurrence of penning traps[5] in corners and to optimise the adiabatic transmission properties of the MAC-E filter.

Monitor Spectrometer

In addition to the 70 m long KATRIN beam line a second, shorter 5 m long beam line will be installed. This beam line consists of a krypton-source, which emits monoenergetic electrons, another spectrometer and a segmented silicon based PIN-diode array as detector. The spectrometer, which is the modified Mainz spectrometer, will be fed with the same retarding high voltage as the main spectrometer and thus provides an on-line monitoring of its stability.
To minimise magnetic stray fields from one beam line towards the other, the two setups are separately assembled at two different buildings.

2.2.4 Detector

The electron detector is placed within the second solenoid behind the main spectrometer. It will count all electrons transmitted through the electrostatic filter. Therefore, a very low background is required there. This low background will be achieved by an active and passive detector shielding.
A good energy resolution[6] will allow for a discrimination of background as well. The detector needs to be very sensitive to low electron rates, but also needs to be able to handle high rates from calibration sources such as an electron gun. Therefore, a silicon-based semiconductor detector (Si-PiN array) will be used. To increase the efficiency of the detector a post-acceleration of electrons up to 30 keV is being investigated.

---

[5] Particles can be stored in penning traps using a strong homogeneous axial magnetic field to confine these particles radially and a quadrupole electric field to confine them axially. While other experiments create these traps on purpose to investigate particles, they are an intrinsic source of background in a spectrometer of MAC-E type.

[6] The detector used in the final setup will have an energy resolution of ≈ 600 eV for electron energies of 18.6 keV.

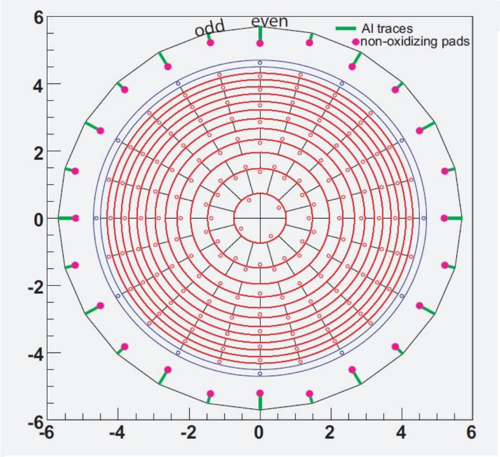

Figure 2.5: Schematical view of the segmentation of the Focal Plane Detector taken from [42]. The 144 segments of the Si-PiN diode array are shown. They are analysed independently to take into account radial inhomgeneities of the electric and magnetic fields.

A very important property is the segmentation of the detector which is shown in figure 2.5. A radial and axial segmentation allows for an independent analysis of each pixel. This is necessary due to the radial inhomogeneities of the electric and magnetic fields. The sizes of the segments are adjusted so that each element has the same surface area, while the radial subdivision follows the expected inhomogeneity of the retarding potential in the analysing plane.

2.3 Main Spectrometer and Air Coil System

In order to achieve the sensitivity KATRIN is aiming for, the magnetic and electric fields in the main spectrometer have to fulfil certain requirements which will be discussed in detail in chapter 4, which is based on [43]. This section intends to give an overview of the influences of the magnetic field on the electromagnetic design of the main spectrometer. In particular, a large air coil system will be motivated and presented in the following.

The magnetic guiding field in the main spectrometer is mainly defined by the superconducting magnets used within the setup. The sensitive flux tube of 191 Tcm^2 is defined by the source magnetic field and the diameter of the source tube. While the field has a strength of 4.5 T (source side) to 6 T (detector side) near the magnets, it drops down to approximately 3 G in the analysing plane[7]. Therefore, low magnetic stray fields and especially the Earth's magnetic field can no longer be neglected there. Its influence ($B_E = 0.48$ G, inclination 64.7°, declination 1.0° [44]) results in significant transverse shifts of electron tracks as shown in figure 2.6.

The disadvantages of this initial setup are on the one hand a reduced count rate at the detector, because β-electrons are hitting the inner electrodes or the vessel wall while

---

[7] In this work the unit T (Tesla) will be used for high magnetic field regions close to the superconducting coils; the unit G (Gauss) will be used for low magnetic field regions around the analysing plane; the relation is given by $1\ \mathrm{G} = 10^{-4}\ \mathrm{T}$.

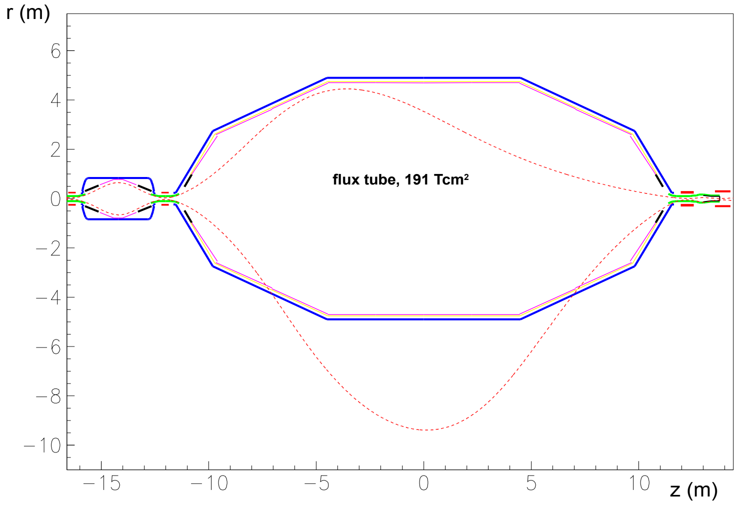

Figure 2.6: Flux tube (design value 191 Tcm^2), transporting electrons through the pre- and main spectrometer, without any corrections. *Red rectangles*: superconducting magnets; *Green*: ground potential; *Blue*: vessel on high potential; *Red/yellow*: inner electrodes on high potential; *Dashed*: outer magnetic field lines of flux tube. The flux tube is too large and asymmetric, both facts are disadvantageous for the transmission of electrons and would result in enhanced levels of background.

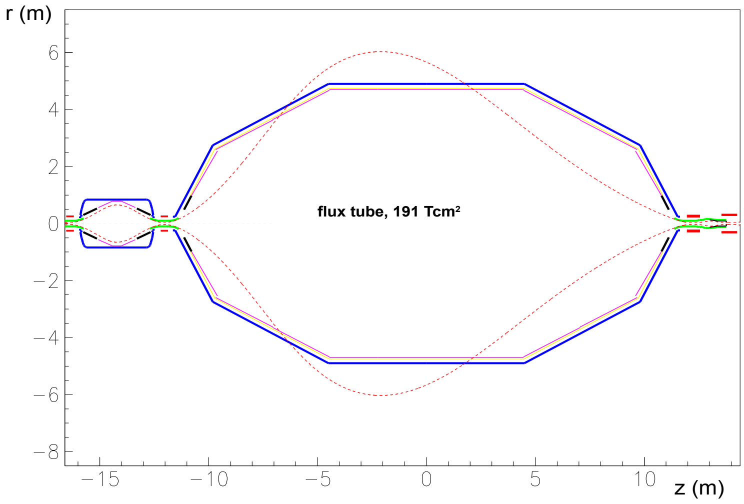

Figure 2.7: Flux tube (design value 191 Tcm^2) with correction by the EMCS. It is now axially symmetric but still too large leading to a reduced count rate and an increased background from electrons emitted in the central spectrometer surface.

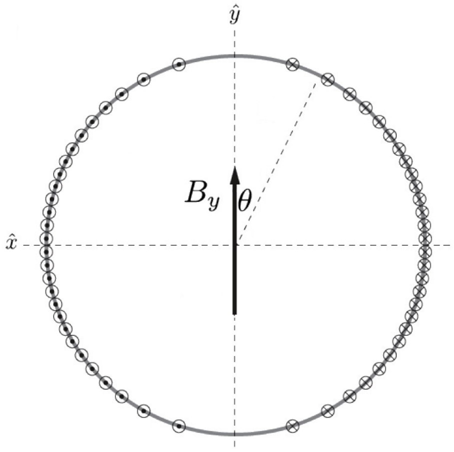

Figure 2.8: Creation of homogeneous magnetic fields. A very homogeneous magnetic field in a large volume can be achieved if the positions of the cables on a cylindrical surface in a way that the $\cos\theta$ is equally distributed over the cross section.

moving along one of the outer magnetic field lines. On the other hand, the background would increase due to electrons emitted from the walls which are entering the flux tube and are then guided to the detector. Therefore, two coil systems [45] have to be implemented to shape the magnetic field in an optimum way.

2.3.1 Earth Magnetic field Compensation System

The first field-shaping action is the implementation of an Earth Magnetic field Compensation System (EMCS). It will compensate the vertical (y-direction, $B_{E_y} = -436$ mG) and the non-axial horizontal (x-direction, $B_{E_x} = 35$ mG) component of the Earth's magnetic field. The resulting flux tube will be of the shape as shown in figure 2.7.
Because each field component has to be compensated separately, the EMCS will consist of two coil systems. The windings will be arranged axially along the main spectrometer. Arranging the system in the well known $\cos\theta$ current distribution (for illustration, see figure 2.8) will lead to a good homogeneity inside the sensitive spectrometer volume. All windings of one particular system carry the same current. A detailed motivation and description of these systems and their realisation can be found in the design document for the air coil system [43], which was edited in the framework of the present thesis, and in [46], [47]. The basic layout is based on the proposals in [48] and [49].

2.3.2 Low Field Correction System

Even though the flux tube is much more axially symmetric after compensation of the Earth's magnetic field, the above mentioned problems persist. In the low field region the flux tube exceeds the radial dimensions of the main spectrometer vessel. Therefore, another coil system has to be implemented, the Low Field Correction System (LFCS). It compresses the flux tube such that it fits inside the vessel, thereby allowing for a full transmission of all electrons from the source to the detector while shielding electrons, which are emitted from the walls, from the detector. This will be adressed in chapter 4. With both systems working as intended, the flux tube will be shaped as shown in figure 2.9.

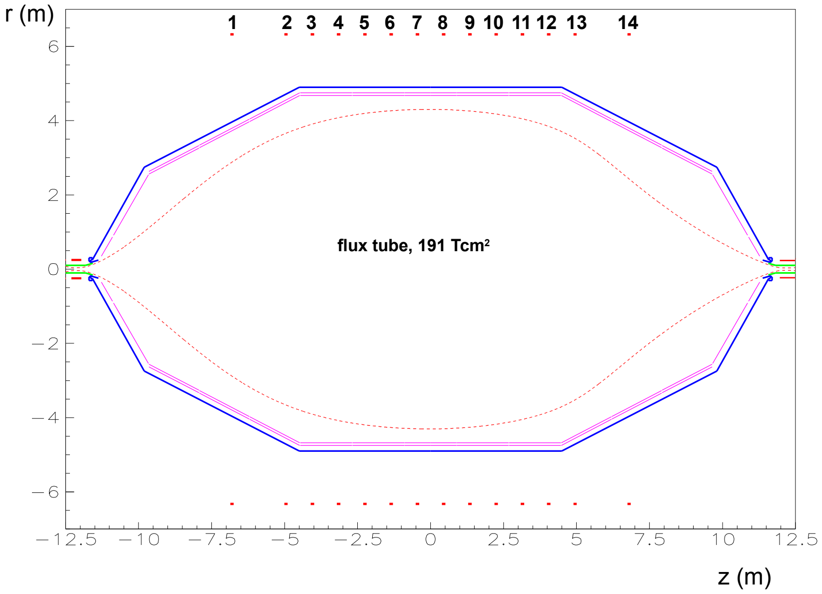

Figure 2.9: Flux tube (design value 191 Tcm^2) with corrections by EMCS and LFCS. Ideally, the flux tube is perfectly axially symmetric and the outer field lines keep a safety distance from the inner electrodes.

Mechanical setup

Numerical calculations, described in [50], [51] and chapter 4, have shown that a set of 15 independent coils with a diameter of 12.6 m are needed in order to fulfil the electromagnetic design requirements. A schematic view of the systems can be found in figure 2.10 and a picture of the actually installed systems is given in figure 2.11. Additional technical drawings can further be found in appendix A.

While coils 1-13 increase the magnetic field strength, there are two coils at the detector side with a current flow in opposite direction leadind to a strong decrease of the magnetic field in this region. This is an essential design requirement because of the asymmetry in the magnetic field strength arising from the different solenoids used in the setup. The magnetic moments of the detector-side superconducting magnets are larger by a factor of 2 than those of the source-side magnets. Therefore, the magnetic field strength increases faster towards the detector side.

An alternative design, where the mechanical structure as sketched in figure 2.10 is also used for carrying the current, was investigated in [52] and [53]. Aluminium rings made of rectangular profiles would be isolated electrically to form a single-loop coil with the ability to carry a large current, up to a few hundred Ampere, with very small resistance and power consumption. The decision to not implement this LFCS configuration was taken for various reasons:

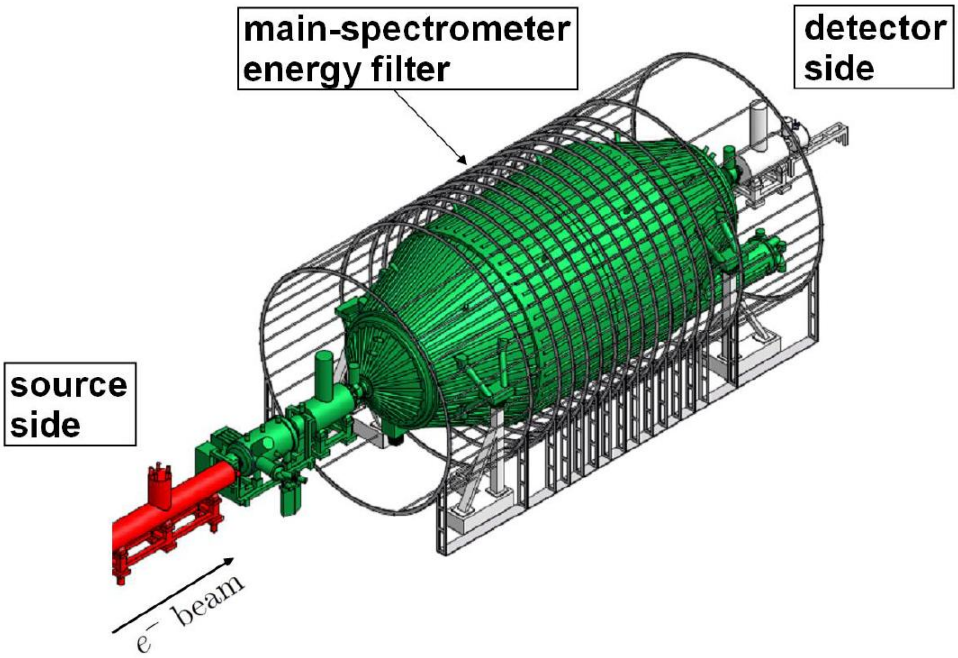

Figure 2.10: Schematical view of the main spectrometer vessel surrounded by the LFCS (vertical) and the EMCS (horizontal + end ring connections).

1. The required insulation of statically important parts makes the mechanical setup more difficult and expensive
2. supplying the high currents is much more expensive
3. low self induction of a one-turn coil makes the operation less stable than with more turns.

The structure described above instead serves as a holding structure for aluminium cables with a cross section of 70 mm^2 and a PE (polyethylene) insulation. They can be bent easily while short sections do not sag. All coils will consist of several cables which have to be joined. All power supplies are at one location in the hall and the two supply cables of each coil will be run closely together to avoid unwanted magnetic stray fields.

The LFCS has to fulfil certain magnetic design requirements, which will be discussed in chapter 4. Calculations have been performed in order to define the ampere turns values[8] for the different coils in order to fulfil these requirements. The results can be found in the same chapter. These values, together with a minimisation of the operating costs, define the number of turns and the maximum current of the individual coils. In order to be able to find an optimum magnetic field configuration, very precise simulation tools are needed and will be presented in the following chapter.

---

[8] The ampere turns value At is defined as the product of current I and number of loops N, i.e. $At = I \cdot N$.

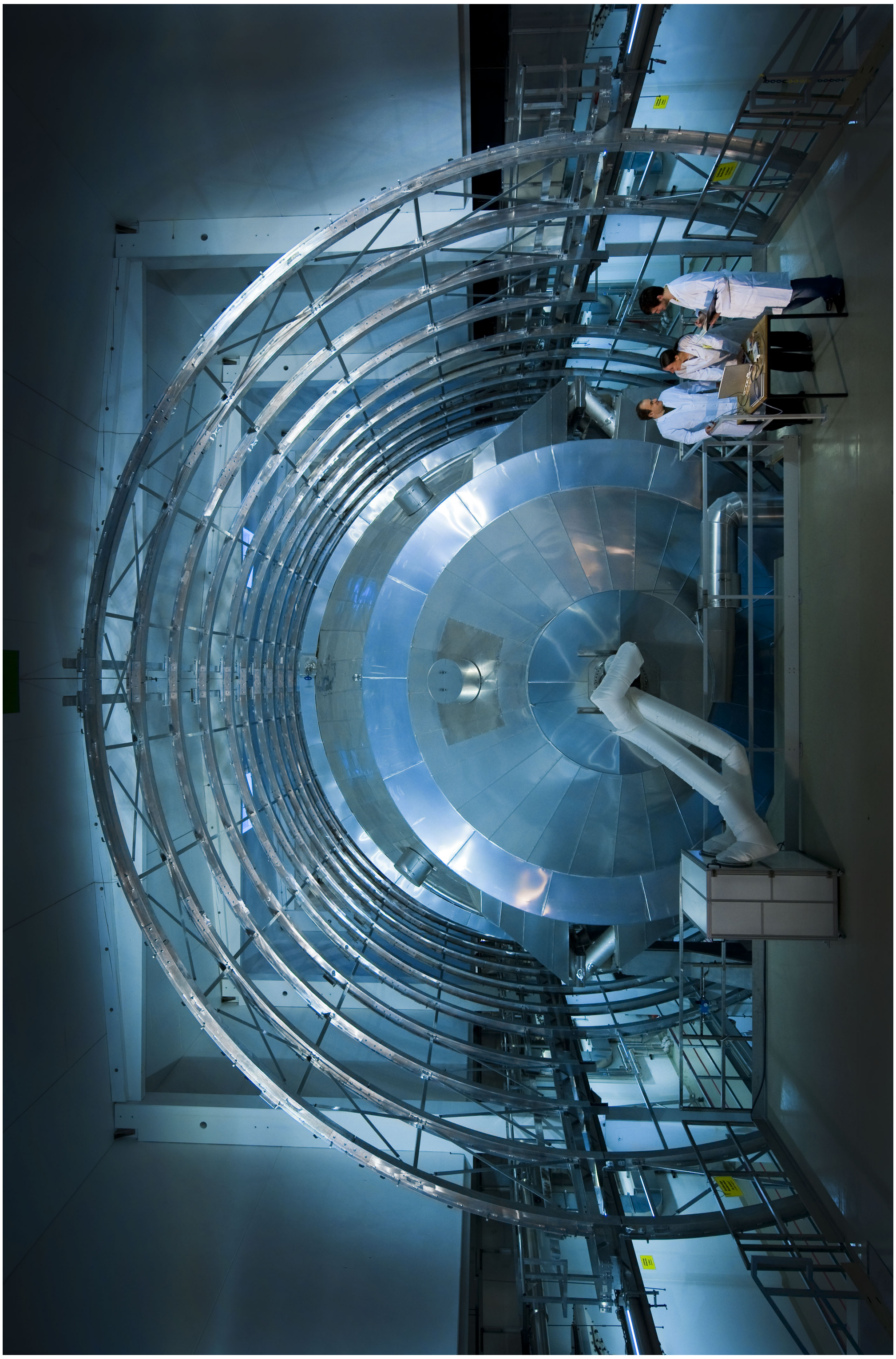

Figure 2.11: A photograph of the main spectrometer vessel surrounded by the LFCS structure, taken in September 2009.

3. Simulation Tools

This diploma thesis is focused on detailed calculations and simulations for the optimisation of the electromagnetic design of the main spectrometer and air coil system of the KATRIN experiment. The simulation tools used were developed by F. Glück at the Karlsruhe Institute of Technology (KIT). This code, written in the C programming language, was adapted by F. Fränkle [54] to develop a particle tracking routine for the spectrometer section.

The functionality of the spectrometer parts of the KATRIN experiment is based on static electric and magnetic fields only. Therefore, their calculation, which will be described in the first two sections of this chapter, can be decoupled completely. This facilitates an adaptation to the various problems. While the effects of different electric and magnetic configurations can be investigated separately, the output of both calculations can be combined to allow for trajectory calculations of charged particles, in particular electrons. This will be discussed in the last section of this chapter.

3.1 Magnetic Field Calculations

The magnetic field, generated by an electric current running through a coil, can be calculated according to the Biot-Savart law:

$$\mathrm{d}\vec{B} = -\frac{\mu_0}{4\pi}\frac{I\vec{r}\times\mathrm{d}\vec{s}}{r^3}, \tag{3.1}$$

where $\mathrm{d}\vec{B}$ is the net magnetic field, induced by an electric current I running through the differential element $\mathrm{d}\vec{s}$ of a wire, which points in the direction of conventional current. Accordingly, $\vec{r} = r\hat{\vec{r}}$ is the full displacement vector from the wire element to the point at which the field is being computed and μ_0 is the magnetic permeability constant.

The magnetic field in the KATRIN experiment is created by locally axially symmetric circular coils. Their cross section is of rectangular shape in the $z - r$ meridian plane[1] as shown in figure 3.1. The complete coil can then be obtained by a rotation of these rectangles around the z-axis. There are two completely different methods for the magnetic field calculation available to the user, which will be explained in the following.

---

[1] Throughout the whole document, the positive z-direction is defined along the beam axis from the source to the detector. The x-coordinate points in horizontal direction, perpendicular to the beam axis, and the y-coordinate denotes the vertical direction. For axially symmetric calculations, a calculation of the radial component $r = \sqrt{x^2 + y^2}$ is sufficient.

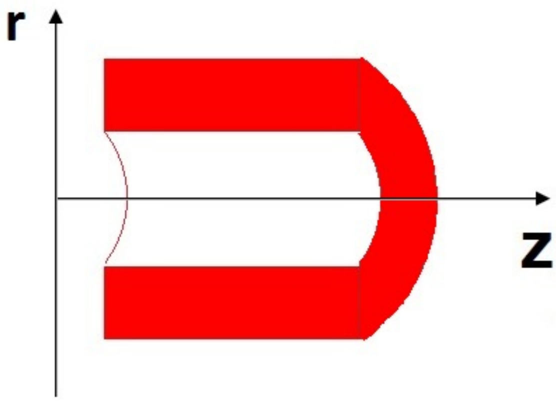

Figure 3.1: Cross section of a coil. .

3.1.1 Elliptic Integrals

The magnetic field components of a circular coil can be expressed by the first (I) and second (II) complete elliptic integrals:

$$\begin{aligned} (I)\quad K(k) &= \int\limits_0^{\pi/2} \frac{\mathrm{d}\theta}{\sqrt{1-k^2\sin^2\theta}} \\ (II)\quad E(k) &= \int\limits_0^{\pi/2} \sqrt{1-k^2\sin^2\theta}\,\mathrm{d}\theta. \end{aligned} \tag{3.2}$$

For a thick coil, a two-dimensional numerical integration of the Biot-Savart law (3.1) along the axial and the radial coil dimensions is needed, making the calculation rather slow. Therefore, also the third complete elliptic integral is being used:

$$(III)\quad \Pi(n,k) = \int\limits_0^{\pi/2} \frac{\mathrm{d}\theta}{(1-n\sin^2\theta)\sqrt{1-k^2\sin^2\theta}}. \tag{3.3}$$

The problem is now reduced to a one-dimensional integration in radial direction. According to [55], the magnetic field components in axial and radial direction can then be calculated analytically by

$$B_z = \hat{B}_z(Z_{max}) - \hat{B}_z(Z_{min}), \quad B_r = \hat{B}_r(Z_{max}) - \hat{B}_r(Z_{min}), \tag{3.4}$$

with

$$\hat{B}_z(Z) = -\frac{\mu_0\lambda}{\pi} \cdot \frac{(z-Z)R}{(R+r)\sqrt{(R+r)^2+(z-Z)^2}} \left[K(k) + \frac{R-r}{2R}(\Pi(n,k) - K(k)\right], \tag{3.5}$$

$$\hat{B}_r(Z) = -\frac{\mu_0\lambda}{\pi} \cdot \frac{R}{\sqrt{(R+r)^2+(z-Z)^2}} \left[2\frac{E(k)-K(k)}{k^2} + K(k)\right] \tag{3.6}$$

and

$\lambda = \mathrm{d}I/\mathrm{d}z$:	linear current density,
z:	axial position of the field point to be calculated,
Z:	$Z \in [Z_{min}, Z_{max}]$, which represents the axial thickness of the solenoid,
R:	$R \in [R_{min}, R_{max}]$, which represents the radial thickness of the solenoid,
r:	radial position of the field point to be calculated.

There are several methods suitable for the calculation of the elliptic integrals, namely the arithemtic-geometric mean method [56], the Chebyshev approximation [57] and Carlson's method [58]. While the first two are only concerned with a calculation of the $K(k)$ and $E(k)$ elliptic integrals, $\Pi(n, k)$ can be calculated by Carlson's method. Field points close to the z-axis have to be handled with care in order to avoid singularities and numerical cancellations [59]. The advantage of the elliptic integral method is that it is possible to calculate the magnetic field everywhere, even inside the coil windings. In return, the computation time is large. For fast trajectory calculations, another method should be used, the zonal harmonic expansion.

3.1.2 Zonal Harmonic Expansion

It is a special property of an axially symmetric coil system that the magnetic field in an arbitrary off-axis point (z, r), which is not far from the axis point $(z_0, 0)$, can be computed by using the derivatives B_n^{cen} $(n = 1, 2, \ldots)$ of the magnetic field in the axis point [60]. The variable B_0^{cen} denotes the magnetic field itself. The axis point $(z_0, 0)$ is called *source point*, the numbers B_n^{cen} are called *central source coefficients.* These coefficients depend on the properties of the coils, i.e. their geometry and the current. The axial and radial magnetic field components in a field point (z, r) can be computed by the following series:

$$\begin{aligned} B_z &= \sum_{n=0}^{\infty} B_n^{cen} \left(\frac{\rho}{\rho_{cen}}\right)^n P_n(u), \\ B_r &= -s \sum_{n=1}^{\infty} \frac{B_n^{cen}}{n+1} \left(\frac{\rho}{\rho_{cen}}\right)^n P_n'(u), \end{aligned} \tag{3.7}$$

where $\rho_{cen} = \sqrt{(z - z_0)^2 + r^2}$ is the minimum distance between the source point z_0 and the source and $s = \sin\theta = \sqrt{1 - u^2} = r/\rho$. This is visualised in figure 3.2. The zonal harmonics $\rho^n P_n(u)$ (of order n) are a general solution of the Laplace equation for an axisymmetric system in vacuum; $\rho^n P_n'(u)$ denotes their first derivatives.

The number of terms that has to be calculated in these series depends on the convergence ratio ρ/ρ_{cen}. If it is small, the expansion converges fast. Therefore, only a small number of terms has to be calculated in order to achieve sufficient accuracy for the magnetic field components. To cover a large region, many source points with different convergence circles have to be defined. For a certain magnetic field configuration these source points are being calculated prior to the calculation of the magnetic field components and stored to a file. In order to have a fast convergence of the Legendre polynomial expansion, the source point with the smallest convergence ratio ρ/ρ_{cen} has to be searched for.

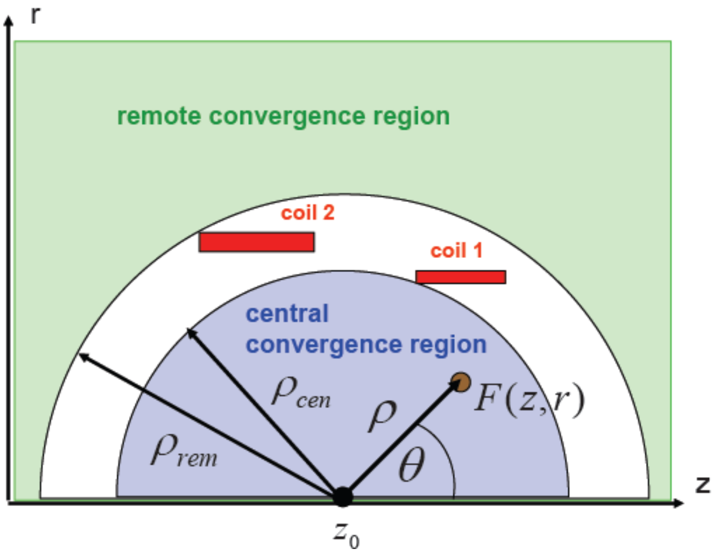

Figure 3.2: Central and remote convergence circle. The central/remote Legendre polynomial expansion is convergent for field points inside/outside its convergence circle, colored in blue/green).

This central Legendre polynomial expansion is appropriate for field points (z, r) that are not far from the source point $(z_0, 0)$. Otherwise, ρ/ρ_{cen} could happen to be larger than 1 and the central expansion would not be convergent. Fortunately, there is the so-called remote Legendre polynomial expansion, which is useful for field points far from the coil. The magnetic field components can be calculated as follows:

$$\begin{aligned} B_z &= \sum_{n=2}^{\infty} B_n^{rem} \left(\frac{\rho_{rem}}{\rho}\right)^{n+1} P_n(u), \\ B_r &= -s \sum_{n=2}^{\infty} \frac{B_n^{rem}}{n} \left(\frac{\rho_{rem}}{\rho}\right)^{n+1} P_n'(u), \end{aligned} \tag{3.8}$$

where ρ_{rem} is the maximum distance between the source point z_0 and the source. The B_n^{rem} $(n = 2, 3, \ldots)$ are the *remote source coefficients*, which represent the magnetic field sources inside the remote region. $\rho^{-(n+1)}P_n(u)$ denotes the zonal harmonics of the remote expansion. As for the central expansion, the series converges fast if the convergence ratio ρ_{rem}/ρ is small and if it is larger than 1 the remote expansion can not be used for a calculation of the magnetic field components.

This method is much faster than the calculation with elliptic integrals, making it the preferred method for field calculations. However, there are regions close to or inside a coil where neither the central nor the remote Legendre polynomial expansion are convergent. In these regions the programme switches automatically to the elliptic integral method at the cost of an increased computation time.

3.1.3 magfield2.c

The programme *magfield2* [61] is designed to compute the magnetic field and vector potential of a coil system with one common symmetry axis[2]. Before starting the calculation, the user has to define the geometry and current parameters of the coils. This is done in an input file with the following structure:

N_{coil}				
$\mathrm{z}_{mid}[1]$	$\mathrm{r}_{in}[1]$	thick[1]	length[1]	current[1]
$\vdots$	$\vdots$	$\vdots$	$\vdots$	$\vdots$
$\mathrm{z}_{mid}[\mathrm{N}_{coil}]$	$\mathrm{r}_{in}[\mathrm{N}_{coil}]$	$\mathrm{thick}[\mathrm{N}_{coil}]$	$\mathrm{length}[\mathrm{N}_{coil}]$	$\mathrm{current}[\mathrm{N}_{coil}]$

where N_{coil} is the number of coils in the configuration, z_{mid} is the middle z-value of a certain coil, r_{in} its inner radius, *thick* its radial thickness, *length* its length in z-direction and *current* the total current[3] running through the coil. All values are given in SI units, i.e. in [m] and in [A]. A visualisation of these parameters can be found in figure 3.3.

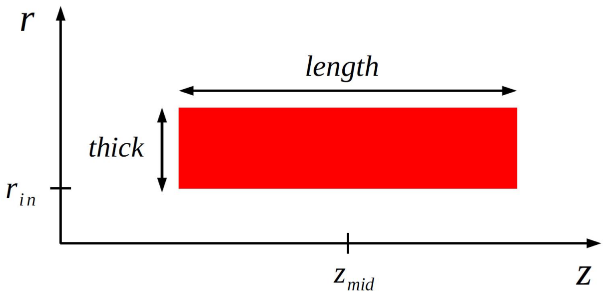

Figure 3.3: Definition of coil (red) input parameters for the *magfield2* program.

As long as the convergence ratio ρ/ρ_{cen} stays below a set limit of 0.99, the magnetic field will be calculated by Legendre polynomial expansion. If magfield2 is used for the first time with this coil configuration, the source points z_0 and the corresponding source coefficients B_n have to be calculated. These values are stored into the data file. They are needed to calculate the magnetic field components B_z and B_r (in [T]) and the vector potential A (in [Tm]) in a field point (z, r) in cylindrical coordinates. The programme searches for the best source point in the data file by calculating the distance ρ between the field point (z, r) and the source point and looking for the minimum ρ/ρ_{cen} ratio. If this ratio is larger than 0.99, the series is not convergent. In this case the magnetic field has to be computed by the elliptic integral method.

3.1.4 magfield3.c

Using the *magfield3* programme package [62] allows for magnetic field calculations for a coil system with different (local) symmetry axes. The geometry of a coil is described by

---

[2] Conventionally, this is the z-axis which is along the beam line.

[3] The total current is defined by the number of windings times the current in the coil wire.

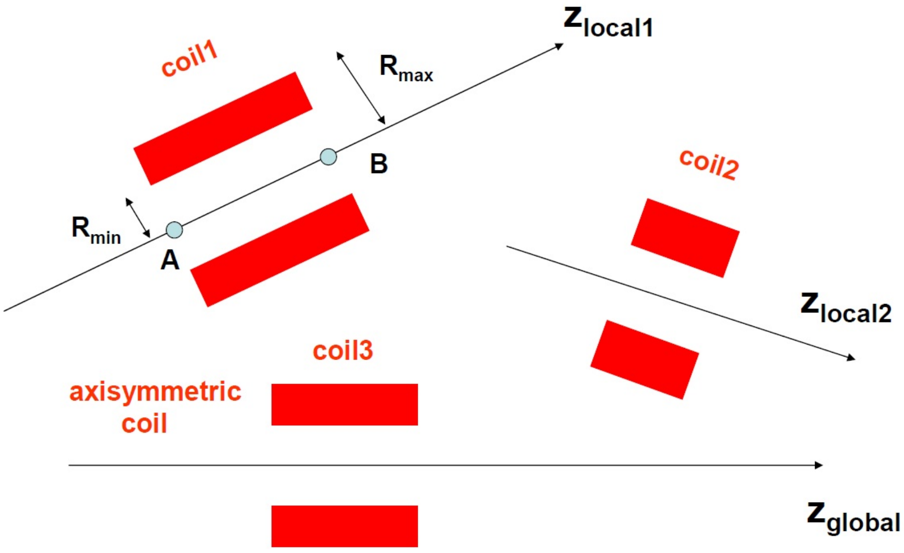

Figure 3.4: Coils with various local symmetry axes as used for the *magfield3* programme. The magnetic field of a coil is being calculated in the local coordinate system, using *magfield2* routines, and afterwards transformed into the global coordinate system.

two additonal points A and B which define this local symmetry axis. This is visualised in figure 3.4.

In addition to the central Legendre polynomial expansion used in the *magfield2* programme, the remote Legendre polynomial series is used here. Otherwise, the elliptic integral method would have to be used more often, leading to a much larger computation time needed.

The input files have to include information on the local symmetry axis as well as the coil geometry and current properties:

$$\begin{array}{lllll}
\mathrm{N}_{coil} & & & & \\
\mathrm{CD}[1] & \mathrm{A}[1][x] & \mathrm{A}[1][y] & \mathrm{A}[1][z] & \mathrm{B}[1][x] \\
\mathrm{B}[1][y] & \mathrm{B}[1][z] & \mathrm{R}_{min}[1] & \mathrm{R}_{max}[1] & \mathrm{n}[1] \\
\vdots & & & & \\
\mathrm{CD}[\mathrm{N}_{coil}] & \mathrm{A}[\mathrm{N}_{coil}][x] & \mathrm{A}[\mathrm{N}_{coil}][y] & \mathrm{A}[\mathrm{N}_{coil}][z] & \mathrm{B}[\mathrm{N}_{coil}][x] \\
\mathrm{B}[\mathrm{N}_{coil}][y] & \mathrm{B}[\mathrm{N}_{coil}][z] & \mathrm{R}_{min}[\mathrm{N}_{coil}] & \mathrm{R}_{max}[\mathrm{N}_{coil}] & \mathrm{n}[\mathrm{N}_{coil}]
\end{array}$$

The first parameter denotes the current density (in [A/m^2]), i.e. the total current divided by the coil cross section, the last parameter is required for the numerical integration in radial direction in casethat the elliptic integral method has to be used.

In order to compute the magnetic field of a coil, the local coordinate system of this particular coil is being used. In this local system the coil is axially symmetric and the field can be computed with central or remote Legendre polynomial expansion or elliptic integrals in the same way as within the *magfield2* programme. Afterwards, the resulting field values have to be transformed back into the global coordinate system.

3.2 Electric Field Calculations

The commercial programmes available for electric field calculations turned out to be not appropriate for the wire electrode system computation of KATRIN. Some tests with SIMION can be found in reference [63]. Therefore, calculation programmes based on the boundary element method (BEM) have been developed by F. Glück [64] especially for the KATRIN setup and its symmetries.

The electrode system consists of a full electrode, the main spectrometer vessel itself, and two layers of wire electrodes which are approximated by line segments. It is a major advantage that the electrode configuration of the KATRIN setup has carefully been arranged to a discrete rotational symmetry. It is thus sufficient to define a linear segment in the $z-r$ plane. The full and wire electrodes are then obtained by rotational transformations azimuthally along the z-axis. Furthermore, the system can be mirrored at the analysing plane. If one half of the spectrometer electrode system is defined, the other half can be calculated by mirror transformation.

To calculate the electric field produced by the electrodes they have to be discretised into subelements:

$$S = \sum_{j=1}^{N} S_j, \tag{3.9}$$

where $N = N_{full} + N_{wire}$ is the total number of subelements. The electrode surface S with a total charge density σ is divided into j subelements S_j with the corresponding charge densities σ_j, which are approximately constant within one subelement. The size of these subelements depends on the variation of the potential in the corresponding region. The results are more accurate for smaller subelements, but, in turn, the calculation time increases.

After this discretisation of the electrode surface, the charge densities are being calculated. This is the major difference to the magnetic field calculation. The potential U_i of a subelement i is a known quantity:

$$U_i = \sum_{j=1}^{N} C_{ij}\sigma_j. \tag{3.10}$$

The charge densities are then obtained by solving this linear algebraic equation system by the Gauss method. But beforehand, the Coulomb integral numbers C_{ij} have to be calculated. C_{ij} is the potential in the middle of the electrode element i due to the subelement j with unit charge density. It can be calculated by the following integration:

$$C_j(\vec{r}_i) = \frac{1}{4\pi\epsilon_0} \int\limits_{S_j} \frac{1}{|\vec{r}_i - \vec{r}_S|} \mathrm{d}^2\vec{r}_S. \tag{3.11}$$

The charge densities, the geometry and potential parameters of the independent subelements are then stored in a data file.

Analogously to the magnetic field calculation, the electric potential can be calculated by either elliptic integrals or by Legendre polynomial expansion. Again, the Legendre polynomial expansion method is faster but it is also constrained to regions where the series is convergent.

For the elliptic integral method, the electric potential in a field point (z, r), due to the full electrodes, is a superposition of the potentials from thin charged rings, obtained by discretisation:

$$\Phi(z,r) = \sum_{j=1}^{N_{full}} \frac{Q_j}{2\pi^2\epsilon_0} \frac{K(k_j)}{S_j}, \tag{3.12}$$

where

$$S_j = \sqrt{(r+R_j)^2 + (z-Z_j)^2}, \quad k_j = 2\frac{\sqrt{R_j r}}{S_j}.$$

The rings have the axial coordinate Z_j, the radius R_j and the total charge Q_j. $K(k_j)$ denotes the first complete elliptic integral calculated in the Chebyshev approximation [65].

In order to compute the electric potential due to a wire segment, the potential formula of a line segment with endpoints P_a and P_b can be used:

$$\Phi = \frac{\lambda}{4\pi\epsilon_0} \ln\left(\frac{D_a + D_b + L}{D_a + D_b - L}\right), \tag{3.13}$$

where L is the length of the line segment, D_a and D_b are the distances of its endpoints from the field point (z, r) and $\lambda = Q/L$ is the linear charge density of the segment with total charge Q. The total potential at the field point (z, r) is again a superposition of all wire segments.

The following equations for the potential and the electric field components apply for the central Legendre polynomial expansion

$$\begin{aligned}
\Phi(z,r) &= \sum_{n=0}^{\infty} \phi_n^{cen}(z_0) \left(\frac{\rho}{\rho_{cen}}\right)^n P_n(u), \\
E_z(z,r) &= -\frac{1}{\rho_{cen}} \sum_{n=0}^{\infty} \phi_{n+1}^{cen}(z_0)(n+1) \left(\frac{\rho}{\rho_{cen}}\right)^n P_n(u), \\
E_r(z,r) &= \frac{s}{\rho_{cen}} \sum_{n=0}^{\infty} \phi_{n+1}^{cen}(z_0) \left(\frac{\rho}{\rho_{cen}}\right)^n P_n'(u).
\end{aligned} \tag{3.14}$$

The parameter s is defined as $s = r/\rho = \sin\theta$ analogous to the magnetic field calculation. Accordingly, ϕ_n^{cen} are the source coefficients, $P_n(u)$ are the Legendre polynomials and ρ is the distance from the field point (z, r) to the source point z_0.

The same advantages and disadvantages as for the magnetic field calculation by Legendre polynomial expansion also apply for the electric field calculation.

For more detailed information, see [66], [67] and [68].

3.3 Tracking

Particle tracking, combined with a Monte Carlo generation of these particles, is a powerful tool to investigate the properties not just of a MAC-E filter, but of the whole experimental setup of KATRIN. The tracking programme *singletraj* was used for an investigation of electron transport in the source and transport section as well as in the spectrometer section, on which the present work is focused on. There are two tracking methods available the user has to choose from, the *exact calculation method* and the *adiabatic approximation method*. These will be introduced in the following. Furthermore, the possibility for electron-hydrogen scattering has been implemented in the tracking programme and will be discussed below.

3.3.1 Monte Carlo Particle Generation

To test especially the trapping properties of certain magnetic field configurations, a huge number of electrons with different starting conditions has to be tracked. Therefore, a Monte Carlo particle generator has been developed. The user can chose between different options:

- Particles starting inside the spectrometer volume: This is useful to test the behaviour of secondary electrons or ions which may be produced somewhere inside the volume.
- Particles starting at the position of maximum magnetic field on the source side of the spectrometer: This option is needed to test the transmission properties within simulations. By varying the radial starting position, the whole flux tube can be scanned. The position of maximum magnetic field correlates with the position of vanishing electric potential. Therefore, the total energy of the particle can be easily fixed. Furthermore, the maximum polar angle θ_{max} is reached at this position. Particles, starting with a polar angle smaller than θ_{max}, can not be trapped without any further interactions.
- Particles starting at the surface of the inner electrodes: Because the KATRIN experimental site is not underground, a large number of muons hit the main spectrometer vessel and inner electrodes. Electrons can be produced due to these impacts. For a perfectly axially symmetric electric and magnetic field, these electrons are shielded completely from the detector. But in reality the existence of magnetic stray fields will slightly distort the flux tube. The resulting effects have to be investigated with particle tracking simulations and test measurements.

Within a parameter file, the user has to set upper and lower limits for the starting parameters of the particle, i.e. kinetic energy E_{kin}, polar angle θ and azimuthal angle ϕ. The programme then generates particles which are isotropically emitted with equally distributed starting energies between $E_{kin,min}$ and $E_{kin,max}$. For particles starting at the position of maximum magnetic field, it has to be decided on whether they should be equally distributed over the whole flux tube or if they should start at a fixed radial position.

3.3.2 Exact Calculation Method

The motion of a charged particle in electric and magnetic fields can be calculated with the help of the Lorentz force

$$\vec{F}_L = q(\vec{E} + \vec{v} \times \vec{B}). \tag{3.15}$$

The method to solve differential equations is based on a Runge-Kutta algorithm [69], [63] of 8^{th} order[4]. This algorithm, though, can only solve first order differential equations. Therefore, the system has to be described by the six first order differential equations

$$\begin{aligned} \dot{\vec{x}} &= \vec{v}, \\ \dot{\vec{p}} &= \vec{F}_L. \end{aligned} \tag{3.16}$$

The velocity vector $\vec{v}$ and the momentum vector $\vec{p}$ are connected by the relativistic relation

$$\vec{p} = \frac{m_0 \vec{v}}{\sqrt{1 - \vec{v}^2/c^2}}. \tag{3.17}$$

At the start of a trajectory calculation the input starting parameters of the particle are used to calculate its velocity. For a single track the user can put these values into a parameter file by hand. For Monte Carlo simulations though, a huge number of particles has to be tracked and the starting parameters are being produced automatically by the Monte Carlo generator described in the previous section. The particle motion then happens stepwise with the stepsize h. The main advantage of this programme package is the possibility to vary this stepsize. This is needed due to the huge variation of magnetic field strength throughout the whole experimental setup. The cyclotron period T

$$T = \frac{2\pi}{\omega} = 2\pi \cdot \frac{\gamma m_0}{qB} \tag{3.18}$$

for a particle of mass m_0 and charge q in a magnetic field of strength B can be calculated, with γ denoting the relativistic factor. The user has to choose the number *ntimestep* which defines the stepsize

$$h = \frac{T}{ntimestep}. \tag{3.19}$$

The magnetic field gradient typically is large in regions close to high magnetic fields, where the cyclotron period is small. Therefore, the stepsize there is smaller than in low magnetic field regions with larger cyclotron periods. For each timestep, the initial conditions (position and momentum) are being used to calculate the final conditions by the Runge-Kutta algorithm. Each step requires 16 function evaluations, which in turn, require the calculation of the electric and magnetic fields. This is the most time-consuming part of a calculation. For a small step size, both, the accuracy and the calculation time increases. Therefore, a compromise between these two objectives had to be found. The accuracy of each step is controlled by the conservation of its total energy. If the particle does not interact with other particles and if synchrotron radiation

---

[4] Actually, the user can choose between 4^{th} and 8^{th} order but the calculation with the 8^{th} order is faster while maintaining the same accuracy.

is being neglected, the total energy of the particle should be conserved. Otherwise, the energy losses have to be calculated and the value for the total energy has to be adjusted. The programme running is stopped as soon as any of the exit conditions, defined by the user, is fulfilled. The programme has the following options implemented:

- Particle has reached the z-limit: The user has to define a region of interest by putting a minimum and maximum value for the z coordinate into the input file.
- Particle has encountered an electrode: The programme stops if a particle reaches the inner electrodes, which are treated as full electrodes to avoid particles stepping through them. This is needed because the calculation time increases drastically close to the electrodes. A method has to be implemented to calculate particle motion through the electrodes more efficiently.
- Particle is trapped: If a particle changes its direction of movement on the z-axis twice, it is considered as trapped. It can only leave the trap again after interaction with other particles. The user has to decide if this exit conditon is turned on, which reduces the calculation time, or off. This depends on the purpose of the simulation.
- Maximum total pathlength reached: To be able to limit the calculation for trapped particles, the user can put an upper limit on the maximum total pathlength of the particle.
- Maximum calculation time reached: This is the easiest option to control the calculation time, but might not be appropriate for all kinds of simulations.
- Maximum number of Runge-Kutta steps reached: Because the Runge-Kutta algorithm is responsible for the majority of the calculation time, it can be controlled with this option. Nevertheless, this option should mainly be used for testing purposes. It helps to check if the step size regulation is working correctly. It should be put to a value of the order of 10^7 for a specific simulation.

3.3.3 Adiabatic Approximation Method

The adiabatic motion of a charged particle in a magnetic field can be decoupled into two seperate terms. The longitudinal velocity component $v_{||}$ leads to a movement along a magnetic field line as shown in figure 3.5. Due to the transversal component $v_{\perp}$, which leads to a Lorentz force $\vec{F} = q\vec{v}_{\perp} \times \vec{B}$, the particle undergoes a cyclotron motion around the so-called *guiding centre* $\vec{R}$.

Only the longitudinal movement of the guiding centre is calculated with the Runge-Kutta method, which is also used for the exact calculation. This can reduce the number of steps, which have to be calculated, by more than 90%[5]. The cyclotron radius ρ is defined by the magnetic field strength at the position of the particle. Therefore, the

---

[5] This value depends on the parameters (ntimestep, maximum pathlength per step) which have to be defined by the user in the input file.

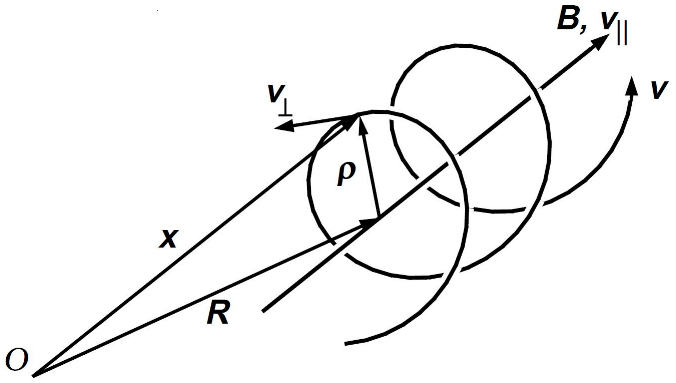

Figure 3.5: Sketch of a negatively charged particle on its cyclotron motion around a magnetic field line. The particle motion can be described as the sum of a fast cyclotron motion around the guiding centre $\vec{R}$ and a slow drift velocity, which is not shown in this sketch.

cyclotron motion can be calculated separately and then added to the guiding centre motion. Furthermore, the magnetron drift, combined of equations (4.2) and (4.3), is also applied. Tests have revealed that the adiabatic approximation method is faster by about a factor of 10, while the resulting trajectories of both methods agree with each other up to a few millimeters, which is sufficient when considering the large dimensions of the main spectrometer.

3.3.4 Scattering

Even with the ultra high vacuum of less than 10^{-11} mbar, which will be achieved by the KATRIN main spectrometer UHV system, the number of scattering events of electrons on the residual gas, which mainly consists of hydrogen, can not be neglected. Especially during calibration and monitoring mesurements a large number of electrons will be sent through the spectrometer by an electron gun. Therefore, the possibility for electron-hydrogen scattering has been implemented into the tracking programme. The corresponding routines were written by F. Glück and tested within the the diploma thesis of K. Essig [70]. The user can choose to turn scattering on or off within the tracking input file.

The scattering probability P is a function of the cross section σ of electron-hydrogen scattering, the stepsize s and the number density of the hydrogen molecules n:

$$P = \sigma \cdot s \cdot n. \tag{3.20}$$

The total cross section $\sigma = \sigma_{el} + \sigma_{exc} + \sigma_{ion}$ is composed of the elastic cross sections σ_{el}, the excitation cross section σ_{exc} and the ionisation cross sections σ_{ion}. The reference values to compute the elastic cross sections were taken from [71] and [72]. For excitation events, in addition to the excited electronic states [73], B and C vibrational states [74] of the hydrogen molecules have to be distinguished. For ionisation events with an energy loss of the impact electron of less than 250 eV, the cross sections were taken from [75].

For events with more than 250 eV energy loss, [76] was taken as reference.
According to the ideal gas law of thermodynamics

$$pV = NkT \tag{3.21}$$

the number of hydrogen molecules per volume unit can be calculated via[6]

$$n = \frac{N}{V} = \frac{p}{kT} = \frac{10^{-9}\ \mathrm{Pa}}{1.38 \cdot 10^{-23}\ \mathrm{J/K} \cdot 300\ \mathrm{K}} = 2.42 \cdot 10^{9} \frac{\mathrm{molecules}}{\mathrm{m}^3}. \tag{3.22}$$

The user has to set an upper limit for the stepsize s and the programme will decrease it further if the energy conservation within a step is not sufficient, i.e. not in the range of $10^{-8} - 10^{-10}$.
For each electron step, a random number generator [77] produces a floating-point number in the range from zero to one, excluding one, but including exact zero. The subsequences have a period of $2^{144} \approx 2 \cdot 10^{43}$ and an average length of approximately 10^{30}. If this generated number u is larger than the scattering probability P, the electron does not undergo a scattering event. If it is smaller, it has to be further distinguished between elastic scattering, excitation and ionisation events with their corresponding scattering probabilities P_i, defined as

$$P_{el/exc/ion} = \frac{\sigma_{el/exc/ion}}{\sigma}. \tag{3.23}$$

Subroutines generate the energy loss and the polar scattering angle of the primary electron, which depend on its incident kinetic energy. Furthermore, secondary electrons are being created. Their position and energy can be stored to a data file so that they can be tracked afterwards.
This simulation of electron-hydrogen scattering in the main spectrometer will be of importance in chapter 6, where the simulation of a periodic measurement to monitor the column density ρd of the tritium source WGTS will be presented.

---

[6] The main spectrometer will be operated at a pressure of 10^{-11} mbar = 10^{-9} Pa = 10^{-9} J/m^3.

4. Optimisation of the Magnetic Configuration

A high ν-mass sensitivity in a tritium-β-decay experiment like KATRIN requires a spectrometer with optimum transmission and background properties. Besides the electric potential, the magnetic field plays a decisive role in achieveing this objective. The magnetic guiding field has to meet stringent design requirements which will be summarised in the first section of this chapter. Within the framework of calculations, performed in this work and using the tools described in chapter 3, different configurations were tested for their properties. The magnetic field has to be optimised in such a way, that the transmission condition is fulfilled while keeping the background rate at a minimum. The two possibilities to achieve this will be discussed in section 4.2. Section 4.3 is concerned with background properties of a MAC-E filter for the different magnetic field configurations. Within the last section 4.4, these two main configurations will be compared.

4.1 Magnetic Design Requirements

To optimise both, background and transmission properties of the main spectrometer the magnetic field has to meet certain design requirements ([50], [78]). For any simulation concerning the electromagnetic design, the following properties have to be checked carefully and the optimum solution has to be found.

Flux tube size

There is the possibility for secondary and field emission of electrons at the surface of the inner wire electrodes. Defining a minimum distance of 0.3 m between the surface of the flux tube and these electrodes will lead to a sufficiently good screening of these electrons. The fixed magnetic field strength of 3.6 T in the source leads to a minimum magnetic field of about 3 G in the analysing plane in order to assure this safety margin.

Transmission condition

Only those electrons which fulfil the transmission condition will reach the main detector. This can be illustrated with an electron starting in the source with a fixed starting angle. It needs a certain minimum starting energy, the transmission energy E_{trans}, in order to be able to pass the electrostatic barrier. This energy is defined as the minimum starting energy E_0 which is needed, so that its longitudinal energy $E_{||}$ reaches zero in the analysing plane.

The transmission condition is satisfied if

- an electron with $E_0 < E_{trans}$ is reflected.
- an electron with $E_0 > E_{trans}$ is transmitted.
- for an electron with $E_0 = E_{trans}$, along all field lines, $E_{||} = 0$ in the analysing plane and $E_{||} > 0$ everywhere else.

This assures that the transmission function in figure 2.2 is determined only by the maximum magnetic field at the pinch magnet and the minimum magnetic field in the analysing plane. The energy transformation $E_\perp \rightarrow E_{||}$ is based on an interplay of the magnetic field and the electric potential. Since the electric potential setup is fixed, the magnetic field has to be adjusted in order to fulfil the transmission condition. This will be discussed in detail in section 4.2.

Homogeneity

In the analysing plane the magnetic field should be as homogeneous as possible. Once the transmission condition is satisfied, only the transmission energy, which is defined by the magnetic field and electric potential in the source and analysing plane, is needed for the analysis of the measured spectrum. The flux tube is imaged directly onto the detector. Due to its segmentation, the corresponding regions of the analysing plane can be treated seperately in the final analysis. To each pixel a particular magnetic field strength and electric potential will be assigned. Therefore, each pixel has its own transmission function. The influence of an inhomogeneous magnetic field on the transmission function is sketched in figure 4.1.

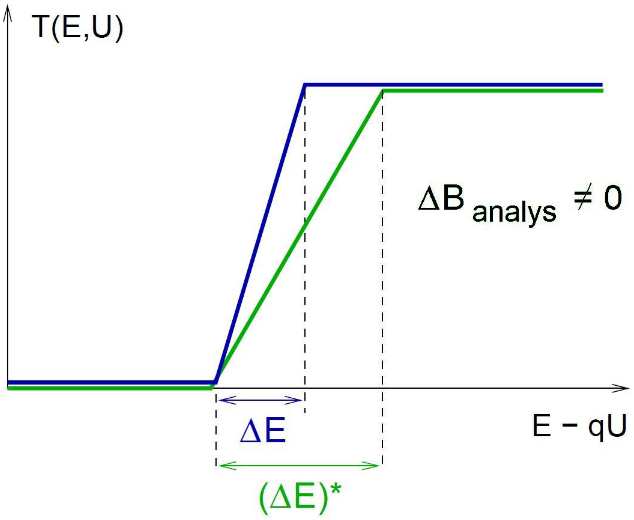

Figure 4.1: Impact of magnetic field inhomogeneity on the transmission function. A magnetic field inhomogeneity $\Delta B_{analys} = B_A(r) - B_A(r^*)$ leads to a radial dependence of the width of the transmission function which determines the energy resolution ΔE.

In the analysing plane, a maximum inhomogeneity of the magnetic field ΔB_{analys} of 10% is acceptable, comparing a magnetic field line on the axis with a field line at the outside of the flux tube. With a radial segmentation into 12 rings, this results in an inhomogeneity of less than 1% for each pixel. Due to an inhomogeneity ΔB of the magnetic field within a pixel, the energy resolution gets modified according to

$$\frac{B_{analys} \pm \Delta B}{B_{A,max}} = \frac{(\Delta E)^*}{E}. \tag{4.1}$$

For a maximum field in the analysing plane of $B_{A,max} = 3$ G and an inhomogeneity of 1% per pixel, the energy resolution $\Delta E = 0.93$ eV changes by $\delta(\Delta E) = 9.3$ meV. To make a rough estimate on the resulting systematic error, the relation $\Delta m_\nu^2 = -2\sigma^2$, taken from [3], can be used[1]. Due to a deviation of the energy resolution of ±9.3 meV an acceptable systematic error of $|\Delta m_\nu^2| \approx |-2 \cdot (9.3)^2|$ meV$^2 = 1.7 \cdot 10^{-4}$ eV^2 is expected. However, it should be noted that the inhomogeneity of the electrostatic potential has a much stronger impact on ΔE.

Axial Symmetry

One primary task of the magnetic field is to screen electrons, emitted from the surface of the inner electrodes, from the sensitive spectrometer volume and hence from the main detector. This can only be guaranteed with a perfectly axially symmetric magnetic field. Deviations from axial symmetry allow electrons to penetrate into the flux tube [79]. An azimuthal dependence of the magnetic field value would lead to a radial gradient drift with a drift velocity

$$\vec{v}_G = -\frac{cE_\perp}{eB^3}\vec{B} \times \nabla_\perp \vec{B} \tag{4.2}$$

and the existence of an azimuthal field component would lead to a radial $\vec{E} \times \vec{B}$ drift with a drift velocity

$$\vec{v}_E = \frac{c}{B^2}\vec{E} \times \vec{B}. \tag{4.3}$$

In a perfectly axially symmetric field these drift velocities have azimuthal components only. But if stray fields distort the magnetic field, the velocities (4.2) and (4.3) lead to a magnetron drift of electrons in radial direction, i.e. into the flux tube, possibly leading to an increased background.

Adiabaticity

If an electron does not move adiabatically, its transversal energy does not transform according to

$$E_{\perp f} = E_{\perp i} \cdot \frac{B_f}{B_i}, \tag{4.4}$$

where $E_{\perp i}$ and B_i ($E_{\perp f}$ and B_f) denote the transversal energy and magnetic field at the initial (final) position of the electron. As a result, the magnetic moment μ (2.2) is not constant anymore. Accordingly, the electron does not 'gain' the full increase

---

[1] This relation is only correct for a gaussian distributed deviation which is not completely the case (it is more of rectangular shape), but it can nevertheless help to make a rough estimate on the systematic error.

in longitudinal energy which is expected from the energy conversion $E_\perp \rightarrow E_{||}$. This leads to an uncontrolled broadening of the transmission function in figure 2.2. Close to the analysing plane, where the magnetic field is rather low, any non-adiabatic motion is particularly disadvantageous. A small fraction of missing longitudinal energy can decide on the transmission or reflection of an electron. This has an immediate impact on the count rate at the detector. Ideally, the parameter

$$\Delta E_\perp = E_{\perp f} - E_{\perp i} \cdot \frac{B_f}{B_i} \tag{4.5}$$

is zero throughout the whole trajectory of an electron.

4.2 Transmission Properties

In order to be able to calculate the transmission function T analytically according to (2.6), it has to be guaranteed that the transmission condition is fulfilled for all electrons moving inside the flux tube. The relativistic longitudinal kinetic energy $E_{||}$ for an electron moving along a specific trajectory can be calculated by

$$E_{||} = E_0 - E_0 \cdot \sin^2\theta_0 \cdot \frac{B \cdot (\gamma_0 + 1)}{B_0 \cdot (\gamma + 1)} - q(U - U_0), \tag{4.6}$$

where E denotes the total kinetic energy of the electron, B the magnetic field and U the electric potential at its position. Furthermore, the Lorentz factor γ is needed. The index 0 indicates the values at the starting point. Combining this with the transmission condition provides an expression for the transmission energy:

$$E_{trans} = q(U_A - U_0) \cdot \left(1 - \sin^2\theta_0 \cdot \frac{B_A \cdot (\gamma_0 + 1)}{B_0 \cdot (\gamma_A + 1)}\right)^{-1}. \tag{4.7}$$

The index A indicates the values at the analysing plane. The electromagnetic design is correct if the longitudinal energy of all electrons, starting with the transmission energy E_{trans}, is positive everywhere and has its minimum value $E_{||} \geq 0$ in the analysing plane. Whenever $E_{||}$ drops below zero, the electron gets reflected. This is not acceptable and, hence, the electromagnetic design has to be corrected.

The inner electrode of the cylindrical spectrometer part, which is about 10 m long, is operated at a very stable voltage of about −18.6 kV. Therefore, the electric potential is rather homogeneous along the beam axis. This configuration of the electric potential is preferrable since it improves the homogeneity in radial direction which is connected to the homogeneity along the beam axis. However, with this configuration it is not guaranteed to satisfy the transmission condition. Any deviations of the electric potential towards more negative values could lead to a violation of the transmission condition. In this case the magnetic field has to be adjusted with the help of the LFCS.

4.2.1 Global Magnetic Field Minimum Solution

The KATRIN experiment was initially designed to be operated with a magnetic field configuration which has its global minimum in the analysing plane, as sketched in figure 4.2. Therefore, the energy transformation $E_\perp \to E_{||}$ of an electron is only completed in the analysing plane. At the same time the electric potential is very homogeneous in the cylindrical part of the spectrometer. An electron, entering the main spectrometer, at first perceives a rapidly decreasing[2] electric potential. This implies that the magnetic field has to transform its transversal energy into longitudinal energy accordingly. Otherwise, the longitudinal energy could drop below zero, which would result in a too early reflection of the electron. This calls for a rapidly decreasing magnetic field. On the other hand, it should not drop too fast to still ensure the adiabaticity. But even if there are small deviations from the adiabatic invariant $\gamma\mu$, they will get scaled down when moving towards the analysing plane [63]: $\Delta E \to \Delta E \cdot B_A/B_0$. Here, ΔE denotes the energy deviation from due to non-adiabatic movement, B_A is the magnetic field at the analysing plane and B_0 the magnetic field at the current position of the electron.
Close to the analysing plane, where the electric potential is very homogeneous, a decreasing magnetic field is disadvantageous for the transmission condition. The longitudinal energy of an electron gets increased further while the electric potential keeps constant. Therefore, $E_{||}$ could have its global minimum somewhere else but in the analysing plane. The analysis of the measured spectrum would require the knowledge of the magnetic field strength at the position of this global minimum of the longitudinal energy.
Hence, in a configuration with a very homogeneous electric potential, the magnetic field also has to be very homogeneous along the beam axis.

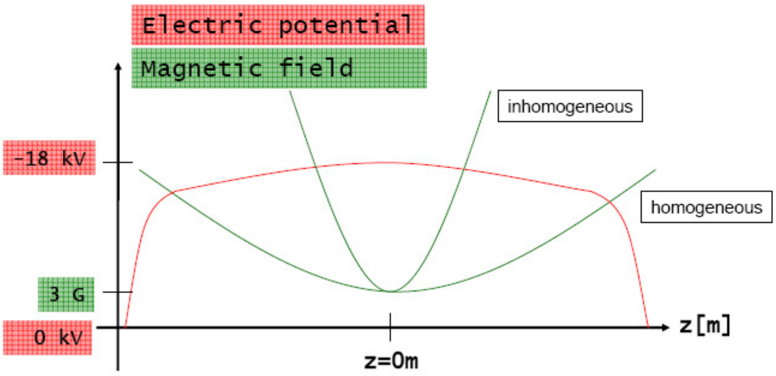

Figure 4.2: Global magnetic field minimum solution. This sketch shows the electric potential (red) and magnetic field (green) in the main spectrometer. The electric potential is almost constant along the beam axis. In this case the magnetic field has to be very homogeneous in order to satisfy the transmission condition.

---

[2] The absolute value of the electric potential increases but has a negative sign.

4.2.2 Local Magnetic Field Minima Solution

Another possibility to avoid a violation of the transmission condition is to choose a magnetic field configuration with two local minima and a local maximum in the analysing plane. This is sketched in figure 4.3. While the magnetic field in the analysing plane has the same strength in both configurations, it drops to an even lower value in front of and behind the analysing plane in the *local magnetic field minima solution*. Therefore, the transformation $E_\perp \rightarrow E_{||}$ is even more effective in this region. The longitudinal energy of an electron, starting with the transmission energy, can not drop to zero anywhere else but in the analysing plane. Furthermore, the magnetic field increases close to the analysing plane[3], leading to a decrease in longitudinal energy of the electron. This guarantees that the longitudinal energy reaches its global minimum only in the analysing plane.

Since the preferred homogeneous configuration of the electric potential of KATRIN is not a configuration which automatically satisfies the transmission condition, the *local magnetic field minima solution* could be preferrable because in this case the magnetic field takes over this responsibility. However, local magnetic field minima might lead to particle traps, which can in turn lead to an increase in background. Electrons could be stored there due to the magnetic mirror effect discussed in the next section 4.3.

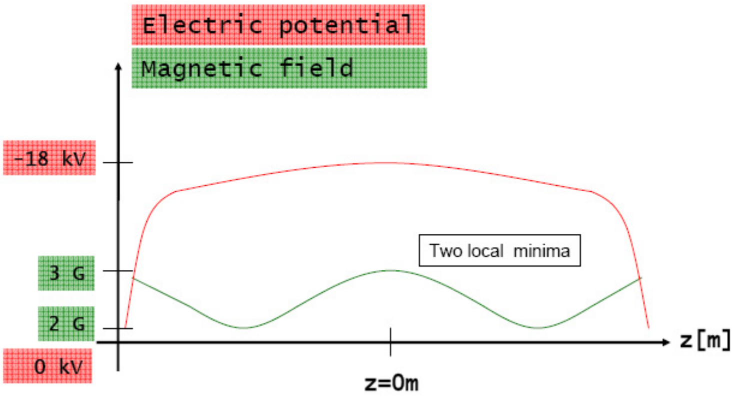

Figure 4.3: Local magnetic field minima solution. This sketch shows the electric potential (red) and magnetic field (green) in the main spectrometer. The electric potential is almost constant along the beam axis. A magnetic field configuration with two local magnetic field minima ensures the transmission condition.

---

[3] Actually the magnetic field increases in front and decreases behind the analysing plane.

4.3 Background Properties

In this section, three possible traps within a MAC-E filter will be discussed. The 'intrinsic magnetic mirror' trap and the 'hybrid' trap can not be avoided in any spectrometer of MAC-E type. The 'local magnetic mirror' trap, however, only occurs for a magnetic field configuration with local minima.

4.3.1 Intrinsic Magnetic Mirror Trap

It is an intrinsic property of a MAC-E filter to create a trap for electrons inside the whole main spectrometer due to the magnetic mirror effect. Electrons starting in the volume of the spectrometer are accelerated towards its ends. On their way they perceive a growing magnetic field which increases their transversal energy. If all longitudinal energy is transformed into transversal energy before the electron reaches the point of maximum magnetic field inside a solenoid, they are stored. The question is, how many electrons are stored depending on their starting energy.

An electron starting at the analysing plane, where the magnetic field has its minimum, gains kinetic energy while being accelerated towards one end of the spectrometer. Its kinetic energy at the position of maximum magnetic field, i.e. zero electric potential, is $E_{start} + qU_{ret}$. E_{start} denotes the starting kinetic energy of the electron and U_{ret} the retarding potential of the spectrometer. The electron is stored if all its longitudinal energy is transformed into transversal energy. This is equivalent to a polar angle exceeding 90°. Therefore, a maximum transversal starting energy $E_{\perp,start}^{max}$ can be found with which an electron can be produced in the analysing plane in order not to be stored:

$$E_{\perp,start}^{max} = (E_{start} + qU_{ret}) \cdot \frac{B_A}{B_{max}}. \tag{4.8}$$

The maximum starting angle can be calculated analogous to (2.3) with the help of (2.4):

$$\theta_{max} = \arcsin\left(\sqrt{\frac{E_{\perp,start}^{max}}{E_{start}}}\right). \tag{4.9}$$

Assuming an isotropic production of electrons, the fraction of transmitted electrons is given by

$$T = 1 - \cos(\theta_{max}). \tag{4.10}$$

With this relation the trapping probability P for electrons starting in the analysing plane can be calculated. The result is shown in figure 4.4. The blue curve shows the trapping probability for electrons, starting in the analysing plane, depending on their starting kinetic energy. The maximum alowed starting angle is represented by the red curve. Electrons with a starting kinetic energy which is smaller than the energy resolution of the spectrometer can not get trapped independently of their starting polar angle. For higher energetic electrons, the trapping probability increases rapidly. For instance, only 3% of all electrons starting inside the spectrometer with a kinetic energy of 15 eV are transmitted. This is the threshold for ionisation events and therefore those stored electrons can, in principle, increase the background. However, it is reasonable to assume that there are not many electrons being produced with more than 15 eV kinetic

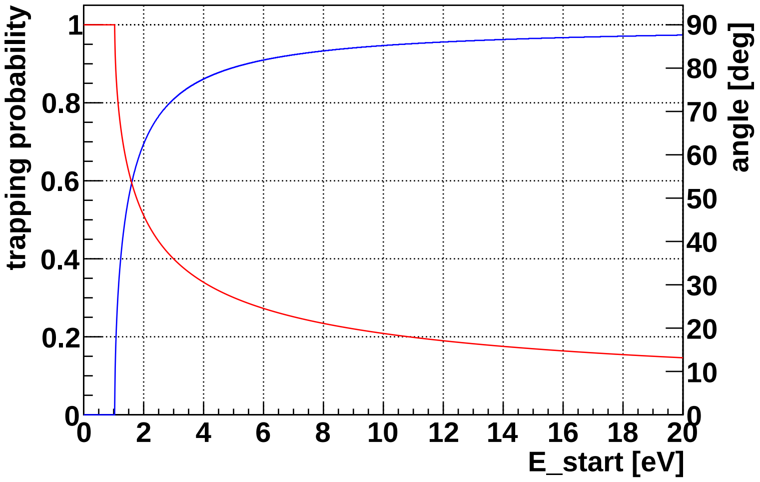

Figure 4.4: Trapping probability for electrons starting in the analysing plane. Simulation parameters: $B_{min} = 3.5$ G, $B_{max} = 6$ T, $U_{ret} = 18.6$ keV. Blue (left axis): Trapping probability. Red (right axis): Maximum starting angle for an electron to be transmitted. Electrons with a starting kinetic energy smaller than the energy resolution of the spectrometer can not get trapped.

energy. Ionising electrons would need a kinetic energy of at least 30 eV to create these secondary electrons. Due to the axial homogeneity of the electric potential, this can only be the case in a region further away from the analysing pane than ±8 m. Besides, in the Mainz experiment, 15 eV electrons were also stored with a probability of about 90%, but an increase in background was not observed [36]. On the other hand, due to the higher magnetic field in the analysing plane, the Mainz spectrometer did not suffer from such a large number of stored low energetic electrons as the main spectrometer. A comparison of trapping probabilities for different magnetic field strengths is shown in figure 4.5.

Nevertheless, trapped low-energy electrons could increase the probability of the production of higher energetic electrons via elastic scattering. To decrease the probability of trapping these low-energy electrons, the magnetic field in the analysing plane can be increased.

4.3.2 Local Magnetic Mirror Traps

In case of a magnetic field configuration with two local minima, electrons starting in the region of these minima can be stored due to magnetic mirroring. Because the depth of these minima is rather small, they need a certain minimal starting angle in order to be stored. The electric potential is approximately constant within the region of a local minimum. Therefore only the magnetic field is responsible for the trap. In this case the trapping condition is independent of the starting energy and can be calculated analogous to (2.3):

$$\theta_{min} = \arcsin\left(\sqrt{\frac{B_{min}}{B_A}}\right) \tag{4.11}$$

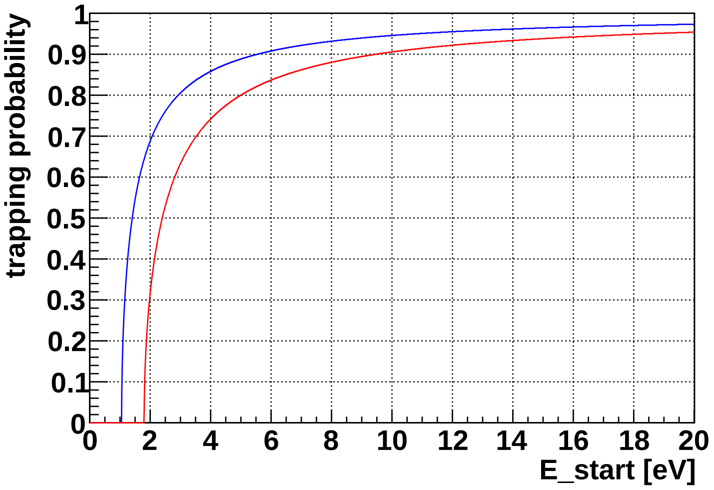

Figure 4.5: Trapping probability for different magnetic field strengths. ***Blue***: 3.5 G in the analysing plane. ***Red***: 6 G in the analysing plane. A higher magnetic field strength leads to a worse energy resolution of the spectrometer. In return, electrons are allowed to have higher starting kinetic energies without getting trapped by the magnetic mirror effect.

where B_{min} denotes the magnetic field strength in the local minimum.

4.3.3 Hybrid Traps

It is possible for electrons starting at the entrance or exit region of the main spectrometer to be trapped. In this case, we consider an electron starting near the ground electrode with an energy of less than the retarding potential. This electron will be reflected before it can pass the analysing plane. If the same electron has a sufficiently large starting angle, it will also be reflected by the magnetic field of the superconducting magnets due to the magnetic mirror effect. Therefore, this trap is a *hybrid trap*. The air coil system, however, is unable to influence such a trap as it occurs near the solenoids where the magnetic field, produced by the LFCS, is negligible.

4.4 Optimised Magnetic Field Configurations

Within the present project schedule, only a part of the entire KATRIN setup will be available for the main spectrometer test measurements and hence the magnet configuration is different than in the final setup. During the test measurement phase, the main spectrometer will prospectively be operated in a 'stand-alone' mode. All magnets of the source and transport section will be missing, and it is not yet defined which superconducting magnet configuration of the spectrometer section will be available. Both the EMCS and the LFCS will be active, leaving just the z-component of the earth's magnetic field to be taken into account. A configuration with just the two pre-spectrometer solenoids was chosen as an example for an initial test measurement setup. Due to the identical properties of these magnets, a magnetic field configuration which is very symmetric with regard to the analysing plane can be achieved. For the final setup, the two pre-spectrometer magnets, the pinch and the detector magnet, an approximation of the WGTS, DPS, CPS magnets and the z-component of the earth's magnetic field were taken into account. Tables 4.2 and 4.1 show the constant input parameters of the simulations. In the final setup, the direction of the LFCS current flow is chosen in a way that the resulting magnetic field vector points in opposite direction of the z-component of the earth's magnetic field. Therefore, a certain offset current is needed to compensate this field component. Because the same magnetic field strength has to be achieved during test measurements with less solenoids, the LFCS cables have to bear much higher currents. Hence, the z-component of the earth's magnetic field is used as an offset field to reduce this current. Therefore, the currents of the LFCS flow in opposite direction than in the final setup.

It is not yet decided on whether a *local magnetic field minima solution* or a *global magnetic field minimum solution* will be realised. Furthermore, theexact value of the magnetic field strength in the analysing plane is not yet fixed. Therefore, a possible set of ampere turns for different magnetic field strengths in the analysing plane were computed for the *local magnetic field minima solution* and the *global magnetic field minimum solution*. The results of these calculations can be found in appendix B.

4.4.1 Final Setup

The minimum magnetic field strength of $3-3.5$ G in the analysing plane is fixed by the diameter of the main spectrometer vessel, whereas the maximum value of 6 G is defined by the maximum field of the superconducting magnets of $4.5-6$ T, and the maximum allowed number of turns of the LFCS rings. The most probable value to be used is thus in the range from $3-4$ G. Therefore, the magnetic design for the case of 3.5 G in the centre of the analysing plane is presented in the following. With a magnetic field strength of $B_D = 3.5$ T at the detector side, this would allow mapping of the analysing plane with an aspect ratio of 100:1.

Table B.1 shows a possible set of ampere turn values of the LFCS which fulfils the magnetic design requirements. The *local magnetic field minima solution* and the *global magnetic field minimum solution* are compared.

The magnetic design requirements have to be fulfilled within the whole flux tube of 191 Tcm^2. The flux tube radius r_z at a certain z-position is defined by the maximum

Type	Position z [m]	Ampere turns [At]	Magnetic field in the analysing plane [G]
pre-spec magnet 1	-16.49	2120000	0.184
pre-spec magnet 2	-12.13	2120000	0.462
pinch magnet	12.22	3225000	0.592
detector magnet	13.82	4230000	0.791
WGTS	-38.5	53100000	0.099
DPS	-27.2	29000000	0.069
CPS	-20	25170000	0.412
earth's magnetic field	0	-3246	-0.2

Table 4.1: Constant magnetic field input parameters for the final setup. The z-position, the ampere turns value and the contribution to the magnetic field strength in the analysing plane are given for each magnet. The earth's magnetic field was approximated by a coil with 40 m diameter and 200 m length in axial direction. The analysing plane is located at $z = 0$.

Type	Position z [m]	Ampere turns [At]	Magnetic field in the analysing plane [G]
pre-spec magnet 1	12.13	-2120000	-0.462
pre-spec magnet 2	-12.13	-2120000	-0.462
earth's magnetic field	20	-3246	-0.2

Table 4.2: Constant magnetic field input parameters for the test measurements.

radius in the source r_S and the corresponding magnetic field strenghts $B_S(r_s)$ and $B_z(r_z)$:

$$r_z = r_S \cdot \sqrt{\frac{B_S}{B_z}}. \tag{4.12}$$

Figure 4.6 shows six representative, equally spaced field lines for the *global magnetic field minimum solution* and the *local magnetic field minima solution.* In both cases there is still a safety distance of at least 30 cm between the outer magnetic field line of the flux tube and the inner electrodes.

The magnetic field strength along these field lines is plotted in figure 4.7. The colours are used correspondingly to figure 4.6. These plots show the main differences between the two magnetic field configurations. The two minima are most distinctive for the outer field lines. This is advantageous concerning the transmission condition. The inner electrodes in the direct vicinity of these field lines create local minima of the electric potential shown in figure 4.8. These, in turn, directly cause local minima of the longitudinal energy of an electron moving along this field line, which is shown in figures 4.9 and 4.10. This feature is independent of the two different magnetic field configurations.
However, in the *global magnetic field minimum solution* the longitudinal energy drops

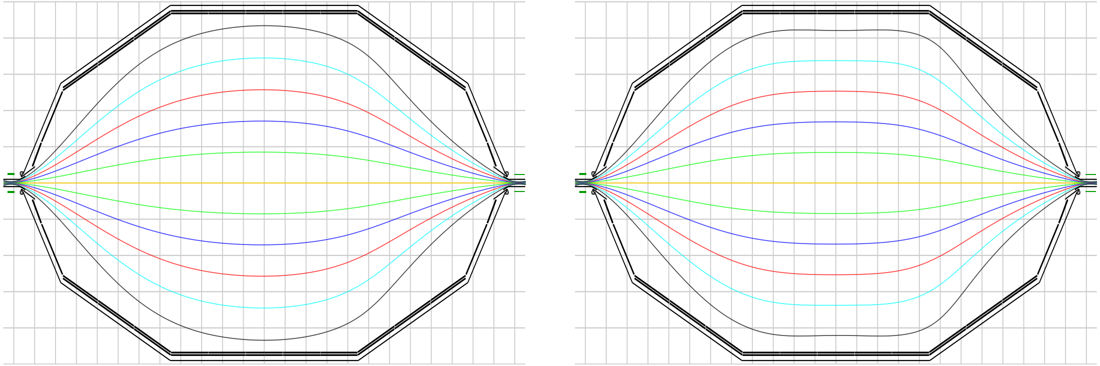

Figure 4.6: Magnetic field lines of the 191 Tcm^2 **flux tube.** Six equally spaced, representative field lines within the design flux tube of 191 Tcm^2 (black field line) are shown. ***Left***: *Global magnetic field minimum solution.* ***Right***: *Local magnetic field minima solution.* The grid has a scale of 1 m × 1 m.

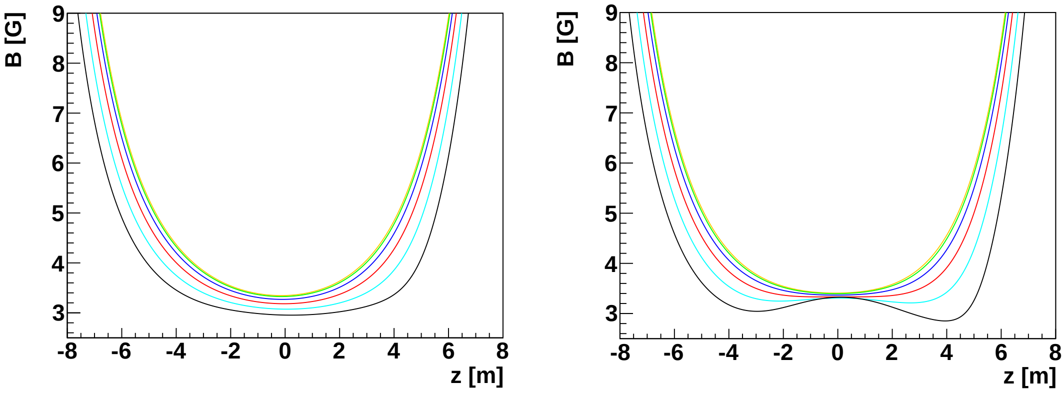

Figure 4.7: Magnetic field strength along field lines shown in figure 4.6. ***Left***: *Global magnetic field minimum solution.* The magnetic field is not symmetric with respect to the analysing plane. Its strength increases faster at the detector side (positive z-values). ***Right***: *Local magnetic field minima solution.* Two local minima occur only on the outer field lines (black and light blue) and are more distinctive towards the outside of the flux tube.

down to 33 meV, while in the *local magnetic field minima solution* it stays above 75 meV. Therefore, in the first case the electron is much more prone to violating the transmission condition than in the latter case. From a simulation point of view, the transmission condition is fulfilled in both cases since the longitudinal energy reaches zero only in the analysing plane. The simulation, however, is based on idealised input parameters. In reality these local minima of the electric potential could lead to a violation of the transmission condition. Therefore, further investigations and especially test measurements are needed to settle these issues.

The correlation between the minima of the electric potential and the longitudinal energy is obvious when comparing figures 4.9 and 4.10 with figure 4.8. Furthermore, these minima could possibly create penning traps for electrons and ions. The depth of such

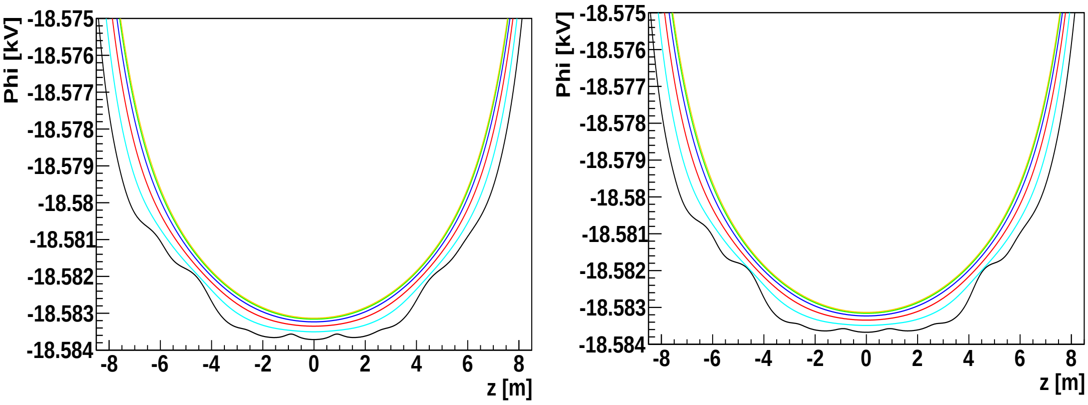

Figure 4.8: Electric potential along field lines shown in figure 4.6. ***Left***: *Global magnetic field minimum solution.* ***Right***: *Local magnetic field minima solution.* The electric potential shows local minima along the field line which is closest to the inner electrodes (black). These minima can serve as small penning traps or lead to a violation of the transmission condition.

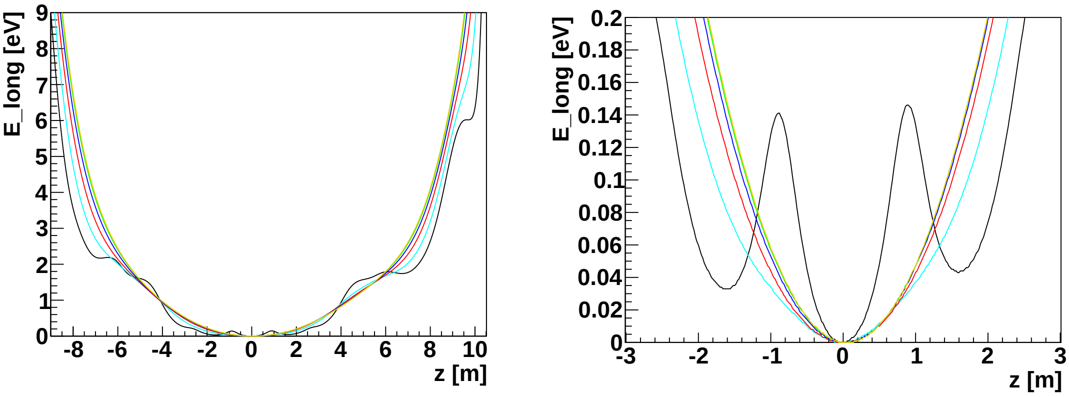

Figure 4.9: Longitudinal energy along field lines of the *global magnetic field minimum solution* shown in figure 4.6. ***Left***: Local minima occur on the outer magnetic field line (black) which is closest to the inner electrodes. ***Right***: A zoom into the interesting region around the analysing plane. The electrons started at the source with the maximum starting angle $\theta = 51^\circ$ and the corresponding transmission energy $E_{trans} \approx 18584$ eV. If the longitudinal energy drops below zero in front or behind the analysing plane, the electron will get reflected at these positions, leading to a violation of the transmission condition.

traps which are close to the electrodes is of the order of 1 eV. Electrons are trapped if their longitudinal energy in these regions is smaller than 1 eV. If their kinetic energy exceeds a threshold of 15.4 eV they could ionise the residual gas, which mainly consists of hydrogen molecules. The safety distance between the flux tube and the inner electrodes comes into effect here. If it is large enough, these trapped electrons and the resulting secondary electrons will not be guided to the sensitive part of the detector. Hence, they do not contribute to the background and do not influence the β-spectrum. On the other hand, trapped electrons with kinetic energies larger than 11 eV are able

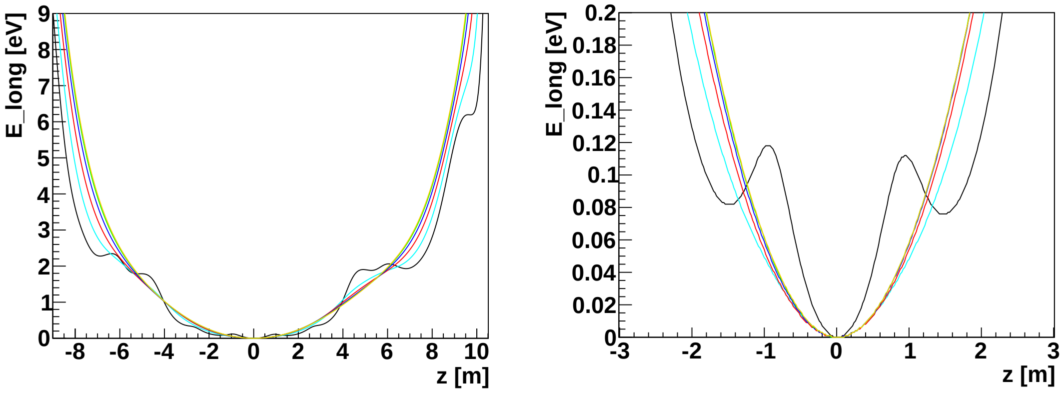

Figure 4.10: Longitudinal energy along field lines of the *local magnetic field minima solution* shown in figure 4.6. ***Left***: Local minima occur on the outer most magnetic field lines. ***Right***: A zoom into the interesting region around the analysing plane. The electrons started at the source with the maximum starting angle $\theta = 51^\circ$ and the corresponding transmission energy $E_{trans} \approx 18584$ eV. The local minima of the longitudinal energy are less deep and the transmission condition is fulfilled easier.

to excite the residual hydrogen molecules. When these go back into their ground state, a photon will be emitted. Since photons can not be shielded by magnetic fields, they can enter the flux tube, and, in case that their wavelength is small enough, ionise the residual gas molecules there [80].

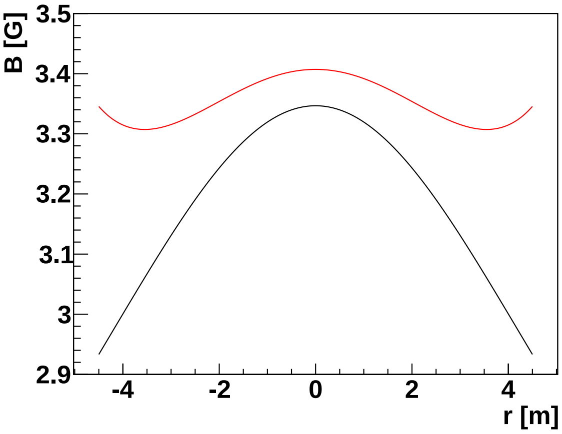

Figure 4.11: Radial inhomogeneity at the analysing plane. ***Black***: *Global magnetic field minimum solution.* ***Red***: *Local magnetic field minima solution.* The radial homogeneity is better in the presence of local magnetic field minima which is advantageous for the analysis of the measured β-spectra of each detector pixel.

Figure 4.11 compares the two configurations with respect to the radial homogeneity of the magnetic field in the analysing plane. In case of the *local magnetic field minima solution* a better homogeneity is reached. As discussed in section 4.1, the more homogeneous the magnetic field the less smearing occurs in the transmission function. The width of the transmission function is defined more precisely which is advantageous for the analysis of the measured spectra. While the demand for a maximum inhomogeneity of 10% is easily fulfilled for the *local magnetic field minima solution*, it is more critical for the *global magnetic field minimum solution.* An inhomogeneity of 12.5% could be just at the borderline. In addition, the *local magnetic field minima solution* features a better magnetic shielding at the crucial region $|r| < 3$ m, offering the advantage of less μ-induced background.

4.4.2 Test Measurement Setup

An important goal of the test measurements is the optimisation of the magnetic field with respect to background and transmission properties. In particular, the test measurements are supposed to give an insight on whether the *local magnetic field minima solution* or the *global magnetic field minimum solution* is preferrable. Furthermore, the advantages and disadvantages of different magnetic field strengths in the analysing plane will be tested during this project phase.

The ampere turn values of the LFCS coils are computed in the same manner as in the case of the final setup. In the following the results for a 6 G configuration are shown exemplary. A possible set of ampere turn values for 3 G, 3.5 G, 4 G, 5 G and 6 G with two local magnetic field minima and one global magnetic field minimum, respectively, can be found in Appendix B.

As in the case of the final setup, the field lines within the flux tube and the magnetic field strength along these field lines were computed and can be found in figures 4.12 and 4.13. The flux tube is more compressed than in the case of 3.5 G due to the higher magnetic field strength. The distance to the inner electrodes is larger. Hence, the potential around the analysing plane is very homogeneous, as shown in figure 4.14, and the transmission condition is fulfilled easier. This is visualised in figure 4.15.

It has also been checked that in the *global magnetic field minimum solution* no local magnetic field minima occur inside the vessel to avoid trapped particles. Secondary electrons from ionisations could move into the flux tube due to non-axially symmetric magnetic fields. Furthermore, there is the possibility for the production of photons, which can not be shielded from the sensitive volume by the magnetic field. If they move into the flux tube they could create secondary electrons due to photo-ionisation of the residual gas molecules. Therefore, these traps have to be avoided. Field lines outside of the flux tube have to be considered and are shown on the left hand side of figure 4.16. The corresponding figure on the right hand side demonstrates that local magnetic field minima only occur outside of the vessel.

Finally the homogeneity of the magnetic field in the analysing plane for the two configurations is compared in figure 4.17. Here again, the *local magnetic field minima solution* yields a better result. In both cases the percental homogeneity increases with increasing magnetic field strength. The homogeneity can be increased by choosing the LFCS currents the proper way. For higher magnetic field strengths, the contribution of the LFCS is larger, and, hence, the homogeneity can be improved further.

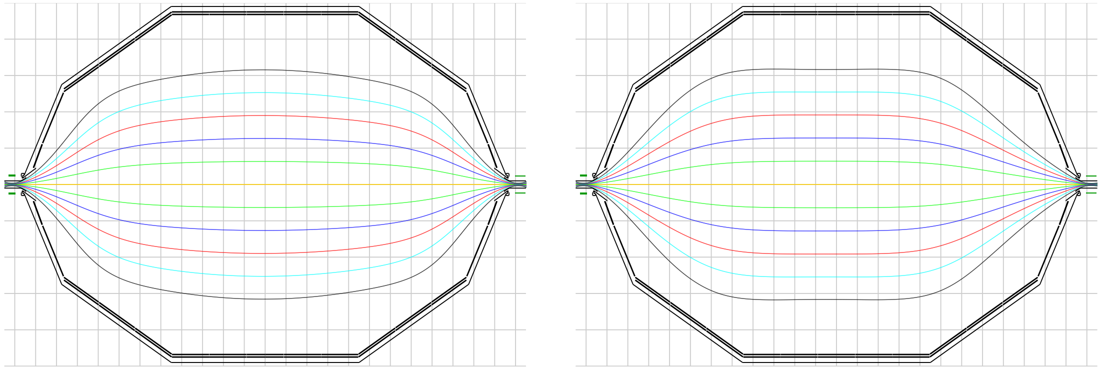

Figure 4.12: Magnetic field lines of the flux tube. ***Left***: Field lines corresponding to the *global magnetic field minimum solution.* ***Right***: Field lines corresponding to the *local magnetic field minima solution.* The grid has a scale of 1 m × 1 m.

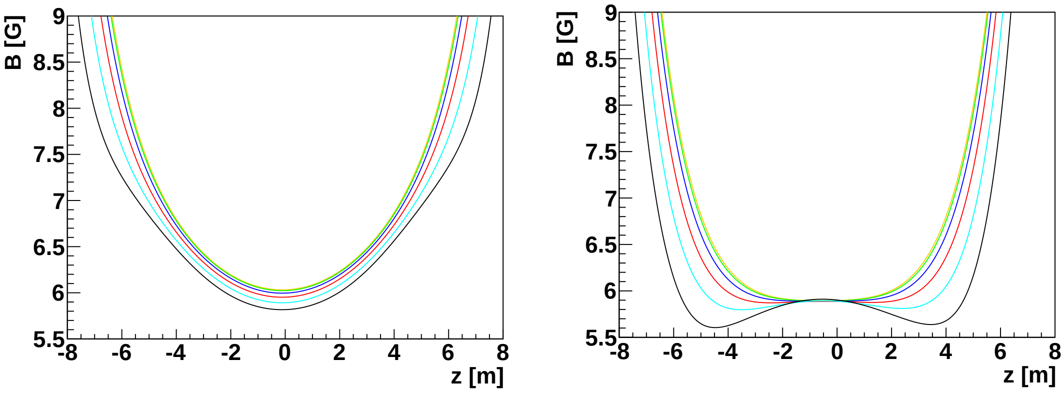

Figure 4.13: Magnetic field strength along field lines shown in figure 4.12. ***Left***: *Global magnetic field minimum solution.* ***Right***: *Local magnetic field minima solution.* Again, local minima only occur on the outer field lines (black and light blue).

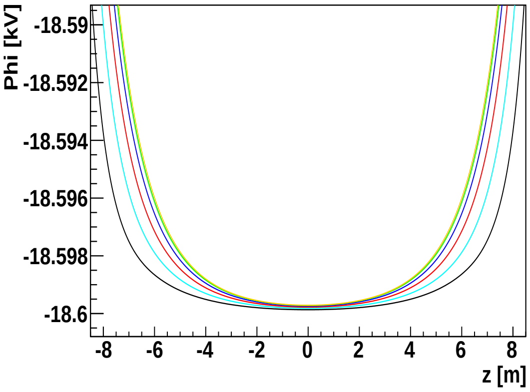

Figure 4.14: Electric potential along field lines shown in figure 4.13. Only one plot is shown because a difference between the two configurations is not visible by eye. Due to the increased distance of the flux tube from the inner electrodes, there are no local minima of the electric potential.

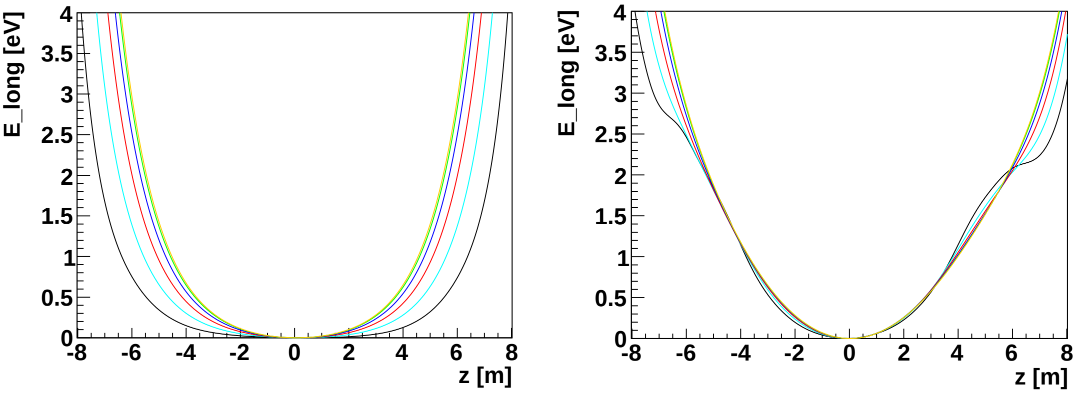

Figure 4.15: Longitudinal energy along field lines shown in figure 4.6. ***Left***: *Global magnetic field minimum solution.* ***Right***: *Local magnetic field minima solution.* The electrons started at the source with the maximum starting angle $\theta = 51°$ and the corresponding transmission energy $E_{trans} \approx 18600$ eV. Outside of the analysing plane, the longitudinal energy is generally higher in the presence of two local magnetic field minima, which is advantageous concerning the transmission condition.

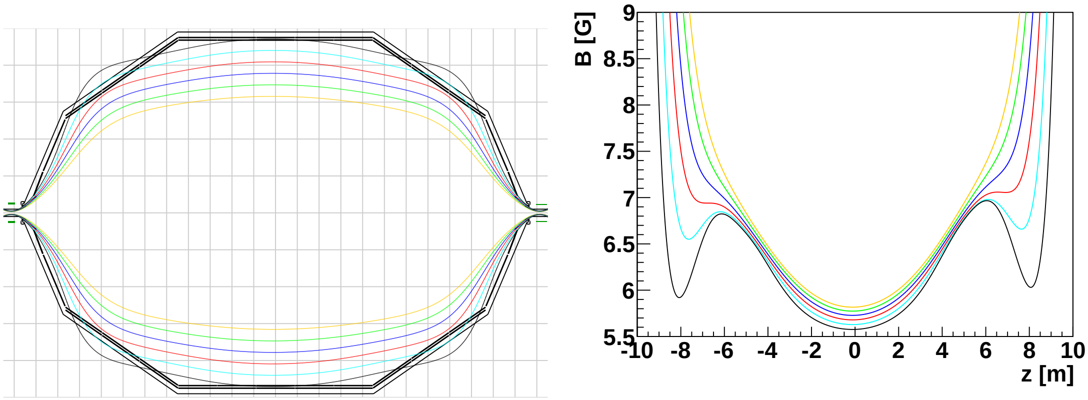

Figure 4.16: Field lines outside of the flux tube for the *global magnetic field minimum solution* of the 6 G test setup. ***Left***: Visualisation of the field lines. ***Right***: Magnetic field strength along the field lines. There are no local magnetic field minima occuring inside the spectrometer vessel.

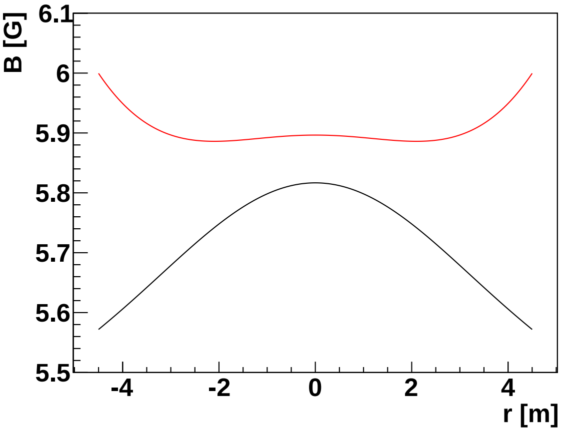

Figure 4.17: Radial inhomogeneity at the analysing plane.. ***Black***: *Global magnetic field minimum solution.* ***Red***: *Local magnetic field minima solution.* The radial and axial homogeneity is better for the *local magnetic field minima solution.*

The test measurements programme should thus include the following points:

- Measurement of the magnetic field with the air coil system and the superconducting magnets with the goal to gather the correct input parameters for the simulation and to validate the calculations done with it.

- Test of the influence of a flux tube touching the inner electrodes and the vessel: This can be achieved by lowering the magnetic field strength in the analysing plane below 3 G. It has to be tested if such a setup leads to an increased background and its quantity has to be determined.

- Measurement of the background dependence on the magnetic field strength in the analysing plane by varying the magnetic field strength and hence the flux tube size so that a *magnetic shielding factor* can be determined.
- Investigation of the influence of potential non-axially symmetric components of the magnetic field in the area of the analysing plane: A well-defined non-axially symmetric field can be produced, for example, by the EMCS. It is designed in such a way that the flux tube can be shifted by ±0.5 m in x- and y-direction. This is needed to identify a possible background increase due to motion of external particles into the flux tube.
- Test of the behaviour of the *local magnetic field minima solution*: Particles can be stored in these local minima due to the magnetic mirror effect. It has to be tested if these stored particles lead to an increase in background compared to the *global magnetic field minimum solution.*

4.4.3 Mechanical and Electrical Coil Layout

After installation of the mechanical support structure the whole system has to be instrumented with cables to carry the current. The ampere turns values of the different coils depend on the magnetic field strength that has to be reached in the analysing plane. Furthermore, there is a difference between the test measurement setup and the final setup. This section shortly summarises the results.

Layout of coils LFCS1-13

The numbering of the LFCS coils is visualised in figure 2.9. The following considerations were taken into account:

1. The current should be well below the cables limit of 205 A to avoid high temperatures.
2. For most coils the existing 200 A power supplies with a maximum voltage of 15 V will be used.
3. The material and operating costs have to be minimised [43].

The first two requirements limit the maximum value of the ampere turns. The calculations, which were discussed in this chapter, showed that a minimum of 500 ampere turns are needed for both the test measurement and the final setup. Presumably, there will be only two superconducting coils available during the initial phase of the test measurements. Therefore, coil LFCS1 has to make up for the loss in field strength at the source side. Hence, there has to be the possibility to operate this coil with up to 1500 ampere turns.

The ideal number of windings had to be found by optimising the operating costs. A detailed description can be found in [43]. For coils LFCS2-13 an initial number of 8 turns will be used. While the mechanical support structure allows for an increase in number of turns by 6, coil LFCS1 is equipped with 14 turns from the start because of the high ampere turns value required for the initial tests.

Layout of coils LFCS14 and LFCS15

The coil which is closest to the detector has two functions. During the test measurement phase this coil has to be operated in analogy to coil LFCS1. In the final setup the solenoid field of the detector side magnets has to be weakened substantially which requires a minimum number of 1600 ampere turns. Therefore, more turns are needed for this coil. The minimum value would have been 28 turns with the possibility to add more turns. This would have exceeded the mechanical strength of the support structure and it was decided to divide this coil up into two rings, LFCS14 and LFCS15, which are spaced closely together and carry 14 coils each.

4.5 Comparison between the Configurations

Both the *global magnetic field minimum solution* and the *local magnetic field minima solution* have been presented in detail. In the first part of this section, the advantages and disadvantages will be summarised shortly. The second part describes corresponding work dealing with a Monte Carlo simulation of 10^5 low-energetic electrons to gain further insight into the trapping behaviour within global and local magnetic field minima.

4.5.1 Advantages and Disadvantages

Magnetic Field Strength

A higher magnetic field strength in the analysing plane increases the distance of the flux tube from the wall. Hence, any electron emitted form the wall has to travel a larger distance in order to reach the flux tube. Furthermore, there are no local minima of the electric potential which could work as particle traps. As a result, the non-existence of local minima in the longitudinal energy facilitates the fulfilment of the transmission condition.

The magnetic mirror effect is less effective because the trap is less deep due to the higher magnetic field strength at the position of the minimum, leading to a decreased probability of trapping electrons.

The clear disadvantage of such a scenario is a decreased energy resolution. The transmission function gets broadened which reduces the count rate at the detector. In addition, a more precise knowledge of the shape of the transmission function is needed for the analysis.

Magnetic Field Minima

The existence of local magnetic field minima, and hence a local magnetic field maximum in the analysing plane, lowers the risk of violating the transmission condition.

A better radial homogeneity at the analysing plane can be achieved by the *local magnetic field minima solution* at the cost of a broadened transmission function for most of the detector subplanes. The consequences have already been mentioned above.

Furthermore, the *local magnetic field minima solution* could possibly lead to an increased background due to additional traps in the region of these local minima, caused by the magnetic mirror effect. This has been investigated with the help of particle tracking simulations. The results will be presented in the following section.

4.5.2 Particle Trapping due to Local Magnetic Field Minima

The *singletraj* programme package of chapter 3.3 was used to investigate the effects of local magnetic field minima on the trapping behaviour of electrons. The exact calculation method was used to ensure most accurate results at the cost of an increased calculation time. About 100,000 electrons were started equally distributed across the whole volume of the main spectrometer with a small kinetic starting energy $E_{kin} < 30$ eV. Such low energetic electrons could be created by several processes:

- Ionisation processes of the residual gas molecules by electrons or fast ions.
- Operating Penning traps can create photons which, in turn, create secondary electrons due to photo-ionisation [80].
- Secondary electrons, emitted from the walls, can enter the flux tube in case the magnetic field is not perfectly axially symmetric.
- Negative ions may also enter the fluxtube and lose their excess electron there.
- Even though the number of tritium molecules inside the spectrometer is reduced down to a partial pressure of 10^{-20} mbar, the so-called *shake-off* process [81] could lead to a significant electron background rate. The tritium molecules inside the main spectrometer will decay eventually and emit a 'normal' β-electron. Because most β-electrons have a kinetic energy larger than 1 keV and will be produced in a region with $U_{ret} \approx 18.6$ V, they can be discriminated by the detector due to their increased energy $E = E_{kin} + qU_{ret} > 19.6$ keV. But due to the charge change in the β-decay process and the fast escape of the β-electron, an abrupt perturbation of the electrostatic environment is felt by the remaining electrons. This can lead to an excitation and even to an ionisation of low-energy 'shake-off' electrons which can not be discriminated from the signal rate anymore. The probability of electron loss is proportional to $1/Z_{eff}^2$[4].

The starting parameters such as position, energy, polar and azimuthal angle, were generated with the Monte Carlo generator of chapter 3.3. The electrons were emitted isotropically.

Global magnetic field minimum solution

The black markers in figure 4.18 indicate the reversal points of electrons trapped by the intrinsic magnetic mirror trap due to the global magnetic field minimum. The plot nicely reproduces the maximum flux tube which would fit inside the vessel. More electrons are stored in a region further away from the analysing plane, i.e. further away from the global minimum. Only those electrons with very large starting angles and starting positions close to the analysing plane can be stored directly around it. This is visualised by the white area around $z = 0$ m. When moving towards the border of the flux tube, the axial position of the global magnetic field minimum is shifted slightly

---

[4] Z_{eff} is the number of protons an electron in the element effectively 'sees' due to screening by inner-shell electrons.

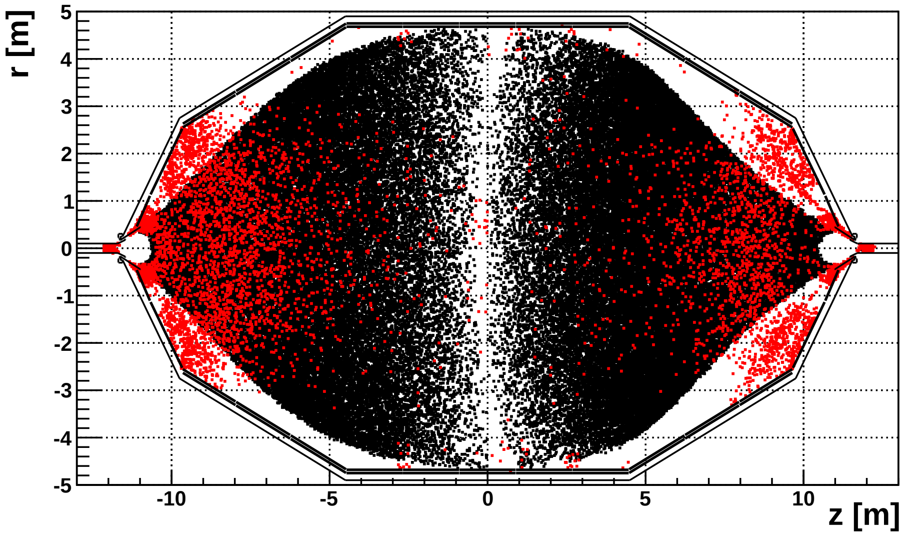

Figure 4.18: Reversal points of trapped electrons for the global magnetic field minimum solution. Low energetic electrons were started equally distributed within the whole main spectrometer. Due to the magnetic mirror effect and the electrostatic potential barrier, about 2/3 of all electrons are trapped. For each trapped electron, two markers indicate the reversal points of its track. ***Black***: Reversal points of electrons, trapped due to the magnetic mirror effect. ***Red***: Reversal points of electrons, trapped due to the mixed trap. The maximum flux tube which fits into the vessel is visible. The white region at the analysing plane shows the position of the global magnetic field minimum.

towards positive z-values. But since the electric potential is sufficiently homogeneous around the analysing plane, this does not have an effect on the transmission properties of this configuration.

The red markers indicate electrons which are trapped by the magnetic mirror on the one side and by the electric potential barrier on the other side. The position of the reversal points due to the magnetic mirror coincide with the position of maximum magnetic field. The position of reflection by the potential barrier depends on both the starting energy and the starting polar angle of the electron.
It is visible that more electrons are trapped in the source-side half of the spectrometer than in the detector-side half. This is due to the larger magnetic moment of the detector-side superconducting magnets. The magnetic field is generally higher in this region, reducing the probability for electrons generated in this region to be stored. Following equations (4.8) and (4.9), the maximum starting angle of an electron, in order *not* to be stored, can be calculated:

$$\theta_{max} = \arcsin\left(\sqrt{\frac{(E_{start} + qU_{ret}) \cdot B_A / B_{max}}{E_{start}}}\right). \tag{4.13}$$

The maximum accepted starting angle is larger in the source-side half of the spectrometer.

In a region close to the entrance and exit of the main spectrometer, there are no reversal points of stored electrons. According to equation 4.13, all electrons, starting in this region with a kinetic energy smaller than 70 eV, can not be stored. The electric potential increases rapidly in this region, accelerating electrons to such an extent that they can not be stored by the magnetic mirror trap anymore.

Local magnetic field minima solution

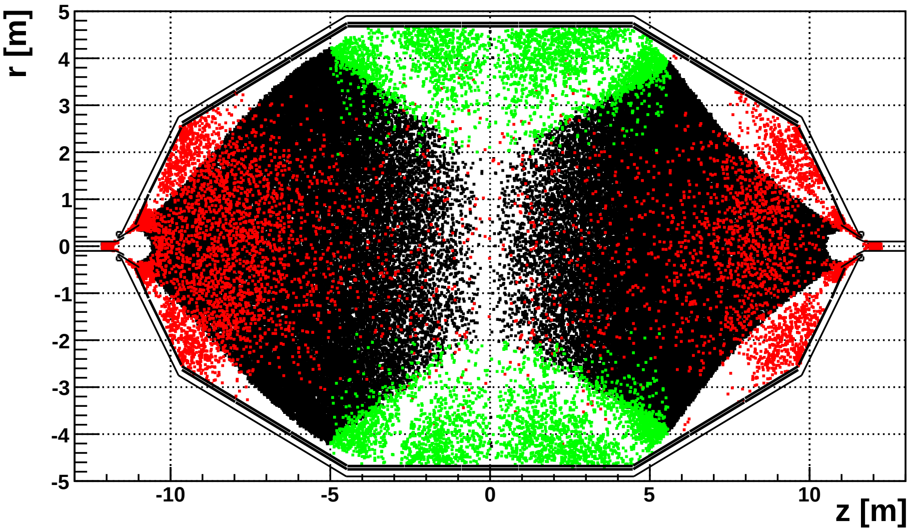

Figure 4.19: Reversal points of trapped electrons for the local magnetic field minima solution. ***Black***: Reversal points of electrons, trapped due to the global magnetic mirror. ***Green***: Reversal points of electrons, trapped due to the local magnetic mirror. ***Red***: Reversal points of electrons, trapped due to the mixed trap. In a configuration with two local magnetic field minima, electrons can get stored in these minima. Most of these stored electrons, however, would be stored anyway due to the intrinsic magnetic mirror of a MAC-E filter.

The results for the *local magnetic field minima solution* look different. Electrons, which started close to the analysing plane but further away from the beam axis, are not trapped due to the intrinsic magnetic mirror trap. Instead, they are trapped by the two small magnetic mirror traps caused by the local magnetic field minima of figure 4.7. This figure also shows that local minima only exist on the outer magnetic field lines. The effect increases further when moving towards the outside of the flux tube. Analoguously to the global minimum, electrons are trapped in a larger region around the local minima. The z-position of these minimum is again visualised by the gap between the green reversal points. Its distance to the analysing plane increases when moving off-axis. In the region between $r = \pm 2$ m, the gap between the black markers indicates the position of the global magnetic field minimum. Further outside, the white area between the green reversal points at the position of the analysing plane marks the position of the local magnetic field maximum.

Results

Table 4.3 shows the results of the simulation in numbers.

	1 minimum [%]	2 minima [%]
Transmitted	19.5	19.5
Absorbed	14.3	11.0
Stored	66.2	69.5

Table 4.3: Comparison between the simulation results for the *global magnetic field minimum solution* and the *local magnetic field minima solution.*

The rate of transmitted electrons is approximately the same for both configurations.
In case of the *global magnetic field minimum solution* about 66% of all electrons are stored due to the intrinsic magnetic mirror trap. For the *local magnetic field minima solution*, the number of trapped electrons is 3% higher and is composed of 46.5% due to the intrinsic magnetic mirror trap and 23% due to the local magnetic mirror traps. This demonstrates that the about 90% of all electrons, stored in the local magnetic field minima, would be stored anyway due to the intrinsic global magnetic mirror trap. This is also visualised in figures 4.18 and 4.19. here, the reversal points of the electron tracks are shown. In the region of the local magnetic field minima, indicated by the green markers, no additonal electrons can be stored due to the intrinsic magnetic mirror trap. The reversal points of electrons, trapped within the global magnetic field minimum are visualised by the black markers.
In turn, within the *global magnetic field minimum solution* 3% more electrons hit the inner electrodes than within the *local magnetic field minima solution.* This is also revealed by the figures. The maximum flux tube which fits into the vessel is larger for the *local magnetic field minima solution* because it is flatter in the vicinity of the analysing plane. Effectively, this should result in a larger number of transmitted electrons but the storage conditions are more disadvantageous, neglecting this effect.

Within this simulation, an electron hitting a part of the inner electrode was always absorbed. In reality, though, a significant number of electrons could get reflected. In case of a silicon surface, this has been investigated by [82]. Inside the spectrometers, stainless steel is the most commonly used material. The simulations thus have to be extended in order to take this effect into account.

4.6 Conclusions

A magnetic field configuration, which satisfies all requirements on the electromagnetic design of the main spectrometer for the standard solution with one global magnetic field minimum, has been discussed. Furthermore, a possible alternative solution with two local magnetic field minima was investigated. It was found to have better transmission properties than the standard solution in addition to a better radial homogeneity in the analysing plane. As magnetic field minima serve as particle traps due to the magnetic mirror effect, increased trapping conditions were expected for this alternative configuration.

Nevertheless, from a simulation point of view, there is no significant additional background to be expected from the *local magnetic field minima solution* compared to the *global magnetic field minimum solution*. The calculations, presented in this chapter, show that about 90% of all electrons, which are stored in the local magnetic field minima, would be stored anyway in the global magnetic field minimum.

There are still effects which were not taken into account by the simulation yet. Due aspect is a detailed simulation of the magnetic shielding effects of both configurations at large radii in the analysing plane. There is the possibility for electrons being reflected from surfaces or non-axially symmetric electric and magnetic fields leading to drift velocities into and out of the flux tube. Therefore, on the one hand, the simulations have to be extended concerning these effects and on the other hand, extensive test measurements are needed. Some proposals for such measurements were given in section 4.4.

5. Magnetic Field Monitoring System

The correct determination of the transmission function requires the knowledge of the magnetic field strength with a precision of 1%. An incorrect value for the width of the transmission function would lead to a systematic error of the neutrino mass.
In addition, the magnetic field has to satisfy all experimental demands outlined in chapter 4.1.
Therefore, a magnetic field measuring and monitoring system is needed.
All these physical requirements address the magnetic field inside the vessel. After completion of the installation of the inner wire electrodes, however, there will be no prospective possibility to directly measure the magnetic field inside the tank. Hence, a strategy of an indirect measurement has to be developed.
The first section 5.1 introduces the measurement principle, while in the second section 5.2, the accuracy requirements on this measurement will be determined. The last section 5.3 provides a method for an implementation of this system.

5.1 Principle

The method described below is based on the precise knowledge of all magnetic field sources. With this information, a simulation programme can calculate the magnetic field strength at any desired point in space. The validity of this simulation has to be tested within the framework of test measurements. After the validation of this strategy, the problem is reduced to a control and monitoring of the behaviour of the magnetic field sources.
On the one hand, magnetic field sensors are used to determine the properties of the sources which are needed as input for the simulation. On the other hand, they are used to control the simulation programme.

The advantage of this method is that a relatively small number of sensors is required. For any interpolation method, a close meshed grid of magnetic field values is needed which requires a large number of expensive high precision sensors.
However, it is disadvantageous that this method relies on a precise description of the magnetic field sources. Obviously, only a limited number of input parameters can be implemented, and, therefore, reality is reflected in a simplified way.

Besides the determination of the magnetic field inside the main spectrometer, the magnetic field monitoring system will also monitor the magnetic field in the pre-spectrometer, monitor spectrometer and transport section.

5.1.1 Description of Magnetic Field Sources

The magnetic field sources, which have to be simulated, can be divided into six types:

1. Superconducting coils: Detector and pinch magnet, the two pre-spectrometer magnets and the magnet chain in the source and transport section most directly affect the magnetic field in the main spectrometer.
2. CPS and DPS: Due to the intrinsic tilt of the transport section magnets, magnetic stray fields influence the axial symmetry of the magnetic field in the main spectrometer.
3. Low Field Coil System: The LFCS contributes approximately half the amount of the superconducting coils to the magnetic field in the analysing plane.
4. Earth Magnetic field Compensation System: The EMCS will compensate the earth's magnetic field with up to 99% efficiency in the analysing plane.
5. Monitor spectrometer: The second beam line of the monitor spectrometer yields another contribution to the magnetic stray fields.
6. Magnetic materials: The main spectrometer hall itself is partly made of magnetic materials, mainly in the form of steel reinforcements. Due to their residual magnetisation they contribute to the magnetic field in the main spectrometer volume.

Finally, there are other sources which are not included in the simulation. These might be for example the ANKA synchrotron, solar related activities or other temporary or constant, yet unknown, sources. Their influence, though, should be small enough to be neglected. Otherwise, the deviations can be detected with a permanent monitoring system. If the cause can be found, the data can be corrected, and, if not, they might have to be rejected.

In order to describe these sources most precisely, a certain set of generic parameters has to be defined. The air coil system, the superconducting coils and the monitor spectrometer are exhaustively defined by their geometrical and electrical properties. Geometrical properties are position z, orientation, inner and outer diameter r_i, r_a and length of the coils l. The electrical property is the electric current running through the coil windings. These are the input parameters needed for the magfield3 programme package of chapter 3.1. Especially the definition of how to describe a coil's orientation can be found there. The programme was used to calculate the deviation from axial symmetry due to a misalignment of single coils and whole groups of coils. The results are shown in the next section.

The earth's magnetic field can directly be measured, as well as the (small) magnetic field remaining after turning on the EMCS. The sources which are most difficult to assess quantitatively are the magnetic materials, as the permeability and the remanent magnetisation of these sources are difficult to determine. A first approach can be found in [46]. The results will be used as direct offset to the magnetic field of the coils.

5.2 Accuracy Requirements

The most constraining requirement for the magnetic field is the demand for axial symmetry. A system of high precision sensors, spread along the entire length of the tank, will be needed. The measurement accuracy is determined by the non-axially symmetric field contributions of the various magnetic field sources, shown in table 5.1. The contribution of all sources together may not exceed 0.1-0.5% of the total value of the magnetic field. The distribution among the single sources is done by their individual percental contribution to the total field value. The lower values in table 5.1 correspond to the magnetic field strength in the analysing plane. The higher values correspond to a position close to the superconducting magnets at the entrance and exit of the main spectrometer.

Source	Deviation from axial symmetry [mG]
Tilt (0.5°) of superconducting coils	1-5
Tilt (0.5°) of LFCS coils	1-10
CPS, DPS	0.3
Monitor spectrometer	2-10
Magnetic materials	3-20
EMCS	1-5

Table 5.1: Non-axially symmetric field contributions of different magnetic field sources.

The contribution of a potential tilt of the superconducting coils and the LFCS, as well as the intrinsic tilt of the DPS and CPS coils was calculated with the help of the magfield3 programme package. The influence of the monitor spectrometer is a result of the magnetic field of its solenoids and its distance to the main spectrometer. There is no simulation programme existent yet for a calculation of the magnetic field created by the magnetic materials. Therefore, the corresponding values are just an estimate under consideration of the measurements done inside the hall. The inhomogeneity of the field created by the EMCS leads to a partially remaining earth magnetic field contribution which can be calculated analytically.

5.3 Realisation

The magnetic field monitoring system consists of two major parts. The first task is the determination of all input parameters of the simulation. A precise knowledge of all sources has to be achieved. The second part is concerned with controlling the simulation. The required measurements can accordingly be divided into *one-time* and *permanent measurements.*

One-time Measurements

The determination of the geometry of the superconducting coils will mainly be performed by a movable magnetic field sensor table [83]. Since their position, orientation and spacial measures will not change in time, this will be a *one-time measurement.* The geometry of the air coil system will also be determined once, after its completion with a mechanical measurement.

The earth's magnetic field has already been measured very precisely with a sensor of the range of 10 G and a precision of 1 mG in [46].

Finding the influence of the magnetic materials to the magnetic field inside the spectrometer volume is most challenging. The magnetisation of the materials inside the walls, platforms and columns of the spectrometer hall have to be known in order to be able to simulate their magnetic field. To determine the magnetisation, the magnetic field close to the walls was measured in [46]. Once the superconducting coils are mounted and can be operated, this measurement has to be repeated due to possible changes of the magnetisation or hysteresis effects.

Once all sources are investigated, the simulation programme is equipped with these precise input parameters and optimised for simulating the magnetic field at the points of interest. The result has to be checked by a *one-time mesurement* of the magnetic field at many points in space. These measured values will be compared to the simulated ones. The deviation of measured and simulated values should not exceed the accuracy requirements for the magnetic field sensors of table 5.1.

Permanent Measurements

The current of the LFCS coils will be measured by current measuring devices. This is not possible for the superconducting magnets. Therefore, their current will be monitored indirectly by magnetic field sensors, which are permanently attached to these coils. They have to tolerate a magnetic field strength of up to a few tesla while sustaining a precision of about 50 mG. Since the electric current is not necessarily a constant parameter, it has to be monitored *permanently.*

Although the stability of most of the input parameters is hereby monitored permanently, additional control sensors are necessary. They will be positioned at various key points in space. The simulation programme will calculate the expected magnetic field value at these points and the sensors will be in charge of recording any deviations. These can occur, for example, if source parameters change or unconsidered sources influence the magnetic field.

The precision and position requirements of the control sensors are determined by the physical requirements for the magnetic field of section 4.1. The most stringent and constraining factor is the demand that these sensors have to be sensitive to a deviation from axial symmetry of 0.1-0.5% along the whole beam axis of the main spectrometer. To fulfil this condition, the control sensor system will consist of 30 sensors in total, arranged in rings around the vessel at seven different z positions as indicated in figure 5.1. The most interesting region is in the vicinity of the analysing plane. Hence, 14 sensors of the range up to 10 G with a precision of $1-2$ mG are planned to be attached in three rings in the cylindrical region. Another 16 sensors will monitor the region of the cones and steep cones. These have to bear a higher magnetic field strength of up to 50 G. Correspondingly, a lower precision of about 50 mG is sufficient. The precision values are a direct result of the influence of the different magnetic field sources on the

deviation from axial symmetry, shown in table 5.1.
The monitor spectrometer will also be equipped with 6 control sensors of the range of 10 G with a precision of about 50 mG.

Figure 5.1 shows the influence of an inaccuracy of both the position and the orientation of the sensors. It was assumed that a precision of the position of 0.5 cm and a precision of the orientation of 0.1° is achievable. With the help of the magfield3 package the resulting deviations of the three magnetic field components B_z along the beam axis, B_r in radial direction and B_t in transversal direction, were calculated. While the position inaccuracy does not have much of an effect, a tilt around the z-axis will change especially the radial and transversal components drastically. Therefore, the sensors will have to be aligned very carefully. On the other hand it should be sufficient to monitor just the total magnetic field value. The source of the magnetic field deviation will be harder to identify, however.

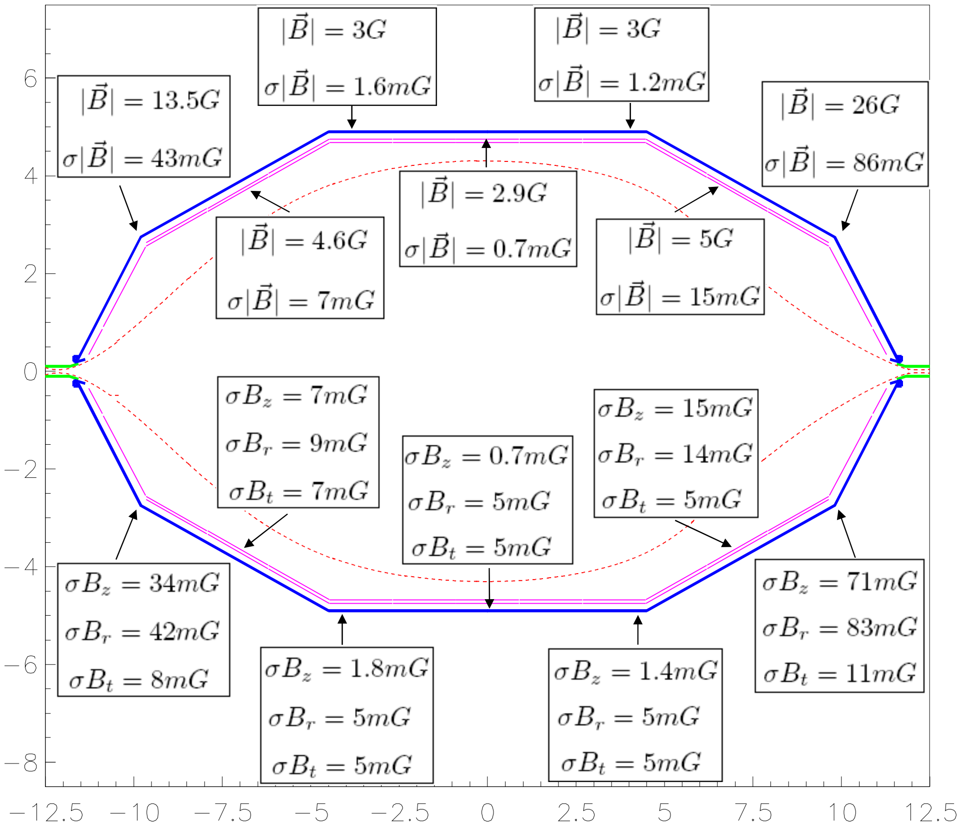

Figure 5.1: Impact of a misalignment of the magnetic field sensors. The arrows indicate the approximate, preliminary axial position of the sensors. The upper half shows the total magnetic field strength and its deviation due a deviation of position of 0.5 cm and a tilt of 0.1°. The lower half shows the deviations of the axial, radial and transversal magnetic field components due to the same misalignment.

5.3.1 Data Storage and Availability

An overview of all types of sensors can be found in table 5.2 below.

Type	Range	Precision	Purpose	Position	Number
C1	10 G	1-2 mG	Monitor low magnetic field inside main spectrometer; ensure experimental requirements	1 ring (6 sensors) at $z = 0$ (analysing plane); 2 rings (4 sensors each) at $z = \pm 3.6$ m	14
C2	50 G	50 mG	Monitor high magnetic field inside main spectrometer; ensure experimental requirements	4 rings (4 sensors each) at $z = \pm 6.8$ m and $z = \pm 9.95$ m	16
MS	10 G	50 mG	Monitor magnetic field inside monitor spectrometer	1 ring (6 sensors) at $z = 0$ (analysing plane);	6
CS	1 T	50 G	Monitor electric current of superconducting coils at the spectrometers	next to the coils	6

Table 5.2: Overview of the different sensors needed for the magnetic field monitoring system.

Prospectively, the permanent sensors will be read out on a scale of 1 to 10 seconds. These data will be streamed to the slow control system. Since the monitoring system acts as a control instance, ensuring the stability of a certain configuration, it should be sufficient to save the data only every 1 to 10 minutes in the database.

There are two options of providing magnetic field data to the users. Ideally, every user does an analysis based on an 'official' magnetic field map. Therefore, it is necessary to introduce standards. The options are described in the following. They can both be used complementary to each other. Figure 5.2 shows an overview of the possible structure.

Option 1

As soon as the simulation is validated by the experimental results, a magnetic field map can be calculated for any given electromagnetic setup. This map will contain a description of the magnetic setup and a list of parameters such as three values for the position and six values for the magnetic field components and their respective errors. If enough positions are recorded, the magnetic field at any point in space can be calculated from the map by interpolation. This map will be made available to the analysis coordinators, who have to agree on an interpolation algorithm to ensure that everyone obtains the same magnetic field from the same map.

This option is attractive in case that the field of interest is in a region with low gradients, for example in the analysing plane. For particle tracking, this method is probably too imprecise, while keeping the magnetic map at a reasonable size.

Option 2

The second option is to store the actual input file for the simulation of the magnetic field. This file contains every relevant parameter of every single magnetic field source. In this case, the routines for calculating the magnetic field at any point of interest have to be standardised. Otherwise, different implementations could produce different field values and only one implementation has been checked with sensor data.
The user will have to operate a magnetic field simulation programme using the input file which describes the current magnetic setup.

This method is preferrable because the simulation programme can calculate the magnetic field strength at any point of interest directly and there is no need for an interpolation. Therefore, the programme package is currently being restructured and translated into a C++ code version [84] to make it more flexible and versatile.

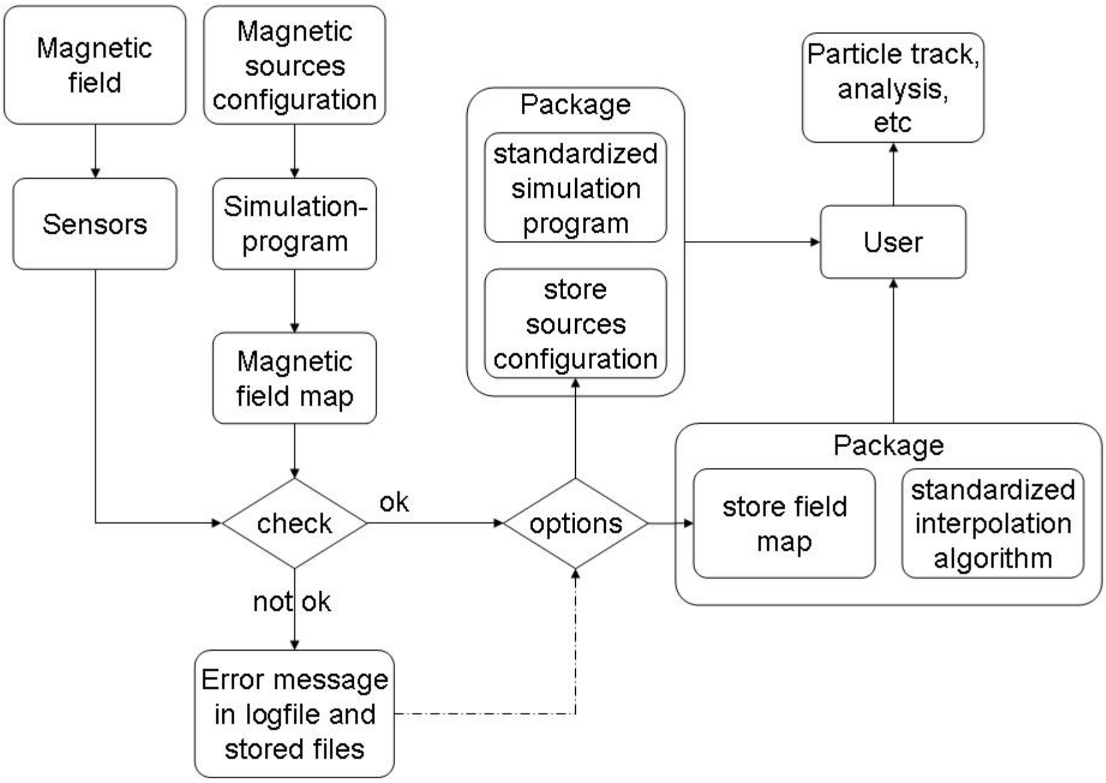

Figure 5.2: Possible data format for magnetic field monitoring system. The organisation of data storage and availability is shown.

6. Particle Trapping due to Column Density Scans of the Tritium Source

The spectrometer transmission function (2.6) obviously does not take into account any interactions of β-electrons inside the source. In case of undergoing inelastic scattering on the tritium molecules the electron will experience an energy loss. Therefore, such electrons may not be able to pass the analysing plane which results in a modification of the transmission function. This modified function, the so-called response function of the KATRIN experiment, will be presented in the first section 6.1 of this chapter. In the following section 6.2 it will be shown how the determination of this function is related to a determination of the column density of the source. The measurement strategy will be presented in section 6.3 and the possible negative consequences for the background will be investigated in section 6.4. Section 6.6 shortly summarises the results of the simulations and section 6.7 offers a proposal for possible test measurements.

6.1 The KATRIN Response Function

Electrons moving through the gaseous tritium source have a certain probability to undergo inelastic collisions with the tritium molecules. These processes can be described by folding of the corresponding inelastic cross section with the distribution of electron path lengths through the source and the density profile for tritium molecules in the source [85]. Multiple scattering events are also included. A detailed description and investigation of these effects can be found in [86]. The most important processes are

- excitation: The total cross section for the excitation of molecular tritium is composed of the cross section for discrete excitation processes and the cross section for the dissociation of the molecule. The energy loss spectrum of the electrons has its maximum at an energy of 12.6 eV.
- ionisation: Due to the high energy of the β electrons only the formation of positive ions has to be taken into account, starting at an energy of ≈ 15.4 eV. The energy loss spectrum shows a weak continuum [87].

The response function of the KATRIN experiment $f_{res}(E, qU)$ is a convolution of the energy loss distribution with the transmission function $T(E, qU)$. The energy loss distribution is characterised by the normalised energy loss function

$$f(\Delta E) = \frac{1}{\sigma_{tot}} \cdot \frac{\mathrm{d}\sigma}{\mathrm{d}\Delta E}, \tag{6.1}$$

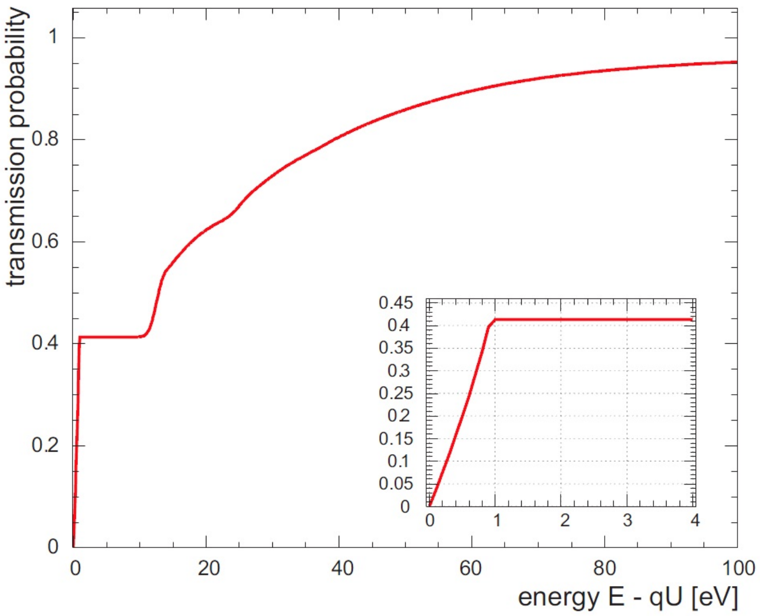

Figure 6.1: KATRIN response function [3] for isotropically emitted electrons with fixed energy E as a function of the retarding energy qU. The energy loss of electrons in the source (for a column density $\rho d = 5 \cdot 10^{17}/\mathrm{cm}^2$ and a maximum starting angle $\theta_{max} = 50.77°$) is folded into the transmission of unscattered electrons shown in the inlay.

where σ_{tot} denotes the total inelastic cross section and ΔE the energy loss of the β-electrons. Taking into account the scattering probabilities P_i $(i = 1, 2, 3...)$ for i-fold scattering in the source, the response function can be written as

$$\begin{aligned} f_{res}(E, qU) = \quad & T(E, qU) \otimes P_0 & + \\ & T(E, qU) \otimes P_1 \cdot f(\Delta E) & + \\ & T(E, qU) \otimes P_2 \cdot (f(\Delta E) \otimes f(\Delta E)) & + \\ & \ldots \end{aligned} \tag{6.2}$$

Figure 6.1 shows the normalised response function for monoenergetic electrons, which are isotropically emitted in the source, as a function of the retarding energy qU. Between 0 eV and 10 eV the response function is identical to the transmission function of the main spectrometer. Electrons, which scatter inelastically off tritium molecules in the source, always lose more than 10 eV kinetic energy. Hence, no modification of the transmission function occurs. These unscattered electrons account for 41.3% of all β-electrons. For lower retarding potentials, i.e. larger values of $E - qU$, the number of transmitted electrons increases. Electrons, which have lost energy due to inelastic scattering, are now able to pass the analysing plane and will be detected. The relative height of the different contributions[1] is determined by actual the column density ρd of the source.

---

[1] The plateau for unscattered electrons and the increasing contributions from 1-fold scattering and 2-fold scattering events can easily be identified.

6.2 Determination of the Column Density

The response function has to be measured very precisely for different column densities ρd in a special pre-measurement. This allows for a determination of the energy loss function. A description of this measurement can be found in [86]. Afterwards, the features of the response function will be monitored via repeated reference measurements of the column density. Monoenergetic electrons from an electron gun with an energy above the tritium endpoint will be sent through the WGTS. Their rates will be measured at three different retarding potentials corresponding to the mean values of the plateaus in figure 6.2, i.e. at 5, 20 and 40 eV above the endpoint. Comparing these rates allows for a determination of the column density ρd as a fraction of the mean free column density[2]

$$(\rho d)_{free} = \frac{1}{\sigma_{tot}} \tag{6.3}$$

with a 2‰ precision.

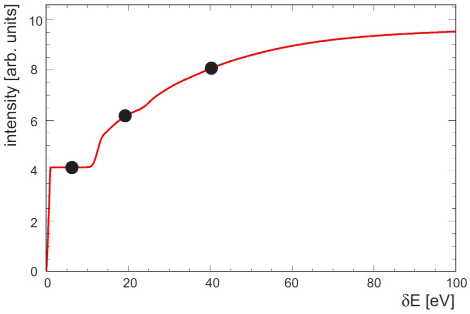

Figure 6.2: Schematic view of the column density determination. Electrons will be sent from an energetically sharp electron gun of energy E_e from the rear through the WGTS. The count rate at the detector will be measured at 3 different retarding energies $qU = E_e - \delta E$ (black dots).

Given that only the ratio is important, the rate of the electron gun does not need to be known absolutely, it only has to be stable over the time required for the different retarding voltage settings. On the other hand, if there is a way to stabilise or measure the electron gun intensity with sufficient precision, the column density could be determined by one retarding potential setting alone. This would reduce the measurement time and the rate of electrons entering the spectrometer by a factor of 3.

Measuring the column density at certain regular time intervals reduces the problem of ρd monitoring to 'statistical fluctuations' around this well known mean value. Unaccounted shifts in ρd of the order of a few 10^{-3} over the entire measuring period easily lead to an unacceptable bias in the observable m_ν^2 [3]. Therefore, it will be necessary to determine the column density during the actual tritium measurements on a regular basis. The β-activity of the source $\epsilon_T \cdot \rho d$ as well as the isotopical content ϵ_T [88] have to be measured. If both parameters are known with sufficient accuracy with respect to the values during the e-gun measurement, variations of ρd can be extracted and the data corrected for.

---

[2] The mean free column density can be seen analogous to a mean free pathlength, where σ_{tot} denotes the total inelastic cross section.

6.3 Scanning Strategy and Requirements

Calibration measurements, monitoring measurements and maintenance intervals limit the measurement time in the β-spectrum scanning mode. A proposal for a measurement scheme, taken from [3], can be found in figure 6.3. The first three months will be allocated to initial measurements, especially calibration measurements with monoenergetic electron sources. Each tritium run will be separated into $\approx$ 2 hours intervals, starting with a 5-minutes e-gun reference measurement of the relative column density discussed in section 6.2. The following 115 minutes are then separated into 23 intervals of 5 minutes each for the actual tritium runs. The first 30-seconds-interval, out of ten, will be used for a measurement of the source activity, resulting in a scanning efficiency of 91% during tritium runs. A β-spectrum scanning period would last about 60 days followed by a maintenance period of about one month. This interval is mainly defined by the CPS. By this time, the argon snow is expected to be saturated with tritium molecules. Therefore, the whole system has to be cleaned and new argon frost has to be applied to the inner CPS beamtube.

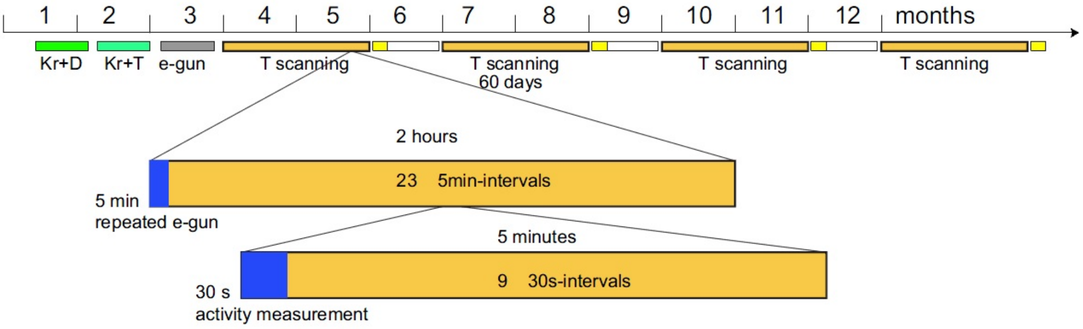

Figure 6.3: Measuring time distribution for a normal Tritium measuring mode of 60 days including monitoring and scanning phases. Also shown are initial calibration measurements as well as maintenance periods of about 30 days.

During those 5 minutes of repeated e-gun measurements, the rate at the detector will be measured for the three plateau energies sketched in figure 6.2. Therefore, an e-gun has to emit electrons with a very sharp gaussian energy distribution of $\Delta E \approx 0.2$ eV and a polar starting angle $\theta \approx 0°$ [89]. This e-gun will have to be installed in the rear section behind the source WGTS in a tritium environment.

If the column density is sufficiently homogeneous in radial direction the electrons will be sent along the beam axis only. Otherwise, dipole magnets in the DPS sections have to be used to shift the electron beam in radial direction. In this case, a method has to be implemented to systematically scan the whole tube area by adjusting the dipole magnet current. The feasibility of such a frequently occuring, fast change of the magnet current has to be tested.

For electrons with very small starting angles the normalised differential cross section for electron-tritium scattering has its maximum for small scattering angles, i.e. $1° - 2°$ [90]. Due to the increasing magnetic field towards the spectrometer, a maximum polar angle of about 10° at the position of maximum magnetic field is expected.

6.4 Implications for the Background Rate

During the column density measurements a large number of the order of 10^5 electrons per second will enter the main spectrometer. Even with the good vacuum of 10^{-11} mbar inside the KATRIN main spectrometer, a considerable amount of scattering events on the residual gas has to be expected. Every scattering process is associated with a change of the polar angle of the primary electron. Depending on the position of the event, a change of 10° might already be sufficient to trap the electron within the intrinsic magnetic mirror of the main spectrometer. This is visualised in figure 6.4. The electron started at $z = -12.13$ m, where the magnetic field has its maximum value. At a position $z \approx 3.5$ m behind the analysing plane, it scatters off a hydrogen molecule and its polar angle changes from 10° to 70°. As a result, the electron is trapped in a region ±5 m around the analysing plane, which is indicated by the blue rectangle.

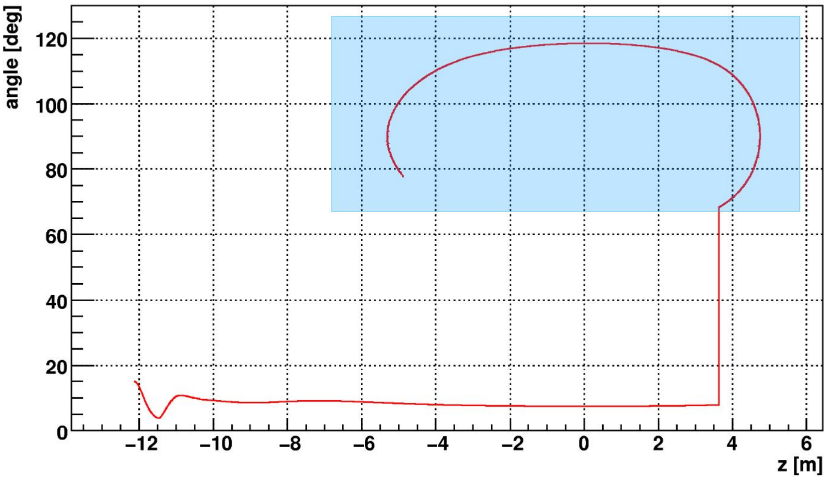

Figure 6.4: Electron trapping after a scattering event. The electron started off at the position fo maximum magnetic field at the entrance of the main spectrometer. At a position $z \approx 3.5$ m, it inelastically scatters off a hydrogen molecule. Its polar angle increases by 60° resulting in a trapping condition due to the magnetic mirror effect.

Furthermore, secondary electrons, which are isotropically emitted from molecules due to ionisation, could be trapped as well. In case of an adiabatic motion in a sufficiently axially symmetric magnetic field, trapped electrons can not leave the spectrometer without undergoing another scattering. Even then, their polar angle has to change in such a way that allows them to escape the magnetic mirror trap. If these trapped electrons leave the spectrometer *after* the 5-minutes measurement window, they will contribute to the background of the actual tritium measurements, possibly leading to an unacceptable systematic uncertainty $\sigma_{syst}(m_\nu^2) > 0.017 \text{ eV}^2$.

The probability P for electron-hydrogen elastic scattering can be calculated analytically [91] following equ. (3.20)

$$P = s \cdot \sigma \cdot n = 24 \text{ m} \cdot 10^{-19}\text{m}^2 \cdot 2.42 \cdot 10^9 \frac{\text{molecules}}{\text{m}^3} = 6.3 \cdot 10^{-9}. \qquad (6.4)$$

The pathlength $s = 24$ m is the approximate minimum travel distance between the superconducting magnets, where the magnetic field reaches a local maximum. The total cross section σ was taken from figure 6.5, specifically for electrons with a kinetic energy of the order of 1 eV. The number density n of the hydrogen molecules was already calculated in equ. (3.22).

This probability is an estimation because it does not take into account a variation of the kinetic energy of the electrons due to the variation of the electric potential. The escape probability strongly depends on the starting kinetic energy, the scattering angle and the magnetic field at the position of the scattering process. This is visualised in figures 6.6 and 6.7. Figure 6.6 shows that for higher kinetic starting energies, the allowed polar angles are limited to smaller values. For example, electrons with a starting kinetic energy of 5 eV have a trapping probability of 90% because they are only allowed a maximum polar starting angle of less than 30°. Assuming an isotropic emission, less electrons are produced with a small starting angle. Independent of its starting angle, the trapping probability is higher if the electron starts in a region with lower magnetic field strengths. This is visualised in figure 6.7.

Therefore, detailed simulations were performed to assess the storage time of trapped electrons.

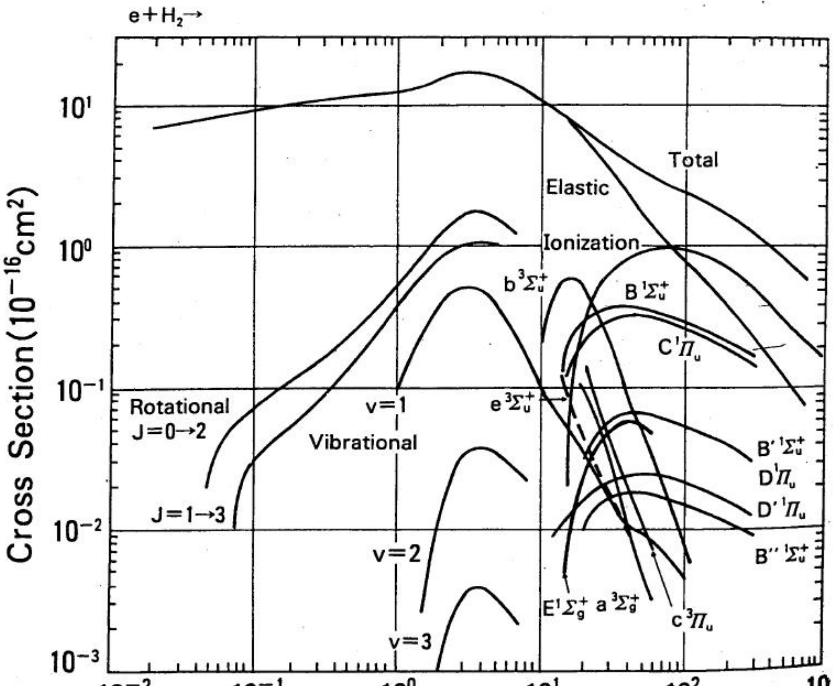

Figure 6.5: Comparison of cross sections for various collision processes in neutral H_2. Also for comparison, cross sections of ionisation of atomic hydrogen are shown. Taken from [92].

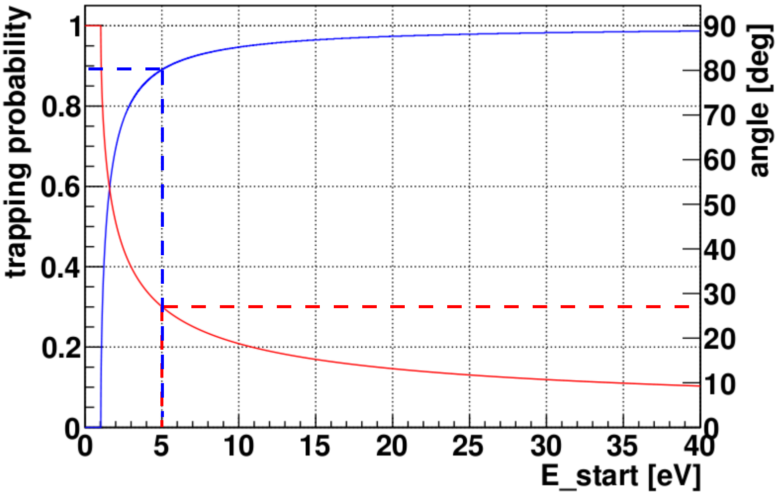

Figure 6.6: Trapping probability and maximum allowed starting angle. ***Blue***: Trapping probability. ***Red***: Maximum allowed starting angle. Electrons with a kinetic energy smaller than the energy resolution of the spectrometer can not get trapped. An electron with a kinetic energy of 5 eV is trapped with a probability of 90% because it may only start with a maximum polar angle of about 28°.

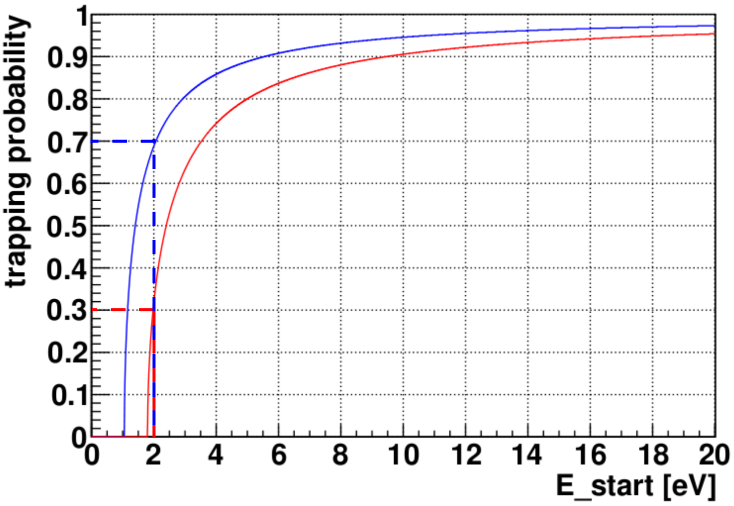

Figure 6.7: Trapping probability for different magnetic field strengths. ***Blue***: 3.5 G in the analysing plane. ***Red***: 6 G in the analysing plane. An electron with a starting kinetic energy of 2 eV has a trapping probability of 30% in the case of a magnetic field of 6 G in the analysing plane and 70% in the case of 3.5 G.

6.5 Simulations

The trapping effects of e-gun electrons in the main spectrometer have been investigated with particle tracking simulations using the *singletraj* programme package, which is discussed in chapter 3.3. To estimate the size and potential implications of electron trapping after column density scans, only electrons moving along the beam axis were considered. The electrons were started at the position of maximum magnetic field at the entrance of the main spectrometer with a polar starting angle $\theta < 10°$. These assumptions are based on the discussion in section 6.3.
Three independent simulations have been performed for the three plateau energies $E_1 = 18605$ eV, $E_2 = 18620$ eV and $E_3 = 18640$ eV of figure 6.2.
The electrons were tracked until they reached the position of maximum magnetic field on either side of the spectrometer again. They do not have to be tracked further because after having passed the point of maximum magnetic field they can not get trapped anymore due to the magnetic mirror effect. Due to the high magnetic field gradients in this region, the programme uses smaller step sizes to keep the energy error in the allowed interval of $10^{-8} - 10^{-10}$ at the cost of an increased calculation time. It was reduced by about a factor of 10 due to the implementation of this exit condition.
The adiabatic approximation was used to decrease the calculation time. Furthermore, the number of hydrogen molecules and hence the scattering probability was increased by a factor of $A = 10^5$. Tests revealed that this is an ideal number, since it is still small enough to allow for an equal distribution of scattering events inside the spectrometer volume. The implementation of such an increasing factor has two effects. On the one hand, 10^5 times more electrons scatter initially and on the other hand, the time between two consecutive scattering events of the same electron is shortened by the same factor. The simulation data, whose results will be presented below, have been corrected for these effects.

For a measurement time of 5 minutes and an e-gun rate of 10^5 Hz there will be $3 \cdot 10^7$ electrons entering the spectrometer equally distributed among the three excess energies. Within the simulation, $1 \cdot 10^6$ electrons were tracked for each excess energy. Taking into account the increasing factor $A = 10^5$, an effective number of $3 \cdot 10^{11}$ electrons was simulated.

Electrons with 5 eV excess energy

The simulation revealed a probability $P = 5 \cdot 10^{-9}$ for an initial scattering event of an electron on a hydrogen molecule. This value is slightly smaller than the estimated value of equ. (6.4). Looking at figure 6.5, the maximum cross section can be found for ≈ 5 eV. But from then on it drops fast for higher energy values. Since the electron will reach its minimal kinetic energy of 5 eV only in a region close to the analysing plane, the resulting scattering probability gets shifted towards lower values.
As explained in the introduction of this section, scattered electrons have a probability to be trapped, depending on their scattering angle and position. In this case, 66% of all scattered electrons were trapped afterwards. Figure 6.8 shows the distribution of both initial and consecutive elastic scattering events inside the main spectrometer. An equal distribution would be expected if the number density of hydrogen molecules is

identical in the whole volume. But trapped electrons, depending on their polar angle, do not reach those parts of the spectrometer, which are far away from the analysing plane. Hence, consecutive scattering processes happen closer to the analysing plane.

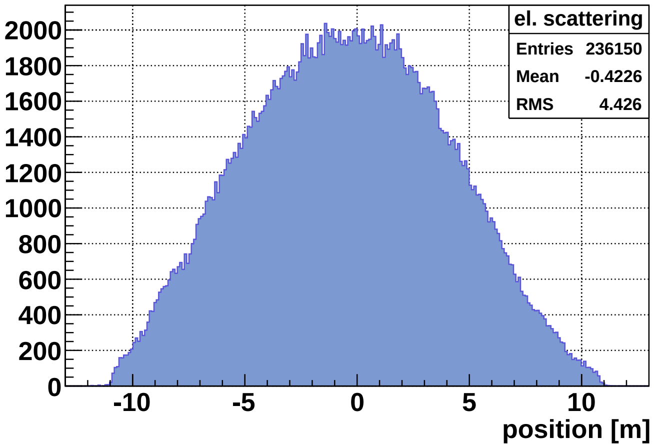

Figure 6.8: Position of elastic scattering events inside the main spectrometer.

Due to the axial homogeneity of the electric potential, the kinetic energy of these electrons stays below the excitation and ionisation energies of hydrogen for most parts of the spectrometer. Furthermore, according to figure 6.5, the scattering cross section is largest for elastic processes. Therefore, 94% of all scattering events are elastic processes. Excitation and ionisation events contribute with about 3% each. Figure 6.9 shows the position of the inelastic scattering events. The excluded region in the central part of the spectrometer, where electrons are low energetic, is readily identifiable.

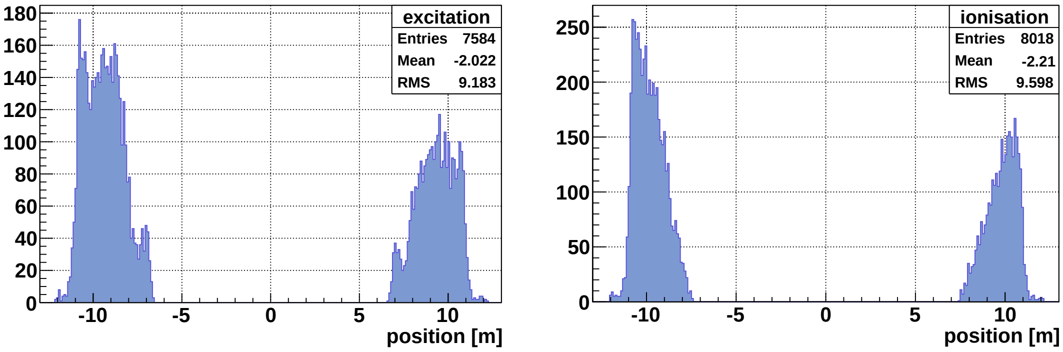

Figure 6.9: Position of inelastic scattering events inside the main spectrometer. ***Left***: Excitation events. ***Right***: Ionisation events.

There are more scattering events happening in the source-side half of the spectrometer. This is visualised by the increased peak height in figure 6.9 and the shift of the mean values of the scattering positions towards more negative values. This effect originates from the asymmetry of the magnetic field around the analysing plane, which was already

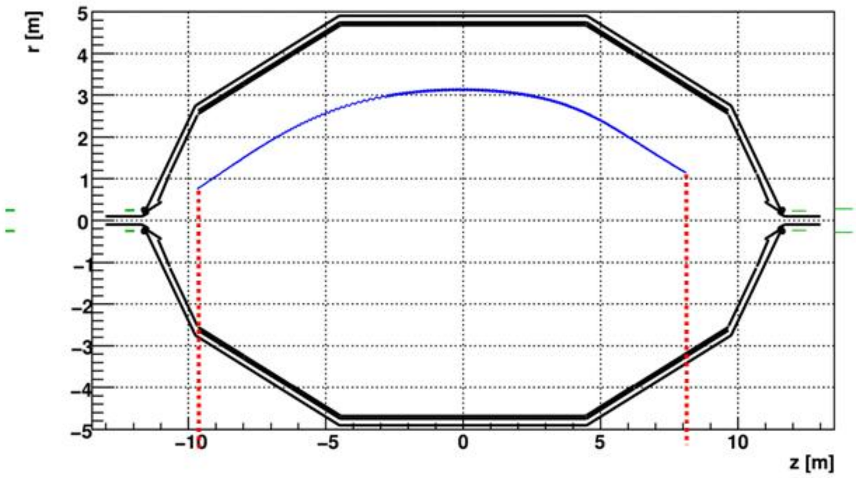

Figure 6.10: Track of a trapped electron. Due to the magnetic field asymmetry, the electron (blue) does not reach as far outside on the detector-side of the analysing plane than on the source-side. The endpoint positions are revealed by the dashed red lines.

discussed in chapter 4. Figure 6.10 shows an exemplary track of a trapped electron. In the source-side half of the spectrometer, the electron reaches the region $z < -8$ m where its kinetic energy is sufficient for an inelastic scattering process. This is not the case on the detector-side.
Trapped electrons have a 50% chance to leave the spectrometer to either side. But if they scatter inelastically in front of the analysing plane, they can not pass the electrostatic potential barrier anymore. They may only leave the spectrometer towards the source side. In total, 64% of all trapped electrons were reflected back to the source.
Figure 6.11 shows the energy loss of primary electrons after excitation of the B- and C-vibrational states and electronic states of chapter 3.3. The electrons need at least 11 eV in order to be able to create an excited state of the hydrogen molecule. Their maximum energy loss is limited by the ionisation energy $E_{ion} = 15.4$ eV of molecular hydrogen. The 28 discrete B-vibrational states are distributed between 11.2 eV and 14.25 eV. The 14 C-vribrational states can be found between 12.3 eV and 14.66 eV. There are 7 excited electronic states visible. Two of them are hidden within the vibrational states, four states can be found above 14.7 eV and one state at 13.06 eV.
The energy losses for ionisation events are shown in figure 6.12. The energy loss probability is highest for small energies but the maximum value can reach up to the total kinetic energy E_{kin} of the primary electron.

Furthermore, secondary electrons are being created. They are emitted isotropically with a kinetic energy $E_{kin} = E_{loss} - E_{ion}$. As they are produced far away from the analysing plane, they need a minimum starting angle $\theta \approx 80°$ in order to be stored. Therefore, most of them leave the spectrometer immediately after their creation.

The change of the primary electron's polar angle decides if it is trapped after a scattering event or not. Figures 6.13 and 6.14 show the angular change for elastic and inelastic scattering events. Due to the higher kinetic energy of the primary electrons

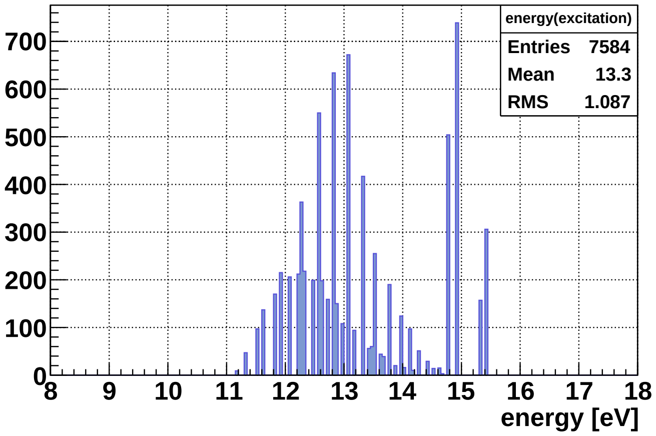

Figure 6.11: Energy loss of the primary electron due to excitation processes. The discrete energy levels of the excited states are visible.

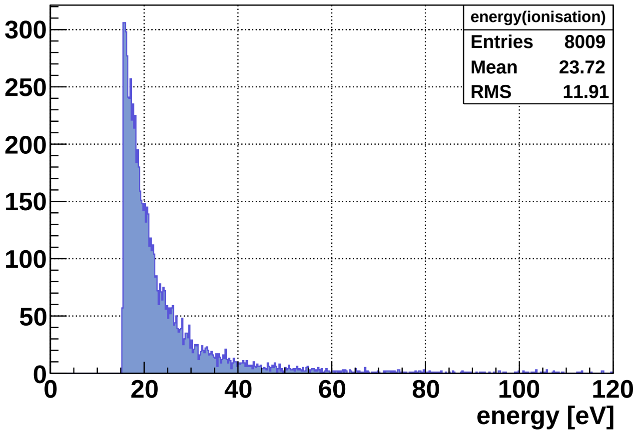

Figure 6.12: Energy loss of the primary electron due to ionisation processes. The primary electron needs a minimal kinetic energy $E_{kin} > E_{ion} = 15.4$ eV where E_{ion} is the ionisation energy of molecular hydrogen. While this plot shows a maximal energy loss of 120 eV, the tail actually reaches values up to E_{kin}.

which scatter inelastically, their angular distribution features a peak at small values. The distribution for elastically scattered electrons is a superposition of two contributions. On the one hand, there is an isotropic distribution for those electrons which scatter in the central part of the spectrometer where the electrostatic potential has its maximum and hence, the electrons have their minimum kinetic energy. On the other hand, electrons scattering in the conical parts of the spectrometer have a higher kinetic energy and the angular distribution has a peak at smaller values.

On average, it takes about 7 interactions until a trapped electron receives the suitable change of its polar angle in order to be able to leave the spectrometer. This number is mainly defined by the elastic scattering events. Firstly, they are by far the most

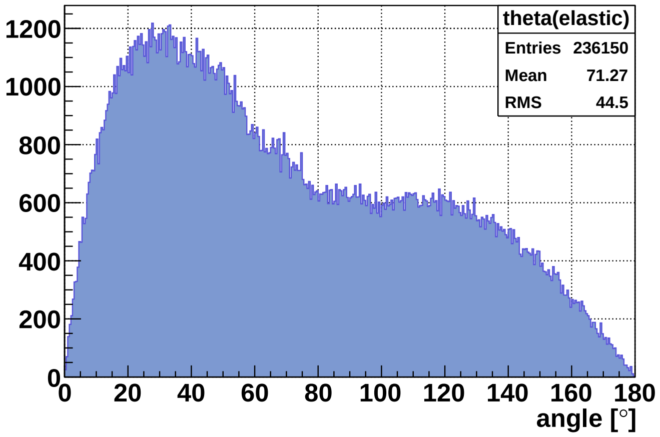

Figure 6.13: Change of the polar angle of the primary electrons due to elastic scattering events.

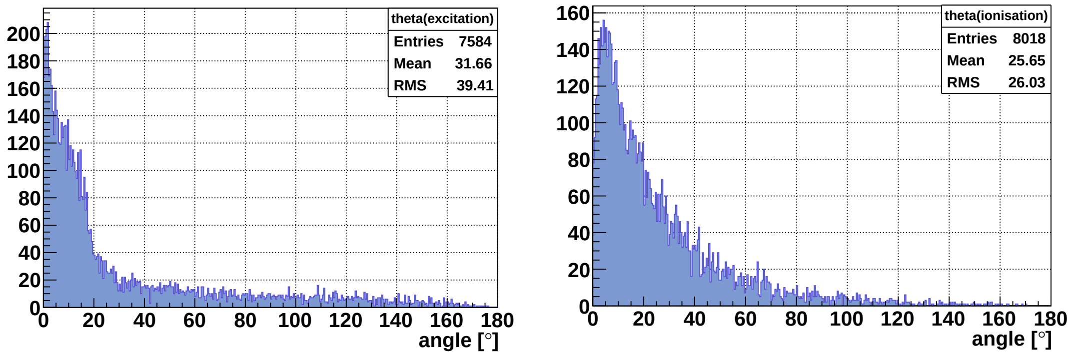

Figure 6.14: Change of the polar angle of the primary electrons due to inelastic scattering events. *Left*: Excitation events. ***Right*:** Ionisation events.

numerous events happening and secondly, their angular distribution has a wider range. Figure 6.6 shows the maximum allowed polar angle for an electron in the analysing plane in order to be transmitted. For an electron with an energy of 5 eV, the maximum allowed angle is about 28°.

The inelastic scattering events exclusively happen in regions with a magnetic field larger than 15 G. Together with the small angular change, a smaller trapping probability results. This is visualised in figure 6.7. For a small kinetic energy of 2 eV the electron has a 40% increased chance to be trapped in the case of a magnetic field strength of 3.5 G compared to a magnetic field strength of 6 G.

Electrons with 20 eV excess energy

The scattering probability P is lower for higher energetic electrons. The scattering probability is mainly defined by the cross section for elastic scattering events. Figure 6.5 shows the decreasing scattering probability for an increasing kinetic energy of the primary electron. Within this simulation, a probability $P = 2.7 \cdot 10^{-9}$ was observed, which is smaller by a factor of two than the probability for electrons with 5 eV excess energy. Furthermore, due to the higher energies, the probability for inelastic scattering events is higher. Excitation events account for 8% of all scattering events, ionisation events for a fraction of 6%.
The distribution of elastic scattering events in the case of 20 eV excess energy is comparable to the case of 5 eV. However, there are now inelastic processes happening in the central region of the spectrometer. Due to the lower energies needed for excitation, these events are distributed more equally than the ionisation events. The energy loss distributions are similar to the 5 eV case but the distribution of the polar scattering angles has changed. In case of elastic events, the distribution shows an enhanced peak at smaller angles. The energy of the primary electrons is higher than in the 5 eV case in favour of smaller scattering angles. In return, the inelastic processes show more events with higher scattering angles. The primary electrons can now scatter inelastically in a large region around the analysing plane where the electric retarding potential is high, and hence their kinetic energy is small.

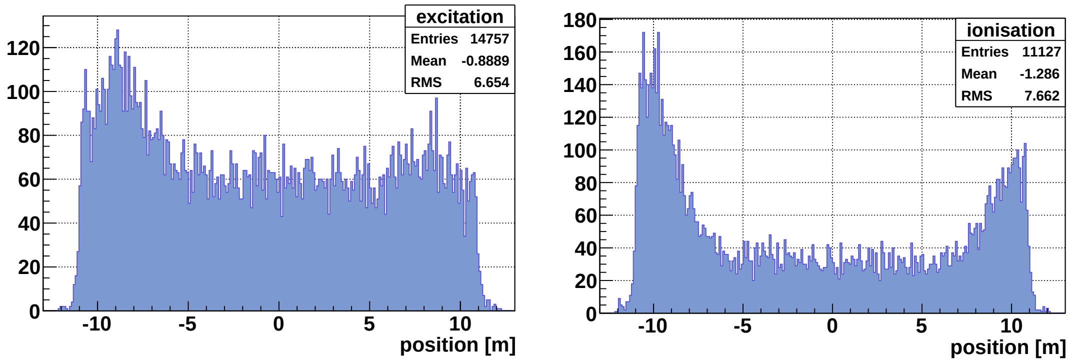

Figure 6.15: Position of inelastic scattering events inside the main spectrometer. ***Left***: Excitation events. ***Right***: Ionisation events.

The average number of scattering events until a condition is reached, where the particle can leave the spectrometer after getting trapped, is increased from 7 scatterings in the case of 5 eV to 9 scatterings in the case of 20 eV excess energy. The angular distribution of the elastic scattering events is less homogeneous than in the case of 5 eV. Furthermore, figure 6.6 shows that higher energetic electrons are limited to smaller polar angles in order to be transmitted.

The decreased scattering probability as well as the increased number of events needed until the electron can escape results in a longer trapping time for electrons starting with a higher kinetic energy.

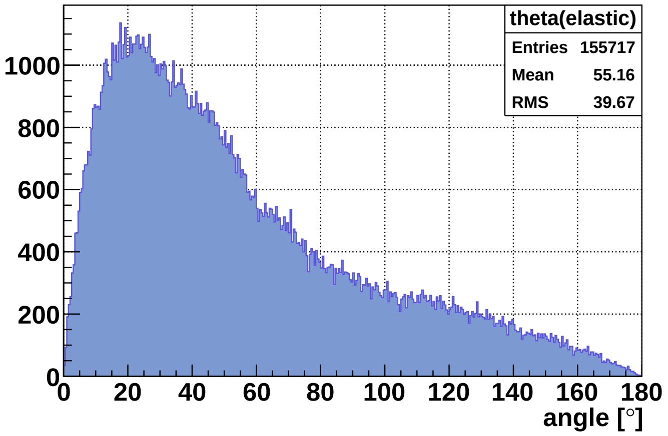

Figure 6.16: Change of the polar angle of the primary electrons due to elastic scattering events.

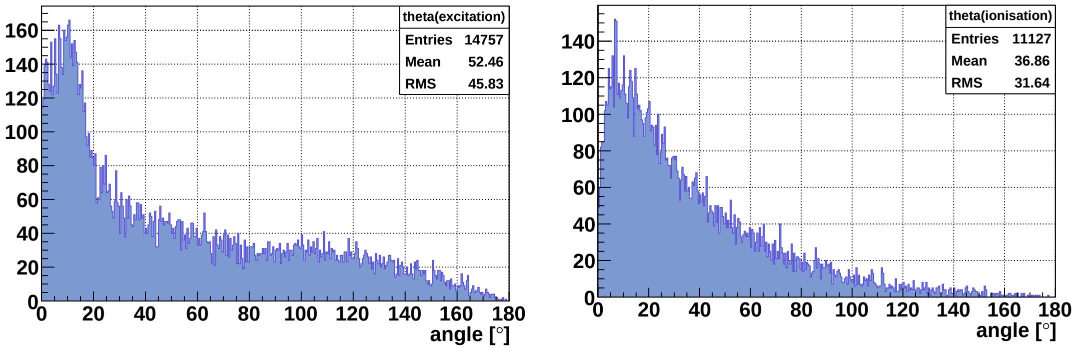

Figure 6.17: Change of the polar angle of the primary electrons due to inelastic scattering events. ***Left***: Excitation events. ***Right***: Ionisation events.

Electrons with 40 eV excess energy

All effects which were discussed for the case of 20 eV excess energy are even more enhanced in the case of 40 eV. The scattering probability now has dropped further down to $P = 2 \cdot 10^{-9}$, the proportion of excitation events is increased to 12% and to 10% for ionisation events. The positions of inelastic scattering events are now equally distributed within the whole spectrometer with a slight shift towards the source side due to the magnetic field asymmetry. The angular distributions show the same behaviour as in the case of 20 eV, i.e. a peak for small scattering angles and a long tail up to 180°. The average number of scattering events before the electron escapes the magnetic mirror increased further to 11 scatterings. Again, the maximum allowed polar angle has decreased.

Secondary electrons

Secondary electrons are being created due to ionisation processes. Their kinetic energy $E_{kin,s}$ is defined by the energy loss $E_{loss,p}$ of the primary electron:

$$E_{kin,s} = E_{loss,p} - E_{ion}, \tag{6.5}$$

where $E_{ion} = 15.4$ eV is the energy needed for the ionisation process of molecular hydrogen. Their starting positions are stored in a file together with their kinetic energy. The polar and azimuthal starting angles are generated afterwards to obtain an isotropic emission. Furthermore, each secondary electron gets a time-stamp for its creation, which is composed of the time when the primary electron was created at and the time this primary electron has already spent inside the main spectrometer until the ionisation happens. Equ. (4.9) allows to calculate the trapping probability for these secondary electrons. In the case of 5 eV excess energy, the majority of the secondary electrons has a kinetic energy of less than 5 eV. This can be derived from figure 6.12. They can only start in a region with a minimum distance of $8 - 11$ m from the analysing plane. The magnetic field there has a strength of $20 - 700$ G. These electrons cannot get trapped, independently of their starting angle. Due to the generally higher kinetic energies of electrons with 20 eV and 40 eV excess energy, the trapping probability increases. Nevertheless, within the simulation, no secondary electrons from ionisation events by 20 eV primary electrons were stored either. In the case of primary electrons with 40 eV excess energy, 31% of all secondary electrons were stored.

6.6 Results

The primary goal of this simulation was to retrieve the time distribution of trapped particles in order to be able to determine the expected background rate following a monitoring e-gun measurement. Electrons with three different excess energies $E = 5, 20, 40$ eV were started at the entrance of the main spectrometer. Due to scattering on the residual gas molecules these electrons can get trapped inside the main spectrometer. Depending on their energy it takes up to 11 further interactions until they are able to escape the magnetic mirror effect. To simulate an actual e-gun measurement of 300 seconds with an e-gun rate of 10^5 Hz, the time distribution was calculated for 100 seconds with each excess energy, starting with the highest energy of 40 eV. This order is advantageous because higher energetic electrons take longer time intervals to escape the magnetic mirror effect than lower energetic ones. Furthermore, secondary electrons are only stored for primary electrons with 40 eV excess energy. Each primary electron has a time-stamp for the time of its creation at the electron gun. Secondary electrons receive their time-stamp in dependence of the primary electrons which created them. Both primary and secondary electrons were taken into account to retrieve the background rate which is expected after the e-gun measurement finished. The following effects had to be included to obtain realistic results:

- **Backscattering**: Due to the asymmetric magnetic field, 66% of all trapped electrons and secondary electrons will be scattered back to the source.

- **Energy resolution of the detector**: The detector has an energy resolution of about 1 keV. Therefore, electrons with a total energy of $E < 17.6$ keV can be discriminated from actual signal electrons. This is only of importance for the secondary electrons, since primary electrons would have to undergo more than 40 inelastic scattering events in order to lose 1 keV of their kinetic energy. Secondary electrons, however, can start in regions with lower electric potential, decreasing their total energy by the missing potential energy.
- **Increasing factor** A: The number density of the hydrogen atoms inside the main spectrometer has artificially been increased by a factor of $A = 10^5$ in order to speed up the calculation. This had two effects:
    1. The number of initial scattering events is increased by this factor.
    2. The time-scale between consecutive scattering events of the same electron is shortened by this factor.

The following time distributions, separated for primary electrons in figure 6.18 and secondary electrons in figure 6.19, take all the above mentioned effects into account.

In the first 300 seconds, a constant rate of electrons enters the main spectrometer. Primary electrons can only get trapped within these 300 seconds. Therefore, the total number of trapped electrons increases linearly with time within these 300 seconds. At the same time, a part of these trapped electrons leaves the spectrometer again with a time-dependent rate of $r(t) \propto e^{-t/\tau_1}$, which is similar to the rate $r(t) \propto e^{-t/\tau_2}$ for times $t > 300$ s. During the e-gun measurement, the rate $r(t)$ of formerly trapped electrons, leaving towards the detector, can be calculated as the product of the linear and the exponential contribution, i.e. $r(t) \propto t \cdot e^{-t/\tau_1}$. The maximum rate is reached at the time when the e-gun measurement finishes. The rate of secondary electrons is highest within the first 200 seconds of the e-gun measurement. Most secondary electrons are being created during this time due to the higher kinetic energies of the primary electrons. Secondary electrons, which leave the spectometer after the e-gun measurement is finished, were either trapped themselves or were created by trapped primary electrons. The number of trapped secondary electrons accounts for less than 15% of their total number. Therefore, the rate of secondary electrons drops fast after the measurement is finished.

When separating the time after the e-gun measurement into smaller intervals, a mean background rate, caused by trapped electrons, can be calculated. The size of the intervals is chosen in such a way that the rate is approximately constant over time.
Table 6.1 shows the corresponding results. Both primary and secondary electrons were taken into account. The rates shown will be measured in addition to the normal spectrometer background of 1 mHz. An additional rate of 1 mHz or more is not acceptable. For lower rates, the influence on the β-spectrum has to be investigated in more detail. Nevertheless, if it is possible to just send in the electrons along the beam axis onto the central pixel, only the innermost detector region will experience an increased rate. Therefore, this region has to be taken out of the analysis for at least 10 minutes after the measurement is finished. If off-axis measurements are going to be necessary, the

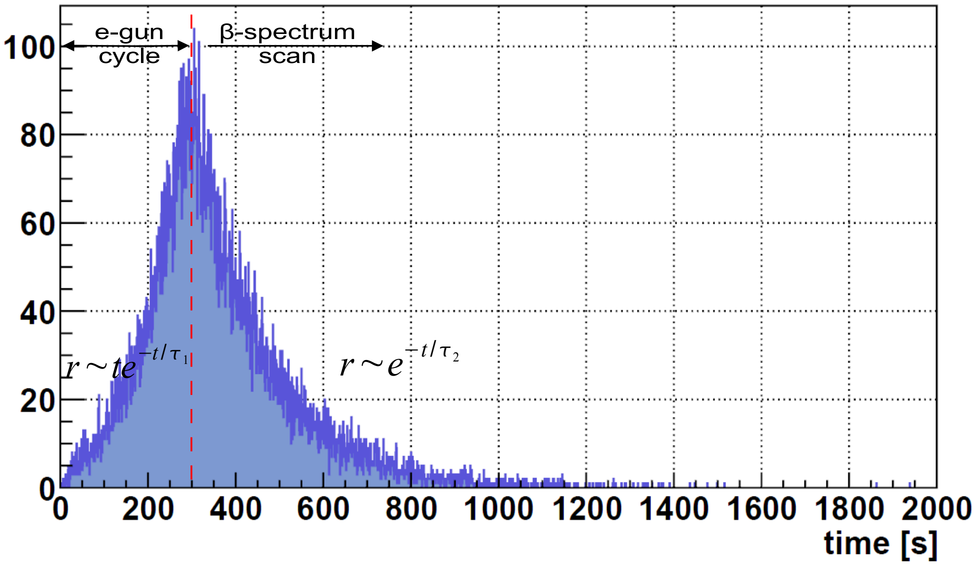

Figure 6.18: Time distribution of trapped primary electrons. Within the first 300 s a constant rate of 10^5 electrons per second enters the spectrometer. Therefore, the rate reaches its maximum at the end of this e-gun measurement. A background rate can be calculated from the exponential drop in rate after the measurement finished. Only electrons leaving towards te detector were taken into account.

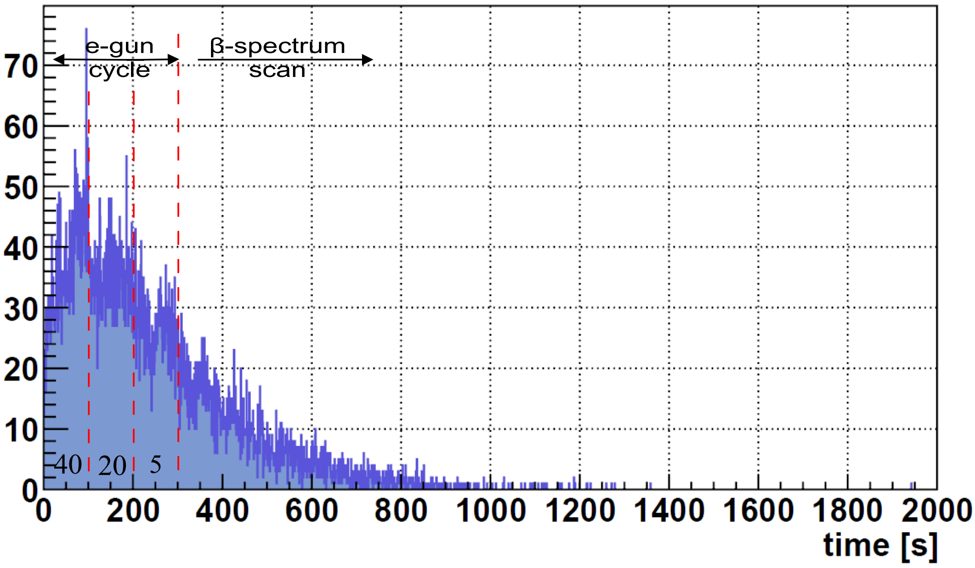

Figure 6.19: Time distribution of secondary electrons. Primary electrons with enough kinetic energy produce secondary electrons which contribute to the background rate. Only 15% of all secondary electrons are stored. Most electrons are created within the first 200 seconds because the primary electrons entering during that time interval have the highest energies.

electrons will not be limited to a single pixel of the detector but due to the azimuthal magnetron drift an increased rate will be detected throughout a whole ring. In case of an equal distribution of electrons among all 12 pixels of a ring, the rate for each pixel will be lower by a factor of 12. However, it has to be noted that any significant non-axially symmetric field contribution would lead to a radial magnetron drift of the electrons and the increased rate might get distributed over the whole detector.

time [s]	rate [mHz]	time [s]	rate [mHz]
300-310	3.7	460-480	1.0
310-320	2.4	480-500	0.9
320-330	2.3	500-525	0.9
330-340	2.1	525-550	0.8
340-350	2.1	550-575	0.7
350-360	1.9	575-600	0.6
360-370	1.8	600-660	0.35
370-380	1.7	660-720	0.2
380-390	1.6	720-780	0.2
390-400	1.5	780-840	0.1
400-420	1.4	840-900	0.07
420-440	1.2	900-2000	≈ 0
440-460	1.1		

Table 6.1: Background rate resulting from formerly trapped electrons after e-gun measurements. For an e-gun rate of 10^5 Hz and a measurement time of 300 s the background rate drops exponentially over time after the measurement finished. Test measurements should be able to identify an increased rate within the first minute after the measurement. For lower rates, as they are present at later times, the additional background can probably not get resolved from the intrinsic spectrometer background.

6.7 Test Measurements

Until the main spectrometer will be ready for test measurements, some aspects related to the above topics can be tested with the pre-spectrometer already.

Pre-spectrometer

- The trapping behaviour of electrons after an e-gun measurement with high rate can already be investigated with the pre-spectrometer. In the present configuration, no significant Penning trap related background is observed so that the additional background after a high intensity e-gun run can be distinguished and a time spectrum similar to the one obtained by this simulation can be measured. Nevertheless, the simulation has to be repeated in order to take into account the different pre-spectrometer properties. The pre-spectrometer setup is smaller and hence, the magnetic field is generally higher, resulting in an energy resolution of $\Delta E \approx 70$ eV. This means that electrons, which start in the analysing plane, need at least 70 eV transversal energy in order to be stored. Therefore, a decreased rate of trapped electrons is expected.

- It is possible to increase the pressure inside the pre-spectrometer in a controlled way by letting e.g. hydrogen stream inside. This allows to test the validity of working with an increased pressure, as used for this simulation. An increased scattering probability is expected to lead to more trapped particles, but on a shortened time scale.

Main spectrometer

- Using the same parameters as within the framework of this simulation, the time spectrum should be reproducable. Especially within the first few minutes after the e-gun measurement is finished, an increased rate should be distinguishable from the intrinsic spectrometer background.
- It can further be tested if a dipole mode of the spectrometer inner electrodes is effective for emptying the magnetic mirror trap filled with e-gun originating and secondary electrons.
- It is not yet decided on whether it will be possible to send the electrons only along the beam axis, resulting in the shortest path possible. If so, only the central pixels will have to be taken out of the analysis for at least 10 minutes after the measurement. Otherwise, electrons will be moving along a longer path and the scattering probability will be increased. Furthermore, due to the azimuthal magnetron drift, electrons will be detected within a whole ring of the spectrometer corresponding to the field line they are moving on. Also, if significant non-axially symmetric field contributions are present, an additional magnetron drift in radial direction will be observed. Electrons will then be detected on neighbour rings. On the other hand, such additional long-term magnetron drifts, if observed, would allow to study in detail the presence of non-axially symmetric field components and add to the overall understanding of the magnetic field configuration in the main spectrometer. This can be done with a deliberate magnetron motion, caused by an appropriate configuration of the inner electrodes or the EMCS, to validate the tracking and field calculation routines.
- The measurement has to be repeated for different magnetic field strengths in the analysing plane. Electrons are less likely to be trapped for higher magnetic fields in the analysing plane. This has a direct effect on the background rate due to both primary and secondary electrons.

7. Summary and Outlook

7.1 Summary

The improved sensitivity of KATRIN of 0.2 eV/c^2 with regard to predecessor experiments can only be reached if all statistical and systematical uncertainties stay below a value $\sigma^2 < 0.017$ eV^2/c^4. To keep the systematical uncertaintites at a minimum, each subsystem has to be stable on a 0.1% level. Therefore, relevant experimental parameters such as the column density ρd of the source or the magnetic field within the whole KATRIN setup have to be monitored.

Within the framework of this work the electromagnetic properties of the main spectrometer have been investigated by means of very precise electric and magnetic field calculations. These are also the basis of the advanced particle tracking routines which have been used to gain a more detailed understanding of background sources and their implications for the KATRIN experiment.

In a first step, the standard magnetic field configuration with one global magnetic field minimum in the analysing plane has been optimised concerning background and transmission properties. A possible alternative configuration with two local magnetic field minima has been presented. It is more advantageous with regard to transmission properties than the standard solution. In return, this solution could possibly lead to an increased background. Therefore, in a second step, simulations of low energetic electrons, which are starting inside the main spectrometer, have been performed to investigate this. However, no significant increase in background was found, thus making the *local magnetic field minima solution* a viable option for the KATRIN experiment.

Independently of the magnetic field configuration to be used, a monitoring system is needed to ensure the required stability of the magnetic field within the KATRIN setup. The solution, which was presented in this thesis, is based on a precise modelling of all magnetic field sources which have an influence on the magnetic field inside the main spectrometer. The expected magnetic field will be simulated and checked with magnetic field sensors attached to specific crucial positions.

During several calibration and monitoring measurements a high rate of electrons will be sent through the whole beam line. An exemplary monitoring measurement of the source column density ρd was discussed. Despite the very good vacuum of 10^{-11} mbar inside the main spectrometer, a considerable amount of electrons will scatter off the residual gas molecules. These electrons can get trapped by the magnetic mirror effect. If they are getting released during the normal β-spectrum scanning phase, they will contribute to the background and induce time-dependent background rates resulting in potential hysteresis effects during the β-spectrum scan. Additionally, they can create secondary electrons as another source of background. Such an e-gun measurement was simulated in order to obtain the time distribution of trapped and secondary electrons.

An important goal of this thesis was to prepare the optimised LFCS input parameters for the upcoming test measurements and the final setup. In parallel, the LFCS and EMCS hardware components were built up according to the design calculations. The utility of Monte Carlo simulations to investigate the properties of the electromagnetic design of the main spectrometer was tested successfully. As all simulations are based on 'ideal' input parameters, the calculations and particle tracking algorithms have to be validated within an extensive test measurement phase.

7.2 Outlook

Up to the present, the magnetic field calculations are available for axially symmetric fields only. Non-axially symmetric fields, however, are a potential source of background due to the radial magnetron drift of electrons into the flux tube. Therefore, this process has to be implemented into the existing routines.

Particle tracking was limited to the spectrometer section within this thesis. It would be of great importance to have a *global tracking programme package* in order to simulate electron motion through the KATRIN experiment as a whole. So far, routines exist for the single components of the experimental setup and they will be brought together in the near future.

The magnetic field monitoring system will be implemented in parallel. Within this thesis, the theory underlying this system was presented and the different required measurements were discussed. For the final use of such a system during the actual tritium measurements, an online monitoring has to be set up to compare measured and calculated magnetic field values. Any deviations from the calculated values have to be recorded to minimise the systematic effects.

Complementary to the simulations that have been and will be performed, a period of test measurements is essential. On the one hand, they are needed to validate the simulations. On the other hand, further insight on background effects can be gained. Finally, these measurements, which will start in mid-2010, can provide new ideas for experimental aspects to be simulated.

Only by continuously improving both the hardware performance aswell as the accuracy of the simulation tools, the KATRIN experiment, and the main spectrometer as a central component in particular, will allow to measure the neutrino mass with an unprecedented sensitivity for astroparticle physics.

A. Technical Drawings

This appendix contains technical drawings of the LFCS and EMCS components as a reference.

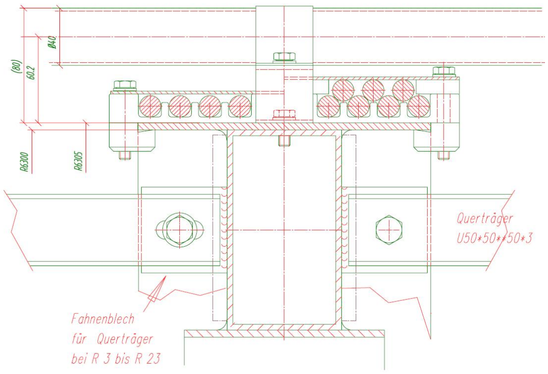

Figure A.1: Cross section of an LFCS ring with 8 windings (lower layer) and the possibility to add 6 more windings (upper layer).

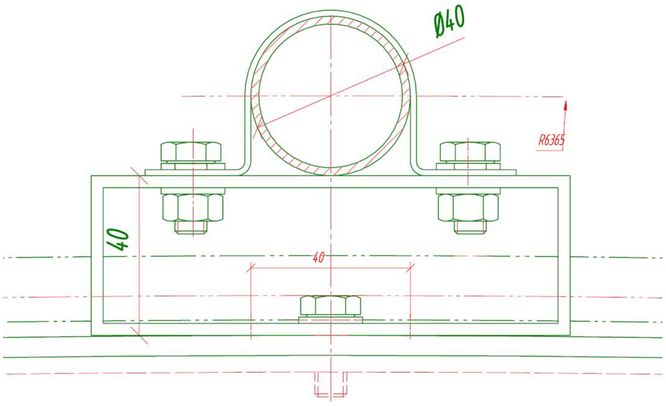

Figure A.2: Cross section of a cable duct for an EMCS cable which will be connected to an LFCS ring.

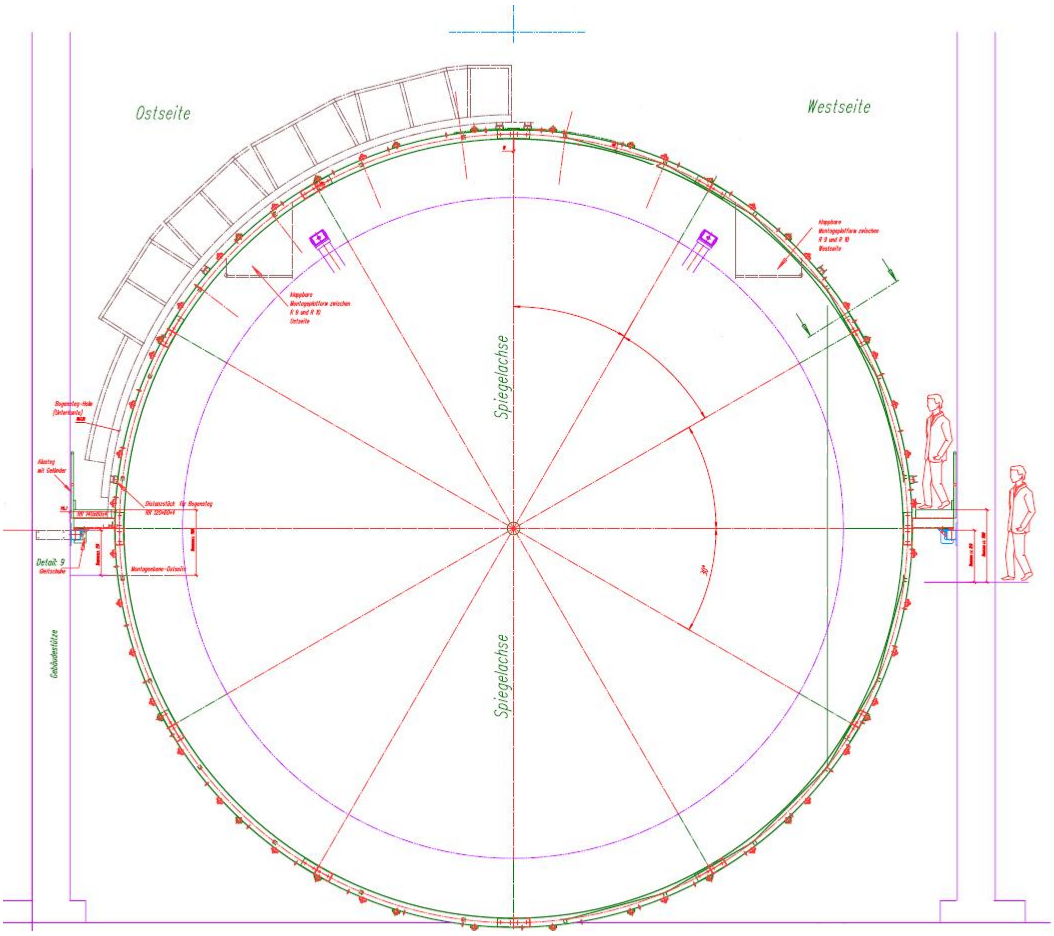

Figure A.3: Cross section of the main spectrometer (violet) surrounded by an LFCS ring (green). The red/green circles at the outside of the ring indicate the vertical/horizontal EMCS. The upper left quarter shows the ladder (brown) for personnel access to the coils and high voltage ports.

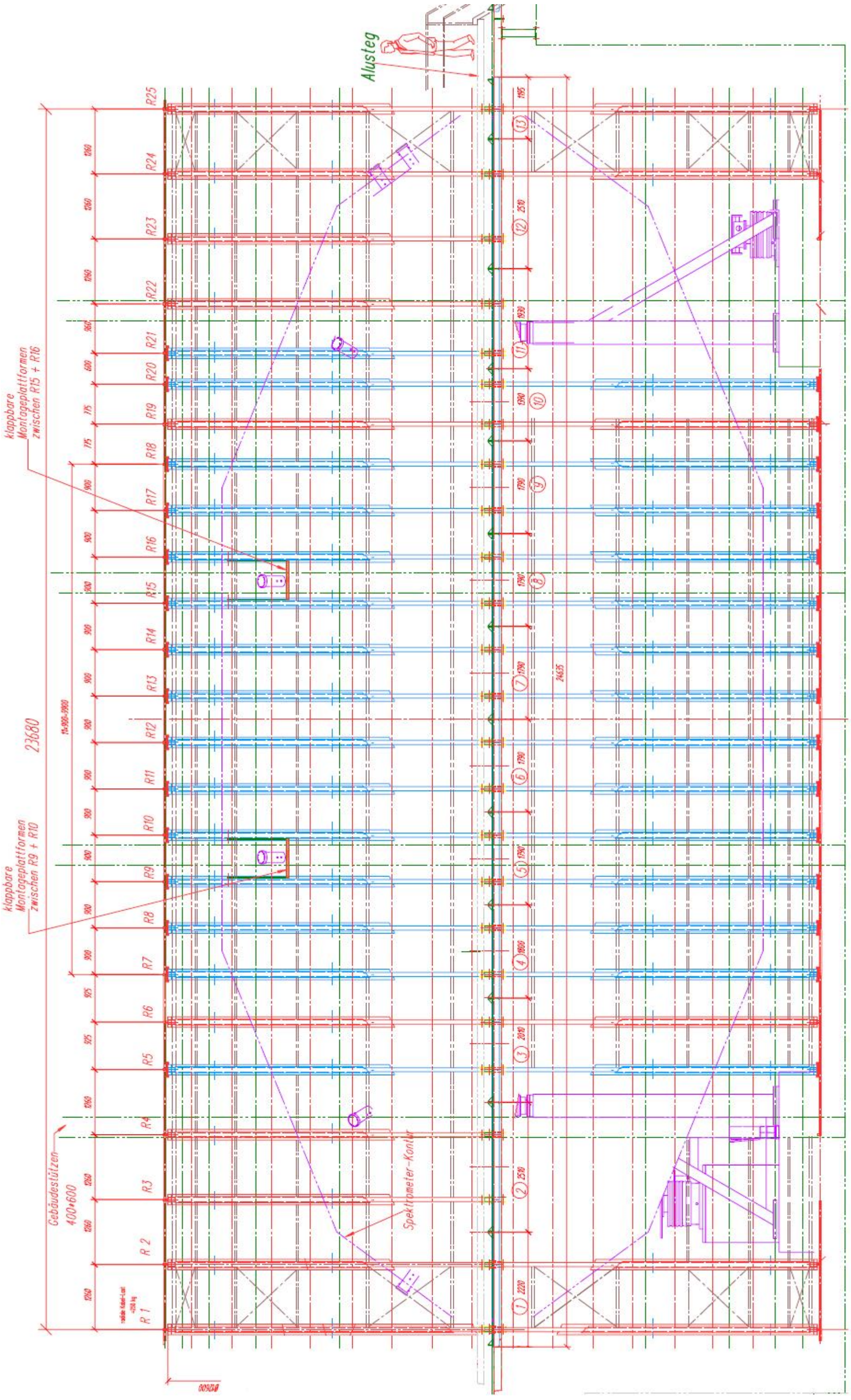

Figure A.4: Side view of the main spectrometer and LFCS. The blue rings are actual LFCS rings, the red rings exist for stability reasons and the outermost rings are used by the EMCS.

B. Magnetic Field Configurations

This appendix gives an overview of the precise ampere turns settings of the LFCS for different magnetic field configurations for both the final and a possible test measurement setup.

Magnetic Field Configurations for the Final Setup

Type	Position [m]	Ampere turns [At] (one minimum)	ampere turns [At] (two minima)
coil 1	-6.80	130	0
coil 2	-4.95	130	50
coil 3	-4.05	100	50
coil 4	-3.15	110	50
coil 5	-2.25	140	100
coil 6	-1.35	140	220
coil 7	-0.45	135	280
coil 8	0.45	135	280
coil 9	1.35	140	260
coil 10	2.25	140	150
coil 11	3.15	140	120
coil 12	4.05	160	100
coil 13	4.95	160	140
coil 14	6.60	-525	-800
coil 15	6.90	-525	-800

Table B.1: Input parameters for the coils of the LFCS. Together with the constant magnetic field sources (input parameters are shown in table 4.1) the magnetic field strength in the centre of the analysing plane is about 3.5 G and at the edge of the flux tube 3 G.

Type	Position [m]	Ampere turns [At] (one minimum)	ampere turns [At] (two minima)
coil 1	-6.80	140	0
coil 2	-4.95	220	50
coil 3	-4.05	220	50
coil 4	-3.15	220	100
coil 5	-2.25	230	240
coil 6	-1.35	230	300
coil 7	-0.45	230	400
coil 8	0.45	230	400
coil 9	1.35	230	350
coil 10	2.25	210	170
coil 11	3.15	210	160
coil 12	4.05	210	120
coil 13	4.95	160	140
coil 14	6.60	-200	-700
coil 15	6.90	-200	-700

Table B.2: Input parameters for a magnetic field strength of 4 G.

Type	Position [m]	Ampere turns [At] (one minimum)	ampere turns [At] (two minima)
coil 1	-6.80	300	-140
coil 2	-4.95	400	210
coil 3	-4.05	400	430
coil 4	-3.15	400	430
coil 5	-2.25	370	450
coil 6	-1.35	380	510
coil 7	-0.45	380	500
coil 8	0.45	360	470
coil 9	1.35	370	460
coil 10	2.25	390	410
coil 11	3.15	370	380
coil 12	4.05	320	360
coil 13	4.95	180	110
coil 14	6.60	0	-365
coil 15	6.90	0	-365

Table B.3: Input parameters for a magnetic field strength of 6 G.

Magnetic Field Configurations for Test Measurements

Type	Position [m]	Ampere turns [At] (one minimum)	ampere turns [At] (two minima)
coil 1	-6.80	500	200
coil 2	-4.95	500	200
coil 3	-4.05	150	200
coil 4	-3.15	150	200
coil 5	-2.25	150	200
coil 6	-1.35	150	200
coil 7	-0.45	150	200
coil 8	0.45	150	200
coil 9	1.35	150	200
coil 10	2.25	150	200
coil 11	3.15	150	200
coil 12	4.05	150	200
coil 13	4.95	500	200
coil 14	6.60	250	100
coil 15	6.90	250	100

Table B.4: Input parameters for the coils of the LFCS. Together with the pre-spectrometer superconducting coils (input parameters are shown in table 4.2) the magnetic field in the centre of the analysing plane is about 3 G.

Type	Position [m]	Ampere turns [At] (one minimum)	ampere turns [At] (two minima)
coil 1	-6.80	900	245
coil 2	-4.95	200	245
coil 3	-4.05	200	245
coil 4	-3.15	200	245
coil 5	-2.25	200	245
coil 6	-1.35	200	245
coil 7	-0.45	200	245
coil 8	0.45	200	245
coil 9	1.35	200	245
coil 10	2.25	200	245
coil 11	3.15	200	245
coil 12	4.05	200	245
coil 13	4.95	200	245
coil 14	6.60	440	120
coil 15	6.90	440	120

Table B.5: Input parameters for a magnetic field strength of 3.5 G.

Type	Position [m]	Ampere turns [At] (one minimum)	ampere turns [At] (two minima)
coil 1	-6.80	600	300
coil 2	-4.95	600	300
coil 3	-4.05	250	300
coil 4	-3.15	250	300
coil 5	-2.25	250	300
coil 6	-1.35	250	300
coil 7	-0.45	250	300
coil 8	0.45	250	300
coil 9	1.35	250	300
coil 10	2.25	250	300
coil 11	3.15	250	300
coil 12	4.05	250	300
coil 13	4.95	600	300
coil 14	6.60	300	150
coil 15	6.90	300	150

Table B.6: Input parameters for a magnetic field strength of 4 G.

Type	Position [m]	Ampere turns [At] (one minimum)	ampere turns [At] (two minima)
coil 1	-6.80	1500	400
coil 2	-4.95	1000	400
coil 3	-4.05	250	400
coil 4	-3.15	250	400
coil 5	-2.25	250	400
coil 6	-1.35	250	400
coil 7	-0.45	250	400
coil 8	0.45	250	400
coil 9	1.35	250	400
coil 10	2.25	250	400
coil 11	3.15	250	400
coil 12	4.05	250	400
coil 13	4.95	1000	400
coil 14	6.60	750	200
coil 15	6.90	750	200

Table B.7: Input parameters for a magnetic field strength of 5 G.

Type	Position [m]	Ampere turns [At] (one minimum)	ampere turns [At] (two minima)
coil 1	-6.80	1500	560
coil 2	-4.95	1200	560
coil 3	-4.05	350	560
coil 4	-3.15	350	560
coil 5	-2.25	350	560
coil 6	-1.35	350	560
coil 7	-0.45	350	480
coil 8	0.45	350	480
coil 9	1.35	350	560
coil 10	2.25	350	560
coil 11	3.15	350	560
coil 12	4.05	350	560
coil 13	4.95	1200	560
coil 14	6.60	800	280
coil 15	6.90	800	280

Table B.8: Input parameters for a magnetic field strength of 6 G.

Bibliography

[1] N. Schmitz. *Neutrinophysik.* Teubner Studienbücher Physik, Stuttgart, 1997.

[2] Particle Data Group. *Particle Physics Booklet.* Extracted from C. Amsler et al., Phys. Lett. B **667** (2008) 1.

[3] KATRIN Collaboration. *KATRIN Design Report 2004.* Wissenschaftliche Berichte FZKA 7090.

[4] N. Bohr. *Faraday lecture. Chemistry and the quantum theory of atomic constitution.* J. Chem. Soc. (1932), 349-384.

[5] W. Pauli. *Offener Brief an die Gruppe der Radioaktiven bei der Gauvereins-Tagung in Tübingen.* Eds. Kronig & Weisskopf, Collected Scientific Papers (1964), 1316-1317.

[6] J. Chadwick. *Possible Existence of a Neutron.* Nature (1932), 312.

[7] E. Fermi. *Versuch einer Theorie der β-Strahlen.* Zeitschrift für Physik A **88** (1934), 161-177.

[8] F. Reines; C.L. Cowan. *Detection of the Free Neutrino.* Phys. Rev. **92** (1953), Nov., Nr. 3, 830-831.

[9] G. Danby et al. *Observation of high-energy neutrino reactions and the existence of two kinds of neutrinos.* In K. Winter, Neutrino physics (1991) 57.

[10] K. Kodama et al. *Observation of tau-neutrino interactions.* Phys. Lett., B504:218-224, 2001.

[11] S. Eidelmann et al. *Rev. part. phys.* Phys. Lett. B, 592:1+, 2004.

[12] B. Povh et al. *Teilchen und Kerne.* Springer Verlag, 1999, ISBN 978-3-540-68075-8.

[13] A.W. Sunyar M. Goldhaber, L. Grodzins. *Helicity of neutrinos.* Phys. Rev., 109(3):1015-1017, Feb 1968.

[14] Y. Fukuda et al. *Evidence for oscillation of atmospheric neutrinos.* Phys. Rev. Lett. 81(8):1562-1567, Aug 1998.

[15] J.N. Bahcall. *Solving the Mystery of the Missing Neutrinos.* `http://nobelprize.org/nobel_prizes/physics/articles/bahcall/`.

[16] R. Davis. *A review of measurements of the solar neutrino flux and their variation.* Nucl. Phys. B (Proc. Suppl.) **48** (1996) 284.

[17] Q.R. Ahmad et al. *Measurement of the rate of* $\nu_e + d \rightarrow p + p + e^-$ *interactions produced by* ^{8}Be *Solar Neutrinos at the Sudbury Neutrino Observatory.* Phys. Rev. Lett. **87** (2001) 071301.

[18] W. Hampel et al. *GALLEX solar neutrino observations: results for GALLEX IV.* Physics Letters B **447** (1999) 127-133.

[19] M. Altmann et al. *Complete results for five years of GNO solar neutrino observations.* Physics Letters B **616** (2005) 174-190.

[20] Q.R. Ahmad et al. *Measurement of charged current interactions produced by* ^{8}B *solar neutrinos at the Sudbury Neutrino Observatory.* `http://www.sno.phy.queensu.ca/sno/first_results/`.

[21] S.P. Mikheyev and A.Yu. Smirnov. *Resonant amplification of* ν *oscillations in matter and solar-neutrino spectroscopy.* Il Nuovo Cimento C **9/1** (1986) 17-26.

[22] L. Wolfenstein. *Neutrino oscillations in matter.* Phys. Rev. D **17/9** (1978) 2369-2374.

[23] S.R. Elliot et al. *Direct evidence for two-neutrino double-beta decay in* ^{82}Se. Phys. Rev. Lett. **59** (1987) 2020.

[24] T.D. Lee and C.N. Yang. *Question of Parity Conservation in Weak Interactions.* Phys. Rev. **104** (1956) 254-258.

[25] C.S. Wu et al. *Experimental Test of Parity Conservation in Beta Decay.* Phys. Rev. **105** (1957) 1413-1415.

[26] A. Faessler. *Grand unified theories and the double beta-decay.* Lecture Notes in Physics Vol. **279** (1987) 291-307, Springer Berlin/Heidelberg.

[27] H.V. Klapdor-Kleingrothaus et al. *Evidence for neutrinoless double beta decay.* Mod. Phys. Lett. A **16** (2002) 2409.

[28] Craig E. Aalseth et al. *Comment on "Evidence for Neutrinoless Double Beta Decay".* Mod. Phys. Lett. A **17**, 1475-1478, Jan 2002.

[29] S. Schönert et al. *The GERmanium Detector Array (GERDA) for the search of neutrinoless* $\beta\beta$ *decays of* ^{76}*Ge at LNGS.* Nucl. Phys. B (Proc. Suppl.) **145** (2005) 242.

[30] M. Pedretti et al. *Cuore Experiment: The search for neutrinoless double beta decay.* Int. J. Mod. Phys. A **23** (2008) 3395.

[31] D. Akimov et al. *EXO: an advanced Enriched Xenon double-beta decay Observatory.* Nucl. Phys. B (Proc. Suppl.) **138** (2005) 224.

[32] J.C. Mather et al. *A preliminary measurement of the Cosmic Microwave Background spectrum by the Cosmic Background Explorer (COBE) satellite.* Astrophys. J. Lett. **354** (1990) L37.

[33] E. Komatsu et al. *Five-Year Wilkinson Microwave Anisotropy Probe (WMAP) Observations: Cosmological Interpretation.* Astrophys. J. Suppl. **180** (2009) 330.

[34] M. Colless et al. *The 2dF Galaxy Redshift Survey: spectra and redshifts.* Mon. Not. R. Astron. Soc. **328** (2001) 1039.

[35] D.G. York et al. *The Sloan Digital Sky Survey: Technical Summary.* Astronomical J. **120** (2000) 1579.

[36] Ch. Kraus et al. *Final Results from phase II of the Mainz Neutrino Mass Search in Tritium β Decay.* `http://arxiv.org/abs/hep-ex/0412056`.

[37] V.M. Lobashov et al. *Direct search for mass of neutrino and anomaly in the tritium β-spectrum.* Physics Letters B **460** (1999) 227-235.

[38] M. Sisti et al. *New limits from the Milano neutrino mass experiment with thermal microcalorimeters.* Nucl. Instr. and Meth. in Phys. A **520** (2004) 125.

[39] F. Gatti et al. *MARE Microcalorimeter Arrays for a Rhenium Experiment.* `http://mare.dfm.uninsubria.it`, 2006.

[40] J. Beamson et al. *The collimating and magnifying properties of a superconducting field photoelectron spectrometer.* J. Phys. E **13** (1980) 64.

[41] A. Poon et al. *Rear Section Design Document - Outline of Questions.* KATRIN internal document, `http://fuzzy.fzk.de/bscw/bscw.cgi/d479671/RearSectionDesignQuestions_v1.pdf`, 2008.

[42] M. Steidl. *Review of Detector Design Summer 07.* `http://fuzzy.fzk.de/bscw/bscw.cgi/d417895/Focal%20plane%20detector%20design%20document.pdf`.

[43] F. Glück et al. *Design Document Air Coil System & Magnetic Field Sensor System.* `http://fuzzy.fzk.de/bscw/bscw.cgi/d530439/Air%20Coil%20System%20and%20Magnetic%20Field%20Sensor%20System.pdf`.

[44] World Data Center for Geomagnetism. *International Geomagnetic Reference Field (IGRF).* Kyoto University, `http://swdcwww.kugi.kyoto-u.ac.jp/index.html`.

[45] A. Osipowicz. *Compensation and Manipulation of the Magnetic Field at the Main Spectrometer.* `http://fuzzy.fzk.de/bscw/bscw.cgi/90040`.

[46] J. Reich. *Magnetfeldmessungen und Designarbeiten für das EMCS Luftspulensystem am KATRIN Hauptspektrometer.* Diploma thesis, University of Karlsruhe, Sept. 2009.

[47] F. Glück. *Earth-field compensation with cylindrical or ellipsoidal coil.* `http://fuzzy.fzk.de/bscw/bscw.cgi/d99726/FG_compcoil.pdf`.

[48] J.W. Clark. *A New Method for Obtaining Uniform Magnetic Fields.* Rev. Sci. Instrum. **9** (1938) 320.

[49] J.E. Osemeikhian J.E. Everett. *Spherical coils for uniform magnetic fields.* J. Sci. Instrum. **43** (1966) 470.

[50] F. Glück. *The axisymmetric aircoil system and the magnetic field in the main spectrometer.* `http://fuzzy.fzk.de/bscw/bscw.cgi/d208402/95-TRP-4040-A2-FGlueck.ppt`.

[51] F. Glück. *EMD calculations for the new coil system near the main spectrometer.* `http://fuzzy.fzk.de/bscw/bscw.cgi/d273480/95-TRP-4153-C1-FGlueck.ppt`.

[52] B. Kuffner. *Konstruktionskonzept der Luftspulen für das Hauptspektrometer im KATRIN Experiment.* Projektarbeit 4. Semester, FZK-IK, Aug. 2005.

[53] M. Richter. *Konstruktionskonzept der Luftspulen für das Hauptspektrometer im KATRIN Experiment.* 1. Praxissemester, FZK-IK, Feb. 2006.

[54] F. Fränkle. *PhD thesis in preparation.* KIT, 2009.

[55] M.W. Garrett. *An elliptic integral computer package for magnetic field, forces, and mutual inductances of axisymmetric systems and a versatile line-tracing routine.* Oak Ridge National Laboratory, Tennessee, April 1965.

[56] J. Lekner. *Axially symmetric charge distributions and the arithmetic geometric mean.* Journal of Electrostatics, Aug. 2009.

[57] W.J. Cody. *Chebyshev approximation for the complete elliptic integrals K and E.* Math. Comp. **19** (1965) 105-112.

[58] W.H. Press et al. *Numerical Recipes.* Cambridge University Press (1986-92) 260.

[59] F. Glück. *Magnetic field calculation of coils by elliptic integrals.* To be published.

[60] F. Glück. *Axisymmetric magnetic field calculation with zonal harmonic expansion.* To be published.

[61] F. Glück. *The axisymmetric magnetic field calculation program package magfield2.* `http://fuzzy.fzk.de/bscw/bscw.cgi/d217050/magfield2.pdf`.

[62] F. Glück. *The 3-dimensional magnetic field calculation program package magfield3.* `http://fuzzy.fzk.de/bscw/bscw.cgi/d217038/magfield3.pdf`.

[63] K. Valerius. *Elektromagnetisches Design für das Hauptspektrometer des KATRIN Experiments.* Diploma thesis at University of Bonn, Dec. 2004.

[64] F. Glück. *The 3-dimensional electric field calculation program package elcd3_2.* `http://fuzzy.fzk.de/bscw/bscw.cgi/d217058/elcd3_2.pdf`.

[65] W.J. Cody. *Chebyshev approximations for the complete elliptic integrals K and E.* Math. of Comp. **19** (1965) 105.

[66] F. Glück. *Axisymmetric electric field calculation by zonal harmonic expansion.* To be published.

[67] F. Glück. *Axisymmetric electric field calculation by BEM and elliptic integrals.* To be published.

[68] F. Glück. *Electric field calculation for electrodes with discrete rotational symmetry.* To be published.

[69] F. Glück. *Runge-Kutta method for numerical solution of differential equation system.* `http://fuzzy.fzk.de/bscw/bscw.cgi/d479152/rungekutta.pdf`.

[70] K. Essig. *Untersuchungen zur Penningfalle zwischen den Spektrometern des KATRIN Experiments.* Diploma thesis at University of Bonn, Jan. 2004.

[71] J.W. Liu. *Total cross sections for high-energy electron scattering by* $H_2(^1\sum_g^+)$, $N_2(^1\sum_g^+)$ *and* $O_2(^3\sum_g^-)$. Phys. Rev. **A35** (1987) 591-597.

[72] S. Trajmar. *Electron-scattering by molecules - experimental methods and data.* Phys. Rep. **97** (1983) 221.

[73] G.P. Arrighini and F. Biondi. *A study of the inelastic scattering of fast electrons from molecular hydrogen.* Mol. Phys. **41** (1980) 1501.

[74] Zhifan Chen and A.Z. Msezane. *Calculation of the excitation cross section for the* $^1\sum_u^+$ *and* $C^1\Pi_u^+$ *states in* e-H_2 *scattering at* 60 eV. Phys. Rev. **A51** (1995) 3745-3750.

[75] W. Hwang, Y.-K. Kim, and M.E. Rudd. *New model for electron-impact ionization cross sections of molecules.* J. Chem. Phys. **104** (1996) 2956.

[76] J.W. Liu. *Total inelastic cross section for collisions of* H_2 *with fast charged particles.* Phys. Rev. **A7** (1973) 103-109.

[77] F. James. *A review of pseudorandom number generators.* Comput. Phys. Comm. **60** (1990) 339.

[78] F. Glück A. Osipowicz. *Air coil design at the main spectrometer.* `http://fuzzy.fzk.de/bscw/bscw.cgi/d443733/95-TRP-4440-D1-FGlueck-AOsipovicz.ppt`.

[79] F. Glück. *Background theory: radial motion of electrons from spectrometer electrodes into the fluxtube.* `http://fuzzy.fzk.de/bscw/bscw.cgi/d174403/background_theory_Glueck.pdf`.

[80] S. Mertens. *PhD thesis in preparation.* KIT, 2009.

[81] A.H. Snell and F. Pleasonton. *The atomic and molecular consequences of radioactive decay.* J. Phys. Chem. **62** 11 (1958) 1377-1382.

[82] P. Renschler. PhD thesis in preparation, KIT, 2009.

[83] A. Reiner. *Entwicklung eines 3D Messtisches für eine Magnetfeldmessung im Raum.* Diploma thesis at University of Applied Sciences Karlsruhe, May 2009.

[84] B. Leiber. Diploma thesis in preparation, University of Karlsruhe, 2009.

[85] M. Hötzel. *Berechnung von KATRIN Messspektren unter Einbeziehung der Eigenschaften der fensterlosen gasförmigen Tritiumquelle.* Diploma thesis at University of Karlsruhe, June 2009.

[86] I. Wolff. *Entfaltung der Energieverlustfunktion beim KATRIN Experiment.* Diploma thesis at University of Münster, July 2008.

[87] J. Geiger. *Streuung von 25 keV-Elektronen an Gasen.* Z. Physik **181** (1964) 413.

[88] M. Schlösser. *First Laser Raman measurements with tritium for KATRIN and studies of systematic effects of the LARA-setup.* Diploma thesis at KIT, Oct. 2009.

[89] M. Beck et al. *An angular defined photoelectron source for the KATRIN experiment.* Talk given at the XVII. KATRIN Collaboration Meeting, Oct. 2009, `http://fuzzy.fzk.de/bscw/bscw.cgi/d579241/95-TRP-4762-S6-MBeck.pdf`.

[90] R.C. Ulsh et al. *Bethe surface, elastic and inelastic differential cross sections, Compton profile, and binding effects for* H_2 *obtained by electron scattering with 25 keV incident electrons.* J. Chem. Phys. **60**, No. 1 (1974) 103-111.

[91] W. Käfer. *Private communication.* KIT, 2009.

[92] H. Tawara et al. *Cross sections and related data for electron collisions with hydrogen molecules and molecular ions.* J. Phys. Chem. Ref. Data **19** (1990) 617.

Danksagung

An dieser Stelle möchte ich allen danken, die zum Gelingen dieser Arbeit beigetragen haben. Ganz besonderer Dank gebührt hierbei folgenden Personen:

- Prof. Dr. Guido Drexlin für die anspruchsvolle Aufgabenstellung und die gute Betreuung während der gesamten Zeit,
- Prof. Dr. Wim de Boer für das Wecken meines Interesses am Thema Kosmologie durch seine Vorlesung und dafür, dass er sich freundlicherweise als Korreferent für diese Arbeit zur Verfügung gestellt hat,
- Dr. Ferenc Glück für die Bereitstellung seiner zahlreichen Programme, ohne welche diese Arbeit gar nicht möglich gewesen wäre. Ganz besonders möchte ich mich auch für die vielen erkenntnisreichen Diskussionen und das Korrekturlesen meiner Arbeit bedanken.
- Dipl.-Phys. Susanne Mertens für ihre gute Betreuung, die Geduld bei der Beantwortung all meiner Fragen und das Korrekturlesen meiner Arbeit,
- Dr. Udo Schmitt und Dipl.-Phys. Wolfgang Käfer für das emsige Korrekturlesen meiner Arbeit,
- Dipl.-Phys. Florian Fränkle, Dipl.-Phys. Pascal Renschler und Dipl.-Phys. Wolfgang Käfer für die Beantwortung all meiner C, C++ und ROOT Fragen,
- allen Mitarbeitern der Institute für Kernphysik und Technische Physik im Forschungszentrum Karlsruhe für die sehr angenehme Arbeitsatmosphäre und die stets vorhandene Hilfsbereitschaft, sowie jedem, der nicht namentlich erwähnt ist.

Ganz besonderer Dank gilt dem für mich wichtigsten Menschen, meinem Schatz Nico, der mich während meines gesamten Studiums unterstützt hat und seiner Familie, ohne die mir ein Studium gar nicht möglich gewesen wäre.